

TEL AVIV UNIVERSITY

The Iby and Aladar Fleischman Faculty of Engineering

The Zandman-Slaner School of Graduate Studies

**RESUSPENSION OF PARTICLES UNDER AN
OSCILLATING GRID**

A thesis submitted toward a degree of

Master of Science in Mechanical Engineering

by

Hadar Traugott

January 2015

TEL AVIV UNIVERSITY

The Iby and Aladar Fleischman Faculty of Engineering

The Zandman-Slaner School of Graduate Studies

RESUSPENSION OF PARTICLES UNDER AN OSCILLATING GRID

A thesis submitted toward a degree of
Master of Science in Mechanical Engineering

by

Hadar Traugott

This research was carried out in The
School of Mechanical Engineering

This work was carried out under the supervision of

Prof. Alex Liberzon

January 2015

Acknowledgments

First and foremost, I would like to thank my supervisor professor Alex Liberzon, for his devoted and patient guidance. For sharing his vast knowledge and experience, valuable comments and encouragement from the start until the end of my study. I appreciate all his contributions of time, ideas and funding to make my experience productive and stimulating. The joy and enthusiasm he has for science and research were contagious and motivational.

I would like to thank Mark Baevsky for his contribution to the development of the experimental system and for his help in performing the experiments.

A special thanks to my lab partners: Hadar Biran, Hadar Ben-Gida, Katya Barishev, Erez Wenger and Yosef Meller for their professional assistance that created a productive and pleasant work environment. Their genuine friendship and support during times of struggle or when motivation was low, is truly valued.

Last but not least, I would like to thank my family. To my mother, Zhava, who always been a great inspiration for me, for her encouragement, unconditional love and support in every step of the way. To my brothers, Oren and Sharon, and My sister in law, Oranit, for believing in me, offering warm advice and moral support each time I needed. Their enthusiasm and interest in my work have given me the motivation to realize this achievement.

Abstract

Resuspension of particles in liquid environments is an important mechanism in a variety of practical applications, such as: particle filtration, oil production, migration of surface contaminants and transport of hazardous materials in the environment. The phenomena cannot be explained unless the factors causing the incipient motion and the following removal of particles from surfaces are understood in details. Despite a significant progress in the field of resuspension during the past decades, the relation between turbulent flow and particle motion are yet to be fully understood and description of the mechanisms responsible for particle incipient motion remains a challenge. This is partially due to the technical difficulties to quantify the local flow properties and the forces applied on the particles with synchronized high resolution data of particle displacement.

This work present three-dimensional experimental measurements of the necessary conditions for initial entrainment of freely, spherical particles from smooth bed into a turbulent flow without mean shear, in an oscillating grid chamber. Simultaneous measurements of local flow conditions, forces and entrainment of test particles were preformed using 3D-PTV technique. In addition, particle image velocimetry (PIV) technique was utilized to obtain detailed turbulent flow field measurements near the bed.

Turbulence generated under the grid was not isotropic nor homogeneous. Turbulent statistics could for the first time be linked directly to the moment of lift off and to the local flow properties. Lift-off events occur concomitantly to high Reynolds stress, horizontal velocity fluctuations (u_{rms}) and absolute value of horizontal mean velocity. In comparison with known models for resuspension under OGT, it was found that most particles were lift-off a long period of time after the threshold value of LFKE (local fluctuating kinetic energy) was reached .Therefore, LFKE can be considered only as a necessary but not as a sufficient condition in order to compare lift-off events. The pressure, inertia, Basset, drag and Lift forces were calculated from the Lagrangian acceleration of the test particle and the local fluid surrounding it. It was found that the turbulent lift was the dominant force in this study, moreover the Basset force can not be neglected in the problem of resuspension

of freely sliding or rolling particles. Two consecutive high peaks in the vertical average values of pressure and Basset forces were observed before the lift-off of the test particles. Both peaks, to the best of our understanding, point out a possible trigger for lift-off events.

Table of Contents

List of Figures	vii	
List of Tables	xi	
1:	Introduction	1
2:	Literature review	4
2.1	Macroscopic threshold criteria	4
2.1.1	Shields diagram	4
2.1.2	Bagnold and Engelund threshold criteria	6
2.2	Particle equation of motion	7
2.3	Forces measurements on sediment particles	9
2.4	Oscillating grid turbulence	11
2.5	Non-intrusive experimental methods	15
2.5.1	Particle Image Velocimetry (PIV)	15
2.5.2	3D-Particle Tracking Velocimetry (3D-PTV)	18
3:	Methods and materials	24
3.1	Test particles	25
3.2	Particle Image Velocimetry (PIV) method	27
3.2.1	Experimental setup	27
3.2.2	Time diagram in PIV	28

3.2.3	Post processing	29
3.3	3D-PTV method	30
3.3.1	Experimental setup	30
3.3.2	Calibration	31
3.3.2.1	Static calibration	32
3.3.2.2	Dynamic calibration	32
3.3.3	3D- PTV post processing	33
4:	Results	34
4.1	Settling test results	34
4.2	Visualization results	34
4.3	Flow field characterization	36
4.3.1	Mean flow	37
4.3.2	Turbulent flow properties	41
4.3.2.1	Length and time scales	45
4.4	Lagrangian results (3D-PTV)	47
4.4.1	Comparison with PIV results	48
4.4.2	Defining the lift-off events	50
4.4.3	Correlations	52
4.4.4	Vertical velocity	54
4.4.5	Turbulent kinetic energy	55
4.4.6	Forces	58
5:	Summary and discussion	65
6:	Conclusion	69
6.1	Research limitation and recommendations for future work	69
References		72

Appendix A:	Measurement uncertainty	77
Appendix B:	Velocity convergence plots	84

List of Figures

2.1	The Shields diagram [49]	6
2.2	General description of PIV setup	16
2.3	Radial shift for compensation of multimedia geometry	21
2.4	Epipolar geometry, two cameras view.	22
3.1	(a) Oscillating grid chamber apparatus (b) Oscillating grid, $f_{solid} = 0.8$. .	25
3.2	Flow field characterization (PIV) and 3D-PTV measurement areas	26
3.3	Electronic microscope image of a test particle	26
3.4	Settling velocity experiment setup. x_2 represents the measured settling distance, x_1 represents the distance between the water surface and the mark for the beginning of the measuring.	26
3.5	PIV Experimental setup scheme	28
3.6	PIV timing parameters diagram	29
3.7	3D-PTV Experimental setup scheme	30
3.8	The two calibration methods : (a) Static calibration body as was captured at the same time by the four CMOS cameras (b) Dynamic calibration using a dumbbell, seen in the frame of one of the cameras during the calibration recording.	33
4.1	Settling velocity of test particles.	35
4.2	(a) Initial pick-up time [sec] (b) Pick-up ratio: number of picked-up particles divided by the total number of particles in the field of view.	36

4.3 Instantaneous velocity fields for frequency of 2.1Hz, x and y axis are normalized by the width of the grid's chamber, L . (a) Contours of horizontal velocity component $u(x,y)$. (b) Contours of vertical velocity component $v(x,y)$	38
4.4 Mean flow profiles as a function of x axis normalized to the width of the grid's chamber :(a) Mean horizontal velocity component [mm/s] (perpendicular to the grid's movement U). (b) Mean vertical velocity component [mm/s] (parallel to the grid's movement V).	39
4.5 Coordination between the locations of lift-off events and mean flow properties: (a) Mean horizontal velocity component [mm/s] (b) Mean vertical velocity component [mm/s] (c) Mean velocity magnitude [mm/s]. Red mark - area where most lift-off events occurred, yellow - few events occurred and black - none of the events occurred.	40
4.6 Fluctuating flow properties as a function of x axis normalized to the width of the grid's chamber.(a) u_{rms} of the fluctuating velocity [mm/s] (b) v_{rms} of the fluctuating velocity [mm/s] (c) Reynolds [Pa].	42
4.7 Coordination between the locations of the lift-off events and fluctuating flow properties. (a) u_{rms} [mm/s] (b) v_{rms} [mm/s] (c) Reynolds [Pa]. Red mark - area where most lift-off events occurred, yellow - few events occurred and black - none of the events occurred.	43
4.8 Longitudinal correlation of velocity fluctuations for the 4 frequencies.(a) $R_{uu}(x)$ (b) $R_{vv}(y)$	46
4.9 Taylor Reynolds number , Re_λ , versus the pick-up ratio.	48
4.10 (a) Isometric sketch of a Lagrangian trajectory of a resuspended particle. (b) Position [mm], velocity [mm/s] and acceleration [mm/s ²] of a resuspended particle during the incipient motion and lift-off phases.	48
4.11 Comparison between PDFs of instantaneous velocity components measured by PIV and 3D-PTV for frequency of 1.5Hz. (a) Horizontal velocity component. (b) Vertical velocity component.	49
4.12 Comparison between PDFs of instantaneous velocity components measured by 3D-PTV at two different heights from the bottom of the chamber, for frequency of 1.5 Hz.	50
4.13 Position,velocity and acceleration (on y axis) of a re-suspended particle during lift-off.	51

4.14 PDFs of flow tracers at distance of up to 25 mm from the particle, at three different time steps: During lift-off, 0.03s and 0.06s before lift-off. (a)Velocity components. (b) Acceleration components.	52
4.15 Spatial distribution of the location of lift-off events on x-z plane for 4 frequencies of the grid. Axis are normalized by the length of the grid chamber.	52
4.16 Lagrangian particle-fluid velocity correlations description: small circle denotes one of the flow tracers and the large circle represents a test particle.	53
4.17 Particle-fluid velocity correlation functions at the moment of lift-off as a function of the distance [mm] particle-tracer, for $f = 1.5\text{Hz}$	54
4.18 Local R.M.S vertical velocity around the resuspended particles,along their trajectories, for all frequencies. Velocity values are normalized by settling velocity of test particles. Trajectories are shifted along the time axis, so the moment of lift off (marked in red) will be located at zero. The blue line describe the average of all the trajectories at the same frequency. (a)1.5 Hz (b)1.7 Hz (c)1.9 Hz (d)2.1 Hz.	56
4.19 Local average fluctuating kinetic energy measured along the trajectory of the resuspended particles. Trajectories are shifted in respect to the lift-off event (marked by the red stars). (a) 1.5 Hz (b) 1.7 Hz (c) 1.9 Hz (d) 2.1 Hz.	57
4.20 (a) presents an isometric sketch of a Lagrangian trajectory of a particle demonstrating the magnitude and direction of the forces acting on the particle at each time step, obtained for frequency of 1.7 Hz. (b) Magnitude of the forces acting on the particle in time, moment of lift-off is marked in red.	60
4.21 Forces acting on the particle in time, obtained for frequency of 1.7 Hz, moment of lift-off is marked in red. (a) Vertical forces (b) Horizontal forces.	61
4.22 Vertical (y axis) component of the first term in the inertia force. Trajectories are shifted along the time axis, so the moment of lift off (marked in red) will be located at zero. The blue line describe the average of of all the trajectories at the same frequency of the grid. (a) 1.7 Hz (b)1.9 Hz.	62

4.23 Vertical components of first term ($-m_p a_p$), second term (apparent mass force) of inertia force, pressure and Bassett force. Each line presents the average quantity of all trajectories at the same frequency. (a) 1.7 Hz (b) 1.9 Hz.	63
4.24 Vertical and horizontal components of F_t force (the sum of lift and drag forces) acting on the particle along its trajectory. Trajectories were shifted along the time axis, so the moment of lift off will be located at zero. Moment of lift-off is marked in red and the blue line describes the average force of all the trajectories at the same frequency of the grid. (a) Vertical, 1.5Hz (b) Vertical, 2.1Hz (c) Horizontal, 1.5Hz (d) Horizontal, 2.1Hz.	64
B.1 Cumulative average of instantaneous velocity as a function of the number of instantaneous velocity maps for four frequencies of the grid [mm/s] (a) Horizontal velocity. (b) Vertical velocity.	85

List of Tables

4.1	Diameters of 10 test particles that were used in the settling test.	34
4.2	Horizontal and vertical turbulent intensity of the four frequencies.	44
4.3	Expected r.m.s. velocity fluctuations according to Hopfinger and Toly [18] empirical relationship	44
4.4	Kolmogorov and Taylor length and time scales.	47
A.1	Estimated particle and tracers velocity error [m/s].	81
A.2	Estimated particle and tracers acceleration error [m/s^2].	81

Nomenclature

ΔZ_o Light sheet width

ε Turbulent energy dissipation

$\widehat{u_i(t)}$ Filtered velocity signal

L_{ij} Integral length scale

R_{11} Longitudinal correlation function of velocity components.

$x_i(t)$ Position signal

R_{22} Transverse correlation function of velocity components.

$u(x,y)$ Instantaneous horizontal velocity

$u_{rms_{cr}}^*$ Peak value of critica r.m.s velocity

$v(x,y)$ Instantaneous vertical velocity

$3D - PTV$ Three dimensional Particle Tracking Velocimetry

\bar{u} Local average of velocity component

Δs Probable displacement of imaged particles between two images

Δt Time intrerval

δ_v Thickness of the viscous sublayer

η	Kolmgorov length scale
λ	Taylor micro-scale
μ	Dynamic viscosity
ν	Kinematic viscosity
ρ_l	Density of liquid
ρ_p	Density of particle
τ_0	Shear stress
τ_η	Kolmgorov time scale
τ_c	Critical bed shear stress
τ_s	Relaxation time
τ_T	Reynolds stress
Θ^*	Modified Shields parameter
θ_{cr}	Critical Shields parameter
Δ_0	Average particle spacing . $\Delta_0 = p_N^{-1/3}$
ς	Anisotropy coefficient
$\widehat{a_i(t)}$	Filtered acceleration signal
a_{if}	Fluid acceleration
a_p	Particle acceleration
C_1, C_2	Constants that depend on the geometric parameters of the grid.
C_3	Form coefficient defining the effective surface area of the particle
C_t	Number density of tracing particles

d_a	Average particle diameter
D_I	Interrogation window length
d_p	Particle diameter
f	Frequency of oscillation
F_a	Added mass force
F_b	Basset history force
f_{cr}	Critical frequency
F_d	Drag force
F_g	Buoyancy force
F_i	Inertia force
F_l	Lift force
F_p	Pressure force
f_r	Frame per second rate
f_{solid}	Solidity of the grid
F_s	Stokes drag force
F_t	Total force
g	Gravitational acceleration $g= 9.81[\text{m/s}^2]$
h	Grid height
I, I'	Pixel intensity value
I_u	Horizontal turbulent intensity
I_v	Vertical turbulent intensity
IA	Interrogation Area

L	Width of the grid chamber
l	Integral length scale
L_{lines}	Settling distance
$LFKE$	Local Fluctuating kinetic energy
M	Mesh size of the grid
m_a	Added mass coefficient
m_f	Fluid mass
M_o	Magnification ratio
m_p	Particle mass
N	Number of velocity vector fields
$n(t)$	Number of particles on the surface at time t
N_f	Number of frames
N_{IA}	Magnification ratio
NI	Image density
OGT	Oscillating Grid Turbulence
P_N	Number of particles per unit volume
PIV	Particle Image Velocimetry
r	Distance vector
$R_{ij}(r)$	Velocity correlation function.
r_i	Radius of search volume
R_{nn}	Prependicular correlation coefficient of velocity vectors.
$R_{pf}(r)$	Fluid - particle correlation coefficient.

r_p	Particle radius
R_{rr}	Correlation coefficient of velocity vectors projection on distance vector r.
Re_λ	Taylor-Reynolds number
Re_p	Particle Reynolds number. $Re_p = \frac{\sqrt{g(s-1)d_p^3}}{v} = \frac{u*d_p}{v}$.
Re_w	Particle settling velocity Reynolds number . $Re_w = \frac{W_S d_p}{v}$
s	Particulate density ($\frac{\rho_p}{\rho_l}$)
s_l	Stroke length of the grid
s_d	Standard deviation
S_N	Cummulative average
St	Strouhal number
t	Time
TKE	Turbulent Kinetic Energy
u', v'	Velocity fluctuations
U, V	Mean velocity vector
u, v	Instantaneous velocity
u_{cr*}	Critical bed shear velocity.
u_f, v_f, w_f	Flow tracer velocity
U_{mag}	Velocity magnitude
u_p	Particle velocity
U_{rev}	Relative velocity between the particle and the fluid
$u_{rms_{cr}}$	Critical r.m.s velocity
u_{rms}, v_{rms}	R.M.S of velocity fluctuations

u_t Local fluctuating velocity component

V_p Particle volume

W_s Settling velocity

z Distance from the center of oscillation

PDF Probability distribution function

1 Introduction

This thesis studies the process of particle release from a surface into the surrounding fluid flow which is commonly called "resuspension" or "reentrainment". Resuspension of particles in liquid environments is an important mechanism in a variety of practical applications, such as: particle filtration, oil production, migration of surface contaminants, detection of explosives, transport of hazardous materials in the environment, pneumatic conveying and particle behavior in respiratory ways [39]. Particle resuspension cannot be explained unless the factors causing the incipient motion and the following removal of particles from surfaces are understood in details. The complexity of the phenomena is due to two inherent features: particle interaction with the surface to which it is attached, and particle interaction with the fluid to which it is exposed. The particle is held on the surface by a combination of attraction forces, chemical bonds and mechanical stresses, which are usually referred to as adhesion forces. Particle interaction with the fluid depends on the fluid properties and the flow regime [54]. Moreover, incipient motion can be one of few different categories, such as motion along the surface (rolling or sliding), saltation (short periods of resuspension and following deposition) or full suspension (called lift-off or pick-up), each category has different critical conditions [54].

Different criteria and models have been proposed to define the threshold conditions for particle incipient motion. Early models have focused on balancing the forces acting on a particle in flow: the hydrodynamic lift and drag, submerged weight of the particle, adhesion and bed friction. One of the first models is the seminal work of Shields [41]. The so-called Shields diagram relates the threshold conditions for a particle of nominal diameter d_p to the dimensionless Shields parameter $\theta_{cr} = \tau_c/(\rho_p - \rho_l)gd_p$, where τ_c is the critical bed shear stress, ρ_p, ρ_l are densities of particle and liquid respectively, g is the acceleration due to gravity. The Shields diagram is developed for uniform steady flow conditions and considers the mean bed shear stress τ_0 as a single integral parameter for determining the hydraulic forces acting on the stream bed [50]. It was found, however that θ_{cr} obtained from the Shields diagram often yields poor and inconsistent results when

applied to real or more complex flows that involve spatial or temporal accelerations [35, 44, 31]. This discrepancy may arise because naturally occurring flows are often neither uniform, nor statistically stationary, with the near bed turbulence quantities varying with time and space [50]. Moreover, the distribution of turbulence quantities can significantly differ between flows having identical values of average parameters such as bed shear stress[40].

Despite a significant progress in the field of resuspension during the past decades, the relation between turbulent flow and particle motion are yet to be fully understood and description of the mechanisms responsible for particle incipient motion remains a challenge. This is partially due to the technical difficulties to quantify the local flow properties and the forces applied on the particles with synchronized high resolution data of particle displacement. In most experimental studies on resuspension, only macroscopic quantities, such as the rate of resuspension or particle concentration above the bed, are measured. Better understanding requires careful and direct experimental measurements to define the local flow-particle interaction accurately [40, 8].

Schmeeckle et al. [40] preformed measurements using a force transducer directly connected to a particle. Although the method allows measurement of force components on a particle in turbulent flows, this mechanical approach applicable to relatively large particles. Additionally, the method requires the particle to be stationary and therefore can represent the instant of initiation of sliding or rolling. During lift-off the particles could be already moving along the surface, so the forces can be different from the forces acting on stationary particles measured by a force transducer. Three dimensional particle tracking velocimetry (3D-PTV) can potentially overcome the limitation of direct force measurement. The method can provide quantitative observation of individual particle movement in 3D with additional information about the local turbulent flow [17].

The scope of the present thesis is to explore the necessary conditions for initial entrainment of spherical particles from a smooth bed into a turbulent flow without mean shear, in an oscillating grid chamber. Simultaneous measurements of local flow conditions and entrainment of test particles are preformed using 3D-PTV technique. In addition, particle image velocimetry (PIV) technique is utilized to obtain detailed flow field measurements near the bed and to investigate how the statistical properties of turbulence affect particle lift-off rates. The experiments were not designed to fully mimic the problem of resuspension in streams and channel flows, but rather identify key mechanisms that lead to the lift off of a free, mobile particles, utilizing direct measurements of particle motion before and during lift-off events. The combination of velocity field near the bed measured by PIV, with 3D Lagrangian trajectories of flow tracers and of individual solid particles measured

by 3D-PTV at sufficiently high frame rate, before and during lift-off can contribute to a better understanding of the dominant mechanisms that cause lift-off and better description of the role various hydrodynamic forces play in this process.

2 Literature review

This chapter reviews briefly the most relevant literature for the present study, including experiments, theoretical models of particle motion and numerical studies. Majority of experimental studies on resuspension focused on macroscopic quantities, such as rate of resuspension or particle concentration above the bed. The number of particles entrained by the flow can be counted by various means. One way is to photograph the surface upon which the particles are initially deposited before, during and after an experiment and compare the respective particle counts. Another way is to collect suspended particles using a filter placed at the end of a wind tunnel or similar device [34]. It is also possible to estimate the suspended particle concentration by relating the range of known concentrations to their measured attenuation of light intensity [38]. These macroscopic measures can lead to the criteria of incipient motion.

2.1 **Macroscopic threshold criteria**

2.1.1 *Shields diagram*

Shields [41] work on incipient motion and bed-load transport is a benchmark study that is widely applied in fields such as hydraulic engineering [15]. Shields [41] expressed incipient grain motion as a dimensionless ratio of the critical bed-shear stress (τ_c) to submerged grain weight per unit area as shown in Eq.2.1.

$$\theta_{cr} = \frac{\tau_c}{(\rho_p - \rho_l)gd_a} = \frac{u_{cr}^{*2}}{(s - 1)gd_a} \quad (2.1)$$

Where θ_{cr} is the corresponding dimensionless critical shear stress also known as the Shields parameter, $s = \rho_p / \rho_l$ is the specific weight of sediment and $u_{cr}^* = \sqrt{\tau_c / \rho_l}$ is the critical bed shear velocity.

Shields parameter can be developed by a simple analytical approach of force balance

model. Under critical conditions, the hydrodynamic forces acting upon an exposed particle are just balanced by the resisting force of the particle. The forces acting upon a particle over which a fluid is flowing are the submerged weight of the particle, the lift force, the drag force and bed friction. A fully developed, turbulent flow condition is assumed and the drag force is expressed as:

$$F_D = \tau_0 C_3 d_p^2 \quad (2.2)$$

Where τ_0 is the bed shear stress, $C_3 d_p^2$ is the effective surface area of the particle exposed to the shear stress τ_0 .

A dimensional analysis of the threshold condition for the incipient particle motion yields that the critical shear stress is a function of particle Reynolds number only [15]:

$$\theta_{cr} = \frac{\tau_c}{(\rho_p - \rho_l) g d_a} = f \left(\frac{u_{cr}^* d_p}{v} \right) \quad (2.3)$$

This Reynolds number can be also seen as the boundary layer Reynolds number, which represents both the thickness of the viscous sublayer, δ_v , and the hydrodynamic conditions of the flow around the surface grains [15]. When the Reynolds number is low, the particles are fully embedded in the viscous sublayer.

The determination of θ_{cr} provides an approximation of the conditions under which particle is brought into motion from being stationary. Many experiments have been conducted to develop an explicit solution of Eq. 2.3. The earliest one is the graphical presentation given by Shields [41] and is known as the Shields diagram, see Fig.2.1.

Shields [41] conducted laboratory open channel flow studies examining incipient motion and bed-load transport of not cohesive, nearly uniform grains. Shields did not give much explanation on how he obtained critical shear values, however, most authors who investigated his work, report that he determined critical shear stress, θ_{cr} , by reference-based method extrapolation paired measurements of shear stress and bed-load transport rate to a zero level of sediment transport [6, and the references therein].

Shields identified the limit of three regions in his diagram in terms of bed roughness: smooth, transitional and rough: hydraulically smooth when $Re_p < 2$ means $d_p < \delta_v$ and particles are fully submerged within the viscous sublayer, transitional when $2 \leq Re_p \leq 500$ and rough when $Re_p > 500$ i.e.: $d \gg \delta_v$, the laminar sublayer gets interrupted by existing bed roughness of the grains. Shields had no data for the smooth and rough regions. For the transitional region, a considerable scatter is observed in the original diagrams.

The Shields diagram is based on uniform steady flow conditions, as it considers the mean boundary shear stress as the only integral parameter for determining the hydraulic

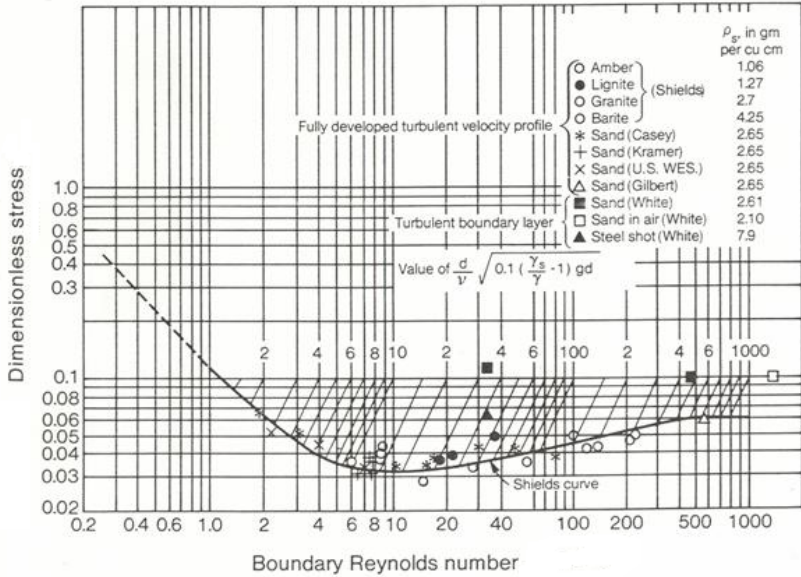


Figure 2.1: The Shields diagram [49]

forces acting on the bed. A number of researchers found that using θ_{cr} obtained from the Shields diagram sometimes yields poor and inconsistent results when applied to real or more complex flows that involve spatial or temporal variations in the flow [35, 44, 31]. Despite this, the Shields diagram is still the most widely used and accepted criterion.

2.1.2 Bagnold and Engelund threshold criteria

While Shields diagram refers to the beginning of bed-load movement of all types (rolling/sliding/ lift-off, etc.) Engelund and Bagnolds [12, 2], proposed one of the first criteria to estimate the beginning of suspension (lift-off or pick-up). Their criteria was based on the assumption that particles remain in suspension as long as the turbulent lift force acting over the particles exceed the forces that oppose particle motion, such as gravitational and viscous forces [32]. Therefore, in order to suspend particle from bed, the vertical fluctuations, v_{rms} , must exceed a critical value of the submerged weight of the particles, i.e. the criteria can be formulated as: $v_{rms_{cr}} > w_s$. The authors [12, 2] expressed the critical vertical fluctuation velocity by the critical shear velocity u_{cr}^* and thus: $u_{cr}^* = \alpha w_s$. Bagnolds [2] suggested $\alpha = 0.75$ for the initial suspension and $\alpha = 1.4$ for full suspension, Engelund [12] suggested $\alpha = 0.25$. Zanke [53] proposed a way to explain the different values of α . Vertical fluctuations are of different strength and different probability of exceeding. While Bagnolds [2] refers to frequent and weak fluctuations, which can be

interpreted as considerable suspension, Engelud [12] refers to rare but strong fluctuations that can be interpreted as a first suspension. However, their approach was based on a constant relation between the near bed vertical turbulent velocity and the bed shear velocity and did not take the near bed turbulence characteristics into account. Therefore, their criteria underestimated the threshold conditions where the flow conditions are not hydraulically rough [53]. Later on, Van Rijn [48], based on experimental results, suggested a range of limit conditions for which sediment particles are lifted from the bed into suspension: if the particle parameter, $D^* > 10$ (calculated according to 2.4), then $\alpha = 0.4$. if $D^* < 10$, than u_{cr}^* has relatively higher values $\alpha = \frac{40}{D^*}$ [53] .

$$D^* = d_a \left[\frac{(s-1)g}{v^2} \right]^{1/3} \quad (2.4)$$

However, Van Rijn [48] condition did not take into account the influence of external turbulence and therefore might underestimate the pick-up rates in natural flows and industrial applications such as mixers.

Different approaches to address the incipient motion have been developed over the years, both numerical and experimental. These methods addressed the forces acting on the sediment particle directly, focusing on the hydrodynamic forces. The studies refer first to the hydrodynamic forces, presented in the particle equation of motion. The major goal is to simulate or to measure the sum of the forces (i.e. the acceleration of the particle) and sometimes also the separate force terms in order to emphasize key physical processes that lead to resuspension.

2.2 Particle equation of motion

Maxey and Riley [25] presented the equation for the motion of a small sphere in a nonuniform flow based on the previous development of Corrsin and Lumely [9]. The Corrsin and Lumely [9] equation is :

$$m_p \frac{du_p}{dt} = m_f \left(\frac{Du_f}{Dt} - v \nabla^2 u_f \right) - 0.5 m_f \frac{d}{dt} U_{rev} - 6\pi r_p \mu U_{rev} - 6\pi r_p^2 \mu \int_{-\infty}^t \frac{dU_{rev}/d\tau}{\sqrt{\pi v(t-\tau)}} d\tau + (m_p - m_f) g \quad (2.5)$$

Where u_p represent particle velocity, m_p the mass of the particle with radius r_p , u_f represent the undisturbed fluid velocity at the particle center position, m_f the mass of fluid displaced by the particle, $U_{rev} = u_p - u_f$ represents the relative velocity between

the particle and the fluid. The derivatives $\frac{d}{dt}$ is used to denote a Lagrangian derivative following the moving particle while $\frac{D}{Dt}$ represent Lagrangian derivative of the moving fluid element.

$$\frac{d}{dt} = \frac{\partial}{\partial t} + \mathbf{u}_p \cdot \nabla \quad (2.6)$$

$$\frac{D}{Dt} = \frac{\partial}{\partial t} + \mathbf{u}_f \cdot \nabla \quad (2.7)$$

The terms on the right side of Eq. 2.5 are different forces acting on the particle: the pressure gradient force F_p , added-mass force F_a , stokes drag F_s , Basset history term F_b and buoyancy F_g . The motion equation was developed for an isolated particle in the bulk of a flow, far from any boundary so that particle-particle and particle-boundary interactions are excluded.

The formulation of Maxey and Riley [25] keeps the buoyancy term but replaces the added mass, Basset and the Stokes drag terms with expressions modified by the Laplacian of fluid velocity (also known as the Faxen correction) due to curvature in the velocity profile. The pressure term is also modified:

$$F'_p = m_f \frac{Du_f}{Dt} \quad (2.8)$$

$$F'_a = -0.5m_f \left(W - \frac{r_p^2}{10} \nabla^2 u_f \right) \quad (2.9)$$

$$F'_b = -6\pi r_p^2 \mu \int_{-\infty}^t \frac{d(W - \frac{r_p^2}{6} \nabla^2 u_f)/d\tau}{\sqrt{\pi\nu(t-\tau)}} \quad (2.10)$$

$$F'_s = -6\pi \mu r_f \left(W - \frac{r_p^2}{6} \nabla^2 u_f \right) \quad (2.11)$$

The development of the equation of motion relies on the assumption that the particle is much smaller than the smallest scales of the flow, however in cases where the particle is smaller than a few Kolmogorov length scales, the error this assumption introduces is not significant [5, 47]. Simulations [7] have shown that the Faxen correction becomes significant only for particles with diameter of several times the dissipative length scale of the flow.

The Basset history term accounts for the viscous effects, it addresses the temporal delay in boundary layer development as the relative velocity changes with time. In the classical definition, it must be calculated between the initial time and current time. However, since the earlier moments give smaller contribution, it can be calculated approximately during a few of the last particle time steps. The Basset force is usually neglected, in several cases because it was found negligible, see for example Sridhar and Katz [42], while in other since it is computationally expensive or not accessible experimentally. Recent investigations show that the Basset force is important for relatively small particles moving close to solid boundaries and must be included in Lagrangian models of bed-load transport of particle settling velocity Reynolds number ($Re_w = \frac{W_s d_p}{v}$) smaller than about 4000 [20, 4] and when the density ratio between particle and fluid, i.e.:s, is of the order 1-10 [33].

2.3 Forces measurements on sediment particles

Several studies propose that particles motion is predominantly driven by the magnitude of fluctuating drag and lift forces exerted on exposed particles [40, 11]. These fluctuating forces are directly related to the instantaneous fluctuating velocities indicating that the turbulence structure at near bed is ultimately responsible for particle motion [26]. It has been suggested that the critical motion is best represented by the maximum forces acting on the particles rather than the mean bed shear stress [16]. Furthermore, It has been shown that the duration of the period of force can be also critical [8]. For turbulent simple shear flows in the streamwise direction parallel to the plane bed, the hydrodynamic drag term appears to be dominant, e.g. [40]. Nelson et al. [31] have reported a strong correlation between bed load flux sediment rate and streamwise velocity fluctuations, often associates with the drag force, near the bed while vertical velocity fluctuations, often associated with lift force, are poorly correlated with the flux of sediment. In general it can be summarized that the effect of drag force has received considerable attention in sediment research, while the role of lift is less well understood. Therefore, there are no reliable quantitative relationships for lift force, which could be used for the determination of sediment threshold condition [11].

Schmeeckle et al. [40] preformed force measurements using a force transducer directly connected to a particle with synchronized flow velocity measurements above or in front of the particle. The force transducer measured the horizontal and vertical components of the force, which are not the same as the hydrodynamic drag and lift. His results showed that the horizontal force was well correlated with the downstream velocity and not

correlated with the vertical velocity. The standard drag formula worked well to predict the horizontal force. However, vertical force correlated poorly with downstream velocity and vertical velocity. Overall their measurements suggested that the process producing lift on particles in near-bed turbulent flow are not captured by the simple models for lift in uniform flows. Schmeeckle et al. [40] and Dwivedi et al. [11] who also preformed a study on the hydrodynamic lift force using a force-sensor, suggested that the lift force is produced primarily by pressure gradient in the flow, which can arise from externally imposed unsteadiness, spatial accelerations or turbulent fluctuations. If a local turbulent structure produces high pressure on the bottom of the particle and low pressure on the top, the vertical acceleration force will be large and high lift event will occur. This mechanism was also suggested by Zanke [53] as possible way to bring particle into a start position for suspension.

A study by Sridhar and Katz [42] reported force measurements obtained from bubbles position in a laminar vortex using Maxey and Riley [25] equation of motion. In this study neighboring bubbles were used to estimate the fluid velocity in the vicinity of other bubbles. The equation for balance of forces was defined as:

$$0 = F_g + F_p + F_i + F_b + F_d + F_l \quad (2.12)$$

Where the terms in the right side are, in order, buoyancy, pressure, inertia, Basset, drag and lift. The inertia force was calculated as follows

$$F_i = m_p \frac{du_{pi}}{dt} - F_a \quad (2.13)$$

The Basset force and Faxen correction were neglected and the Stokesian drag was replaced with a general drag term and an additional lift term. The procedure involved calculations of the pressure, inertia, and buoyancy forces using velocity measurements and balancing their resultant force (F_t) with lift and drag forces. Drag is parallel to the relative velocity U_{rev} between the particle and the fluid and the lift is perpendicular to it.

$$F_d = \frac{F_t \cdot U_{rev}}{|U_{rev}|} \quad (2.14)$$

$$F_l = F_t - F_d \quad (2.15)$$

The measured drag and lift forces were used to compute the trajectory of a bubble and

compared with the experimental observation. The results of the study was successful in terms of the trajectory method. Although, the study was preformed on bubbles, with 2D measurement and in laminar flow, its ideas can serve as a good basis for quantitative, 3D measurement of forces in turbulent flows.

Furthermore, it is important to point out that it is difficult to compare forces obtained by various researchers because of variation in velocity-measurement location, estimation of particle area expose to the flow and the choice of velocity for calculations (shear or streamwise velocity) and type of flow, see e.g. Dwivedi et al. [11].

2.4 Oscillating grid turbulence

As a result of decades of work, the literature acknowledges the significance of turbulent-particle interaction, taking place in the near bed region of the flow, on mobilizing the particles at incipient motion. For example, Nearing and Parker [30] have shown that detachment rates of particles were dramatically greater for turbulent flow case compared to laminar case. Sumer et al. [44] who examined the influence of external turbulence on sediment transport, reported that the particle transport increases markedly with increasing turbulence level. Therefore, improvement in our understanding of the resuspension process, requires a detailed knowledge of how turbulent fluctuations interact with and mobilize particles [50].

In the past three decades, researchers have employed oscillating grids in mixing boxes (chambers) as a simple field to investigate the effect of turbulence on: particle resuspension [3, 34], particle lift-offs [27], desorption of compounds from resuspended sediment and diffusion of particulate matter in water [3]. In those experiments the turbulence was generated in a water chamber by a uniform, mono-planar grid, oscillating perpendicular to its plane. The grid consisted of an array of bars and was positioned below the water surface. Turbulence produced in this way was characterized by fluctuations that were dominant compared to the mean flow, which allowed the interaction between the sediment and near-bed turbulent to be studied [50].

The statistical properties of this class of “zero-mean-shear” turbulence, commonly referred to as oscillating grid turbulence (OGT), have been studied extensively in the work of Hopfinger and Toly [18], Fernando and De Silva [14]. Turbulence is generated near the grid by the development of jet and wake structures, corresponding to the open areas and the grid bars. Immediately near the grid, the intensity of turbulence tends to increase because of the presence of shear. If the grid is properly designed, beyond a certain distance downstream, the mean shear induced by the jets and wakes becomes insignificant because

of their merger into one another, whence the turbulence begins to decay. The initial flow development region typically lasts for about $2\text{-}3 M$ downstream (M is the mesh size of the grid- defined as the distance between the centers of two neighboring openings). Further downstream, the turbulence is nearly homogeneous in planes parallel to the grid and the ratio of the horizontal (streamwise) turbulent velocity to vertical (spanwise) turbulent velocity is typically in the range of $1.05 \div 1.35$. The turbulence so produced is considered quasi-isotropic [13].

The oscillating grid turbulence depends on various parameters: The distance to the center of oscillation, z , the stroke length, s_l , the frequency of oscillation f , the mesh size, M , and the grid solidity (defined as the ratio of the area of bars to the total area of the grid). In order to produce, statistically stationary, zero-mean turbulence certain design conditions have to be satisfied: grid solidity less than 40% and oscillation frequency between 0.5-7Hz. Also, the grid-end should be designed to satisfy a reflection-symmetry condition, with respect to the wall for reducing the formation of mean secondary circulation. For other designs and different combinations of these parameters, the wake and jet structures behind the grid bars can become unstable, and rather than uniformly spreading into each other, deflect and merge to form few stronger jets, which can result in strongly inhomogeneous turbulence [13].

For a grid of square bars, which follows the specified restrictions, it has been shown by Hopfinger and Toly [18] that the decay of the time-averaged r.m.s velocity fluctuations in horizontal (u_{rms}, w_{rms}) and vertical (v_{rms}) directions can be described by Eqs. 2.16 and 2.17:

$$w_{rms} = u_{rms} = \sqrt{\overline{u'^2}} = C_1 s_l^{1.5} M^{1/2} f z^{-1} \quad (2.16)$$

$$v_{rms} = \sqrt{\overline{v'^2}} = C_2 s_l^{1.5} M^{1/2} f z^{-1} \quad (2.17)$$

where C_1 and C_2 are constants that may depend on the geometric parameters of the grid. Hopfinger and Toly [18] reported values of C_1 and C_2 of approximately 0.25 and 0.27, while Fernando and De Silva [14] measured values of approximately 0.22 and 0.26. The turbulence near the grid is not homogeneous, therefore the empirical relationship for the turbulent velocity fluctuations do not hold until one reaches a significant distance from the grid. Various relationship have been proposed for the limiting distance beyond which the equation is applicable. Atkinson et al. [1] concluded that the relationship held for $z > 2M$, while Fernando and De Silva [14] found that for small strokes the relationships help for $z > 4s_l$ [34]. These properties allow to control the turbulence at the top of the sediment

sample by setting operational parameters of the grid: the frequency, the stroke length and the distance between the center of oscillation of the grid to the sample. The advantage for using oscillating grids for studying turbulence is that there is no mean shear. Unlike a boundary layer flow, where uni-directional shear is generated at the fixed boundaries, the oscillating grid produces no net flow direction, and thus no mean shear. Thereby, it allows to examine the effect of turbulent fluctuations on the sediment bed in isolation. Due to the predictable and reproducible nature of the turbulence generated by the oscillating grid, replicate tests of sediment resuspension and chemical fluxes can be readily accomplished [38, 34]. However, with an oscillating grid, the simplification of turbulence represented by a mean boundary shear does not work. Since time averaged mean shear is zero, another robust term to quantify turbulence for the resuspension is required.

Medina et al. [27] performed experiments to show the relation between turbulence and the initiation of sediment motion under OGT. They have found an empirical relation between the critical r.m.s velocity and the particle parameter, D^* . The critical frequency, f_{cr} , was determined as the frequency at which local transport of particles at the bottom was first detected, and the critical r.m.s velocity ($u_{rms,cr}$), was defined using Eq. 2.16 as the r.m.s velocity that produced this movement at the surface of the sample. However, when the critical r.m.s velocity of the zero-mean turbulent was compared to the theoretical critical bed shear velocity, u_{cr}^* (determined using analytical method of Van Rijn [48]) it appeared always lower than the comparable velocities calculated for the Shields parameter.

Lyn [22] has proposed a modification of the traditional Shields parameter in which the incipient of sediment motion in a tank with oscillating grid flow is characterized using a modified Shield parameter, defined as :

$$\Theta^* = \frac{TKE}{g(s-1)d_p} \quad (2.18)$$

Where Θ^* is the modified Shields parameter and the turbulent kinetic energy (TKE) of the turbulence, is defined from the r.m.s velocity fluctuations according to Eq. 2.19.

$$TKE = 0.5(u_{rms}^2 + v_{rms}^2 + w_{rms}^2) \quad (2.19)$$

The idea relies on the assumption that the square of friction velocity, which is proportional to the shear stress, is also a measure of the TKE in a channel flow, hence by replacing this quantity in the conventional Shields parameter by the TKE in the grid generated turbulence, the modified parameter is obtained [3].

Bellinsky et al. [3] have further established the role played by Θ^* , under OGT, and

obtained an approximate relationship between the critical modified Shields parameter and the particle Reynolds number for a range of natural and artificial sediments. They have neglected the effect of the bottom wall, which makes the turbulence anisotropic, and assumed approximate isotropy of turbulence induced by the oscillating grid $u_{rms} = v_{rms} = w_{rms}$, yielding:

$$TKE = 1.5\zeta(u_{rms}^2) \quad (2.20)$$

where ζ is an anisotropy coefficient. By introducing Eq. 2.16 into Eq. 2.20, the authors obtained:

$$\Theta^* = \frac{1.5\zeta C^2 (fs_l^{1.5} M^{0.5} z^{-1})^2}{g(s-1)d_p} \quad (2.21)$$

The critical frequency, chosen as the criterion for incipient motion, was determined in a similar manner as preformed by Medina et al. [27]. The measurements established the form suggested by Lyn [22] for the critical modified Shields parameter and provided values of Θ^* close to the open channel Shields curve, by assuming $\zeta = 1$ and $C = 0.5$.

Recently Wan Mohatar and Munro [50] suggested an improvement to the modified Shields parameter, Θ^* , which take into account the near bed anisotropic conditions created by the present of the sediment layer. They have measured the turbulent fluid velocity field, in the region between the grid and bedform surface, with and without sediment layer using a particle image velocimetry (PIV) set-up. The critical frequency was determined in a similar manner as was preformed by Medina et al. [27]. Although, their grid followed all the restriction described earlier, the presence of the sediment layer had a significant affect on the structure of turbulence, leading to anisotropy in the near bed region: a weak secondary flow and a peak in the r.m.s horizontal velocity component, u_{rms} , were observed in the near-bed region, at the critical frequency. Under anisotropic conditions they exacted the shear stress to scale as $\tau_c \sim \rho_l u_{rms}^{*2}$, where $u_{rms_{cr}}^*$ is the peak value of $u_{rms_{cr}}$ obtained in the near bed region, in contrast to modified Shields parameter, where it is assumed $\tau_c \sim \rho_l u_{rms_{cr}}^2$, with $u_{rms_{cr}}$ given by Eq. 2.16. Therefore, they concluded that the threshold condition for sediment transport can be defined as:

$$\theta_c^* = \frac{u_{rms_{cr}}^{*2}}{(s-1)gd_p} \quad (2.22)$$

Their measurements of θ_c^* were plotted against Re_p and compared with the standard Shields curve. Although, the data trend showed a qualitative agreement with that predicted by Shields curve, the data was a factor of two greater than the values predicted by Shields diagram.

In addition to the literature review of the physical problem of our study, the two non-intrusive, optical measurements methods that will be used in the work, namely the two-dimensional particle image velocimetry (PIV) and the three-dimensional particle tracking velocimetry (3D-PTV) methods and their use are reviewed.

2.5 Non-intrusive experimental methods

2.5.1 Particle Image Velocimetry (PIV)

Particle image velocimetry (PIV) is a quantitative optical measurement technique that provides instantaneous two-dimensional velocity fields. The method is non-intrusive, suitable for both gaseous and liquid flows at a wide range of Reynolds numbers and can provide high resolution data of a whole field. The general principles of the method are illustrated in Fig. 2.2 and can be described as follow. The fluid is seeded with tracer particles. A cross section of the flow field is illuminated at least twice within a short time interval by a thin light sheet pulse. The light scattered from the particles is captured by a highly sensitive camera in a pair of successive frames separated by a known time interval Δt . The frames are divided into small subsections called interrogation areas (IA). For each IA, statistical methods (auto and cross correlation) are used to calculate the most probable displacement Δs of all imaged particles between the two images. Under the assumption that the displacement and time interval between the light pulses are small enough, acceleration effects can be neglected and velocity is then given by the ratio $\Delta s/\Delta t$. Repeating the process for all IA will result in the velocity field. The following paragraphs will describe briefly the main features of the setup and the data processing stage of this measurement technique.

Seeding The method rely on scattering particles suspended in the flow to provide the velocity information for the continuous medium (gas or liquid). The accuracy of the velocity field determination is ultimately limited by the ability of the seeding particles to follow the instantaneous motion of the continuous phase [28]. Therefore, seeding particles should be chosen carefully according to the following considerations. The particles must be small enough to follow the flow, i.e. the density and diameter of the particle should exclude gravity and buoyancy effects, see Eq. 2.5. On the other hand, particle diameter should not be too small as light scattering properties also have to be taken into account. Therefore, a compromise has to be found. Particles can be considered suitable if their relaxation time, τ_s , is significantly lower than the shortest flow time scale. Relaxation time is derived from Stokes drag law as follows [37, 51]:

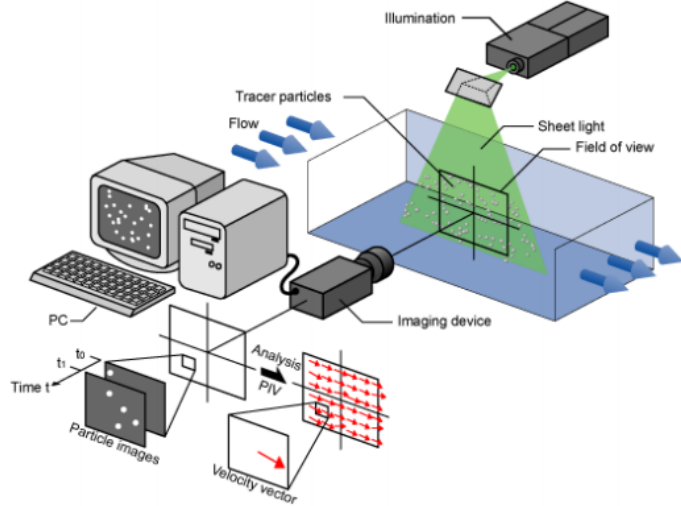


Figure 2.2: General description of PIV setup

$$\tau_s = d_p^2 \frac{\rho_p}{18\mu} \quad (2.23)$$

Although the law is valid for viscous flows with low Reynolds numbers at constant acceleration, the expression is considered a convenient measurement for the behavior of particles in more general flows. Particle concentration must be high enough to enable reliable spatial velocity measurement. In most cases, an amount of 8-10 particles per IA is considered sufficient [37].

Illumination and optics In order to record the light scattered from the seeding particles, a cross section of the flow field is illuminated by a light sheet. The sheet should be thin enough so that only particles at a narrow slice of the flow will be illuminated. The amount of light should be sufficient to detect the particles. The duration of the illumination pulse must be short enough to prevent a significant motion of the particles during the pulse exposure in order to avoid blurring of the image. The time interval between the illumination pulses must be long enough to be able to determine the displacement between the images of the particles with sufficient resolution and short enough to avoid particles living the light sheet between subsequent illuminations .

Lasers are widely used in PIV, because of their ability to emit monochromatic light with high energy, which can be bundled into thin light sheet for illuminating and recording the particles without chromatic aberrations [37, 51, 52]. The various lasers type can be divided into two categories: continuous and pulsed. Continuous weight (CW) lasers, such

as AR-ion, are suitable for low speed flows and require electronic shuttering to pulse the light. Pulsed lasers, such as Nd:YAG, can provide a light pulse with higher intensity where separation of pulses and the repetition frequency can be varied. Pulsed lasers are more robust and are suitable for high speed flows [10]. The generated beam is transformed into a thin sheet using lenses. The optical configuration include a cylindrical lens which expands the laser into a sheet and at least one spherical lens which focuses the sheet to the appropriate thickness.

Image capture and recording techniques Digital PIV recording is usually performed by cameras with a CCD or CMOS sensor. Current CCD technology can provide high spatial resolution, immediate feedback on image quality and instant analysis. The optical axis of the camera should be located perpendicular to the illuminated sheet, in order to record the whole plane in focus. Experimental characteristics such as event speed, repeatability and illumination intensity need to be evaluated for choosing a camera for a specific application, often in combination with the illumination system [43]. The location of the illuminated particles is recorded twice to calculate the displacement. There are two main approaches for PIV recording: single frame/multi-exposure, in which the particle location in both time intervals is recorded on a single frame and multi-frame/single-exposure, in which the particle location in each time interval is recorded on a separate frame. The main advantage of the second approach is that it solves the directional ambiguity, allows higher signal-to-noise ratios in the correlation plane to be available at the same interrogation area [37].

Analysis In the analysis process, a velocity field is calculated from the images by measuring particle displacement between two sequential frames. The steps in the analysis process include: dividing the image into IA, calculating the correlation between two sequential frames, finding the correlation peak with sub pixel accuracy, calculating the velocity vector and repeating the process for all IA of the PIV recording. The particle displacement is assumed to be linear, thus the size of the IA must be small enough that velocity gradients have no significant influence on the results. The probability for a good analysis result is highest when the IA contains about 8 – 10 particle. Furthermore, the size of the IA determines the number of independent velocity vectors and therefore the maximum spatial resolution of the velocity map. Overlapping of adjacent IA can be used to increase resolution between measured displacement points. An overlap of 50% is considered a good balance between information density and over-sampling [37].

The displacement is calculated using statistical methods which estimate the best match

between image pairs. Analysis of data captured at a double frame/single exposure technique is performed using a 2D discrete cross-correlation function [37]:

$$R(x, y) = \sum_{i=-K}^{i=K} \sum_{j=-L}^{j=L} I(i, j) \cdot I'(i + x, j + y) \quad (2.24)$$

Where I, I' are the pixel intensity values in each frame and K, L are the dimensions of the IA. The correlation for each image shift is determined by the sum of all over lapping pixel intensity products. Analysis of single frame/double exposure data is performed using auto-correlation which is a specific case of cross-correlation. The calculation of the cross correlation function requires many multiplications and consumes substantial computational resources. The alternative is to use the fast Fourier transform algorithm (FFT), which can significantly reduce the computational operations. In most application, each IA is transformed from the spatial to the frequency domain using FFT. In the frequency domain a conjugate multiplication between the transform results from both images takes place, and the product is transformed back to the spatial domain using an inverse FFT. Cross correlation of two functions is equivalent to a complex conjugate multiplication of their Fourier transforms in the frequency domain. The use of FFT requires equal size IA in both images, and their dimensions should be a power of two.

The displacement of particles in the IA is estimated as the distance between the center of the IA and the peak value received from the 2D cross correlation function. The cross-correlation is applied on discrete values therefore, the peak correlation value permits the displacement to be determined with an uncertainty of ± 0.5 pixel. However, the peak is usually larger than one pixel; all pixel information of the peak can be used to calculate the peak position, and obtain sub-pixel accuracy using different methods. Gaussian and parabolic curve fitting work well and accurate on average size peaks (3 pixels) but are less reliable on smaller or larger peaks. Depending on the peak size and the method used, accuracies of less than one tenth of a pixel are possible. With displacements of 3 pixels or more, a confidence level of much higher than 95% can be achieved[45].

2.5.2 3D-Particle Tracking Velocimetry (3D-PTV)

Three-dimensional particle tracking velocimetry (3D-PTV) is a quantitative flow visualization technique, which measures the Lagrangian trajectories of individual particles in three-dimensional space [24, 10]. The measured trajectories can be used to compute velocity and acceleration. A standard 3D-PTV system includes: the experimental apparatus, data acquisition and storage and data processing.

The experimental apparatus includes the investigated fluid contained in a transparent cavity, particles, illumination facility and imaging device. If the experiment purpose is to investigate the behavior of the flow, the tracing particles must faithfully follow the movement of the fluid. Therefore as in the case of PIV, the tracers shall have low Stokes number of short time response time Eq. 2.23. The method is also suitable for the study of two-phase flows. The use of particles of different kinds can allow a simultaneous measurement of the velocity field and the paths of particles which do not follow the flow. Particles do not have to be necessarily solid, and can have positive or negative buoyancy [10]. Since the method is based on the coordinate measurements and tracking of individual particles, the number density, i.e. the number of particles per unit volume (p_N), is limited.

The area of interest in PTV is a 3D volume, therefore the light source should be with homogeneous intensity distribution over the entire observation volume to avoid data loss near the boundaries. Furthermore, it should be of high intensity to enable the use of small particles. If a pulsed light source is chosen, it should be pulsed synchronously with the cameras in frequency and in phase to reduce motion effects.

The choice of imaging device will affect the range of velocities that can be measured, since the time interval between the frames is prescribed by the imaging frequency. In turbulent flows the frame rate is defined such that the time step between two frames is about 1/10th of the Kolmgorov time scale. In principle, the use of two cameras in a stereoscopic arrangement is sufficient in order to determine the three coordinates of a particle in 3D space; a four camera arrangement can be considered ideal. It reduces the number of ambiguities almost to zero, allows a reliable determination of most of those particles that are hidden in one of the four cameras and it improves the accuracy of the coordinates of a point by a factor of 1.7. The arrangement of the cameras in respect to each other and to the area of interest will determine the depth of focus and the size of the observation volume. Wrong positioning of the cameras can cause dead-zones and therefore loss of data. If more than one camera is used, synchronization between the cameras is required [10]. The input of image sensor is digitized and transferred to a host computer for further processing.

Data processing The data processing chain from multi-camera digital image sequence to 3D particle trajectories includes three main steps: image processing (pre-processing), determination of particle 3D coordinates in a given time instance and tracking- correspondence between consecutive time images.

Pre-processing The first step of particle detection requires an image segmentation which can be simplified if the image are high-pass filtered. This high-pass filter is preformed by subtracting an unsharp mask from the original image and removes non-uniformities in the background intensity. Afterward, particle images can be segmented by a simple thresholding algorithm into bright areas-particles and dark regions-background. Blobs of bright light are detected and accepted as particle if their size and shape fulfill certain criteria. Particle coordinates are determined with subpixel accuracy using the gray value weighted center of gravity of the segmented blobs. However, under realistic PTV conditions, a problem of particles optically blocking or overlapping each other in one or more images can occur. One of the methods used for detection and splitting of overlapping particles images is a rule based modified thresholding operator, which searches for discontinuities in the gray value inside segmented particles and splits blobs if a discontinuity exceeding a certain empirically limit, is detected [23] .

Determination of particle 3D coordinates The fundamental mathematical theorem of photogrammetric 3D coordinate determination is described by the pinhole camera model and the collinearity condition, which state that object point, camera projection center and image point lie on a straight line. The mathematical formulation should be corrected to account for the effect of lens distortion and image digitization [23, 24]. Furthermore, the area of interest is usually contained in a transparent cavity made of glass. In this case, the rays scattered from the the particles to the sensor passes three optical media: water, glass and air, which cause a twice broken beam. The multimedia geometry model described in Dracos [10] can be used to correct this effect, if the X-Y plane of the coordinate system is chosen parallel to the plane of interface water/glass/air, as described in Fig. 2.3. Each object point P , that will experience the twice broken beam, can be shifted to an ideal point \bar{P} . The distance between the points can be calculated according to the Snell law if the refractive indexes and the thickness of the different medias are known. The collinearity condition can be applied to the ideal point \bar{P} .

In total each camera of a 3D-PTV system is described by 16 parameters: 6 for exterior orientation, 3 for interior, 5 for lens distortions and 2 for influences of A/D conversion. These parameters have to be determined in system calibration. In the calibration procedure, the multimedia model is being applied for a spatial resection using control points on the calibration target with known coordinates and introducing the 16 parameters as unknowns. After the calibration the same model can be used for a spatial intersection introducing the coordinates of a particle as unknowns [10].

Determination of particle 3D coordinates is based on establishment of spatial corre-

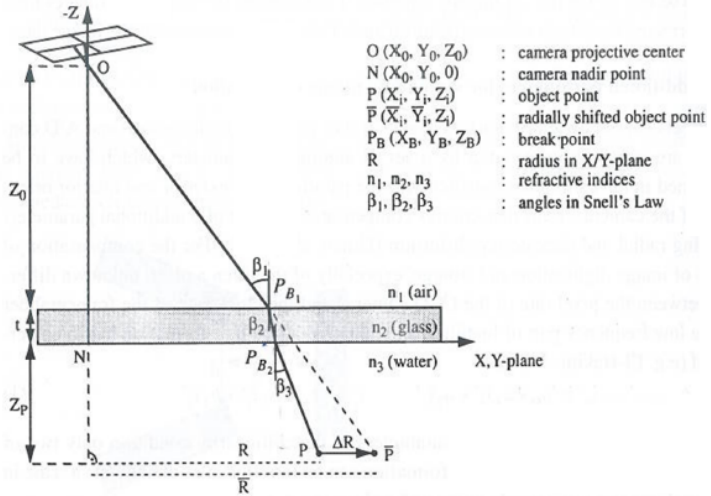


Figure 2.3: Radial shift for compensation of multimedia geometry

spondence between image frames. As the particle images do not show any characteristic feature like shape or color, which would allow a reliable distinction between them, the only criterion which can be applied is the geometric relation between the projection of the 3D particle on a pair of image planes, as described by the epipolar geometry. In figure 2.4, epipolar geometry of two image plane is presented, where O_L, O_R are the projection centers of the left and right cameras respectively, X is a particle and e_L, e_R are epipolar points- projection of the other camera center on the image plane. The points e_L, e_R are located on the base line connecting the two projection centers O_L, O_R . The point X_L is the projection of the particle X on the left image plane. The object location cannot be defined on the projected point alone, since all space object along the line $X - O_L$ will project to the same point in the image plane. Therefore, a second camera is necessary. The line $X - O_L$ is projected to an epipolar line $e_R - X_R$ in the image plane of the right camera. If the parameters of the two cameras are known, the search area on the right camera image plane is reduced to the epipolar line. If the image of the second camera contains only one particle along the epipolar line, the particle spatial location is defined. However, in real experiments, due to the effect of calibration accuracy and multimedia geometry, the epipolar line becomes a 2D band shaped window with tolerance width of ε . Ambiguities occur when multiple candidates are found in a search area defined by the epipolar line. The use of third or fourth camera allows the calculation of intersections of the epipolar line segments in image planes, which reduces the search area to the surrounding of a single point. After the establishment of multi image correspondences, the 3D coordinates of all successfully matched particles can be determined.

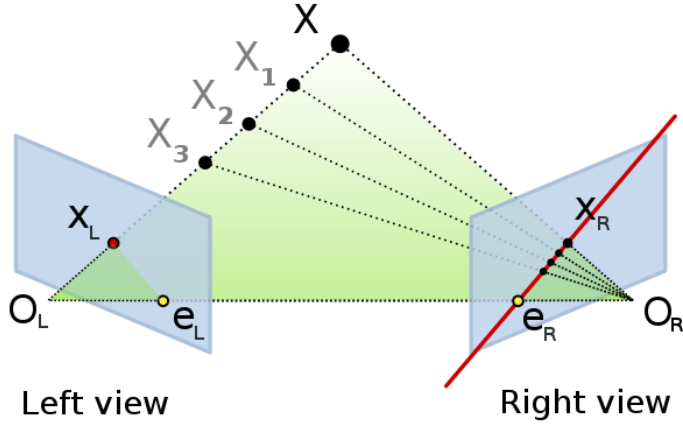


Figure 2.4: Epipolar geometry, two cameras view.

Tracking After the 3D-coordinates of individual particles are fully identified in each frame, the next step is to establish correct links between particle positions at consecutive time instances. The tracking procedure include two main stages: prediction of the expected position of the particle in the next frame and determining the real position of the particle with a selected statistical confidence inside a search volume centered on the expected position.

Reliable tracking procedure must have the capability of selecting the correct link between two successive positions of a particle in presence of a multiple choice of links. The procedure is influenced by many factors. The first one is the ratio of the average particle spacing, $\Delta_0 = p_N^{-1/3}$, to radius of the search volume r_i :

$$p = \frac{\Delta_0}{r_i} \quad (2.25)$$

The ratio is a measure of the tracking difficulty. For $p > 1$, the probability to find only one particle in the search volume is high and tracking is easy. For $p < 1$ more than one candidate is found and tracking becomes difficult, for $p \ll 1$ tracking becomes impossible. The second factor is the nature of the flow, e.g: non turbulent or turbulent flow, turbulent flow with high or low turbulent intensity. In turbulent flows the deviation of the particle real position from its expected position increases. An additional factor is data loss cause by drop-outs of particles coordinates in successive time steps. Drop-outs may result from dead zones caused by wrong positioning of the cameras, inhomogeneous illumination, overlapping of particles or failure to identify particles in photogrammetric process[10].

As a first step, the position of the particle in next frame is roughly estimated from

its position in the current and previous frames. Since the position of the particle in the current and previous frames and frame rate are known, the particle predicted position is determined by velocity evaluation, under the assumption that the particle moves during the time step and that acceleration can be neglected. If the current particle is itself linked to a particle in previous frame, the predicted position will be taken as the linear continuation of that link. If the particle does not have a link to previous frames but some particles in the search volume do, the predicted velocity of the particle will be calculated as the mean of these particles local velocity. If there are no links to previous frames for any of the particles (like when the tracking starts), velocity will be determined based on local flow properties [24].

The second stage is to link between the particle position in the current frame and its real position in the next frame. The estimation of the search volume is based on the nature of the flow. Once the search volume is defined, the number of particles inside the volume is determined. If no particle is found in it, a data loss has occurred. If only one particle is found, the link is established. If more than one particle is found ambiguities arise and application of sorting criteria such as minimum acceleration or minimum kinetic energy based on three or four framed is applied [10].

After the trajectories are established, the entire position signal $x_i(t)$ of each trajectory is low pass filtered and filtered velocity and acceleration signal $\widehat{u_i(t)}$ and $\widehat{a_i(t)}$ are derived as first and second deviates from $\widehat{x_i(t)}$. This filter reduces noise stemming from particle position inaccuracies. Detailed description on the process can be found in Lüthi et al. [21].

3 Methods and materials

To meet the objective of this study, resuspension events were investigated in an oscillating grid apparatus. This chapter will provide an overview of the experimental setup and data processing methods.

The experimental setup contained a grid chamber made of glass, square cross-section 30 X 30cm and 50cm tall mounted inside a metal frame 78 X 69cm and 102cm tall. Inside the chamber a flat and balanced grid oscillated vertically, driven by a 1.5kW variable speed electrical motor (CDF90L-4, KAIJIELI Inc.) and an eccentric. The frequency of oscillation of the grid is controlled by changing the input voltage to the motor. The grid was able to move with 1cm peak-to-peak amplitude and a frequency of up to 20Hz. The grid was made of square bars with a plastic sheet with 4X4 arrangement of circular holes pasted on it, in order to increase the grid solidity to 0.8. The resultant grid was consist of an outer frame of blocked area 0.5cm long and an 29 x 29cm inner part with circular holes with diameter of 4 cm; In each hole the grid bars intersect, creating 4 equal quarters as shown in Fig. 3.1(b).

Three different measurement technique were used: Manual analysis of digital video recordings - to define experimental conditions for the following PIV and 3D-PTV runs, PIV technique - to characterize the mean and turbulent flow under the oscillating grid and 3D-PTV to examine long duration data that synchronously measures local flow conditions and tracks the entrainment of individual test particles through the various phases of resuspension.

The flow field characterization (PIV measurements) was performed in a plane parallel to the grid's movements (x-y plane) 13cm from one side of the tank and 16.5cm from the other side on the z axis. 3D-PTV recordings of the resuspension events were performed in the center of the PIV plane, 11cm from one side of the tank and 11cm from the other side on the x axis as shown in Fig. 3.2. All three measurement technique were preformed for four different frequencies of the grid : 1.5, 1.7, 1.9 and 2.1Hz. For all the chosen frequencies, all tested particles became suspended. Experiments were made under the same

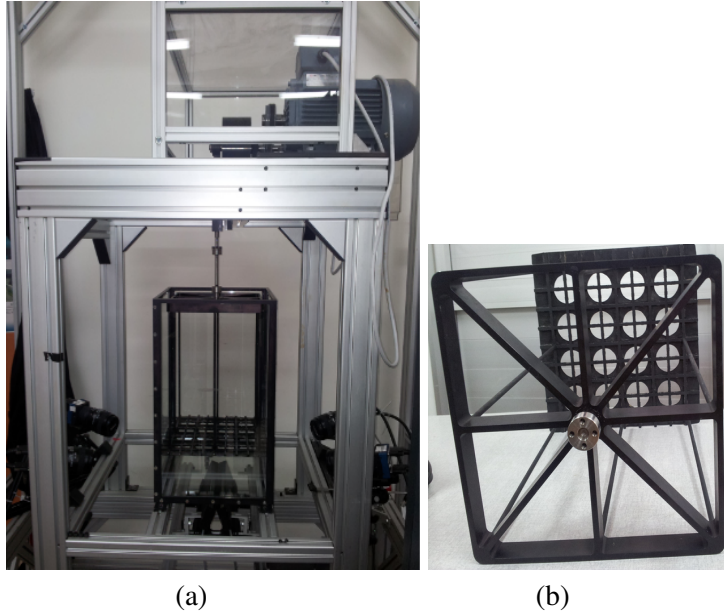


Figure 3.1: (a) Oscillating grid chamber apparatus (b) Oscillating grid, $f_{solid} = 0.8$

conditions: The grid chamber was filled with distilled water at a temperature of 22°C till a height of 22cm, grid height was set within the range of $h = 10 \div 11$ cm (measured from the bottom of the chamber) and stroke length $s_l = 10\text{mm}$. Test particles were distributed randomly on the bottom of the chamber. All runs started in still liquid and after a certain time of the grid oscillatory motion the test particles were entrained into the water column by the flow generated by the constantly oscillating grid.

3.1 Test particles

Silica gel (Fulka Inc.) particles with red coating and mean diameter of $\sim 550\mu\text{m}$ were used as test particles in this study. The spherical shape and size of the particles was verified under the microscope as shown in Fig. 3.3.

A preliminary settling test was applied to measure the settling (terminal) velocity of the particles and determine their effective density. Ten particles were chosen randomly and released one by one into a 500ml volumetric glass cylinder filled with distilled water. Particle release was made in the center of the cylinder (to minimize wall influence), and their settling was measured by a high speed CMOS camera (8 bit, 1280×1024 pixels, EoSens GE, Mikrotron) at 20 fps .

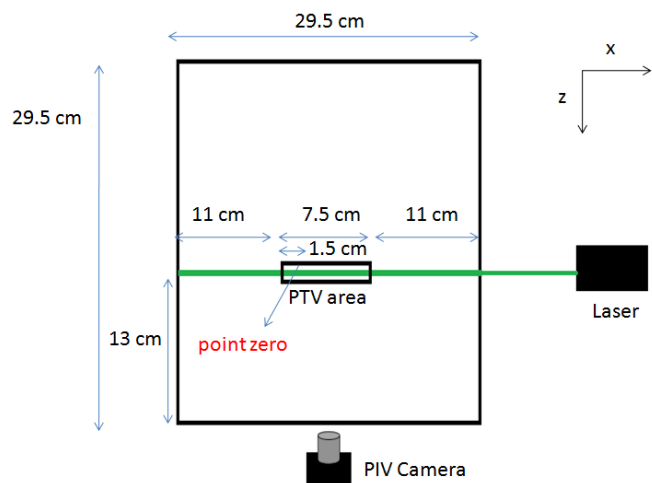


Figure 3.2: Flow field characterization (PIV) and 3D-PTV measurement areas



Figure 3.3: Electronic microscope image of a test particle

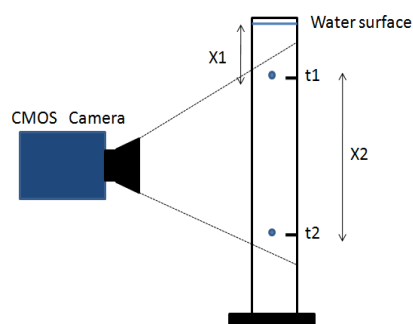


Figure 3.4: Settling velocity experiment setup. x_2 represents the measured settling distance, x_1 represents the distance between the water surface and the mark for the beginning of the measuring.

The beginning point of the measure was marked 50 mm beneath the water surface to ensure that the particle already reached constant velocity. Settling distance was determined as 95.8 ± 0.1 mm. Assuming that the particle settles vertically, the settling velocity was calculated according to Eq.3.1.

$$W_s = \frac{L_{lines}}{N_f} \cdot f_r \quad (3.1)$$

Where, L_{lines} is the settling distance (distance between marking lines), N_f is the number of frames , f_r is the frame per second rate , W_s is the settling velocity.

Applying the Stokes law, particle density was calculated according to Eq.3.2.

$$W_s = \frac{2r_p^2(\rho_p - \rho_l)g}{9\mu} \quad (3.2)$$

The effective density calculated for the test particles is: $\rho_p = 1062 \frac{Kg}{m^3}$. Their relaxation time was calculated according to Eq.3.3:

$$\tau_s = d_p^2 \frac{\rho_p}{18\mu} = 1.8 msec \quad (3.3)$$

For the sake of comparison with the existing resuspension models the Shields parameter was estimated using an analytical method given by Van Rijn [48]. The author showed the relation between the critical Shields parameter θ_{cr} and the particle parameter D^* . In this case the particle parameter is estimated as $D^* \approx 4.7$ and $\theta_{cr} \approx 0.052$. The critical bed shear velocity is therefore estimated as $u_{cr}^* \approx 0.004 m/s$ and the respective critical bed shear stress, is $\tau_c \approx 0.016 Pa$. According to the Shields diagram the selected particles-fluid combination corresponds to the transitional turbulent flow, i.e. range of $2 < Re_p < 500$.

3.2 Particle Image Velocimetry (PIV) method

3.2.1 Experimental setup

The PIV experimental setup included the seeding particles, illumination source, optical apparatus, high resolution camera, sampling and storage hardware and user interface software as illustrated in Fig. 3.5.

Dual head Nd:YAG laser (Solo 120XT; New Wave Research) was used as a light source, operating at 15Hz with energy of 120 mJ/pulse that produces a beam of light at wavelength of 532 nm. The light beam was spread into a thin light sheet using two lenses:

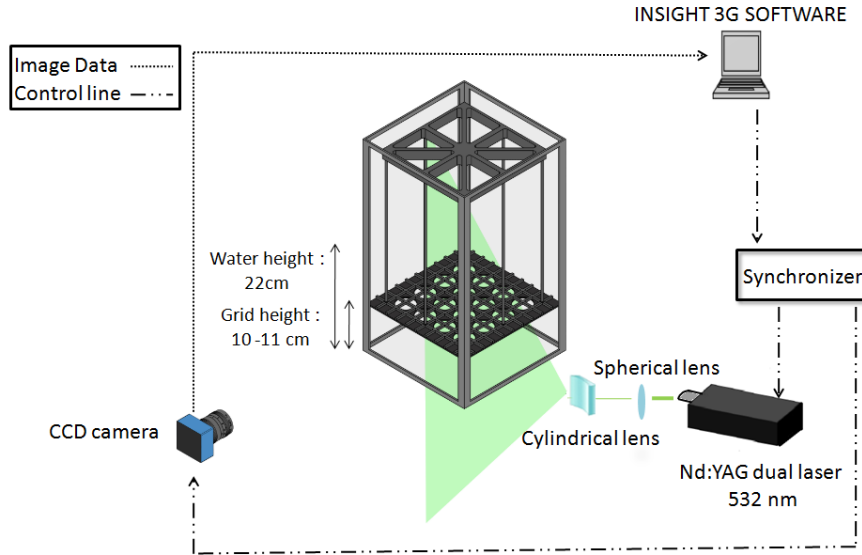


Figure 3.5: PIV Experimental setup scheme

(-15) mm cylindrical lens followed by a 500mm spherical lens located at the exit of the laser, creating a thin laser sheet with 2 mm thickness. Polystyrene particles with a nominal diameter of $10\mu m$ and a density of $1.05 g/cm^3$ (Duke Scientific Corp.) were used as seeding particles. To ensure the ability of the seeding particles to be used as reliable flow tracers, their relaxation time was calculated according to Eq. 3.3 as $5\mu sec$. The relaxation time is significantly smaller than the Kolmogorov time scale of the flow characterized by 0.07-0.1s, therefore the $St \ll 0.01$ and the particles behave as tracers. The scattered light from the particles was collected using a high resolution CCD camera (12 bit, 4008×2672 pixels, Power view 630062, TS Inc.) equipped with a 60mm macroscopic lens (Nikon 60), pixel dimension $15.07\mu m/pixel$. Images were captured beneath the grid from a height of 1.5cm from the bottom till the grid , size of the test area was 29.5cm X 8.9cm. The acquired images were transferred to a computer and the capturing process was controlled using a synchronizer (Laser Pulse TM610034; TSI) connected to a designated software (INSIGHT 3GTM, TSI) .

3.2.2 Time diagram in PIV

The synchronizer controlled the operation of the camera, frame grabber and laser using a series of TTL sequences. The camera was operated in straddle mode, therefore in each synchronize cycle two frames were acquired. Laser pulse delay is the time interval between the beginning of the synchronize pulse sequence and the first laser pulse. PIV

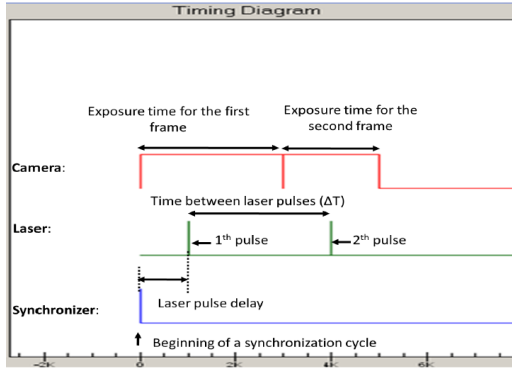


Figure 3.6: PIV timing parameters diagram

exposure is the exposure interval of the first frame. The Laser pulse separation time Δt is the time interval between the laser pulses. This parameter is chosen according to the estimated maximal velocity of the particles and the size of the interrogation window; the maximal pixel displacement, $\Delta s = \Delta t \cdot u_{max}$, should not exceed a 1/4 of the interrogation window size. Final definition of the actual values was the result of a trial and error process, i.e. changing the parameter values until a clear image is achieved in both frames, and the quality of the velocity vectors is satisfying. The time parameters of the PIV experiments are shown in Fig.3.6. The final value of Δt was set to 3.5-7ms, depending on the frequency of the grid and the flow velocity. Time between couple of exposures was set by the camera frequency (2 Hz). For each frequency of the grid, 500 pairs of images were captured.

3.2.3 Post processing

Image processing was performed using INSIGHT 3GTM software as follows. Each pair of images was divided into interrogation windows of 32×32 pixels. For each interrogation window, FFT based cross correlation algorithm with 50% overlap and Gaussian peak fitting was used to detect the displacement vector of the particle volume between the two frames. The vector field was calculated by dividing the displacement field with the known time interval between the laser pulses. In order to remove wrong displacement vectors, two post processing filters were applied. The first filter was applied twice, once for removing the wrong velocity vectors that exceeds a threshold value and second for removing velocity vectors that exceeds the standard deviation of the velocity vectors within each map. The second filter removed wrong vectors based on differences between individual vectors and their neighbors, using a median test.

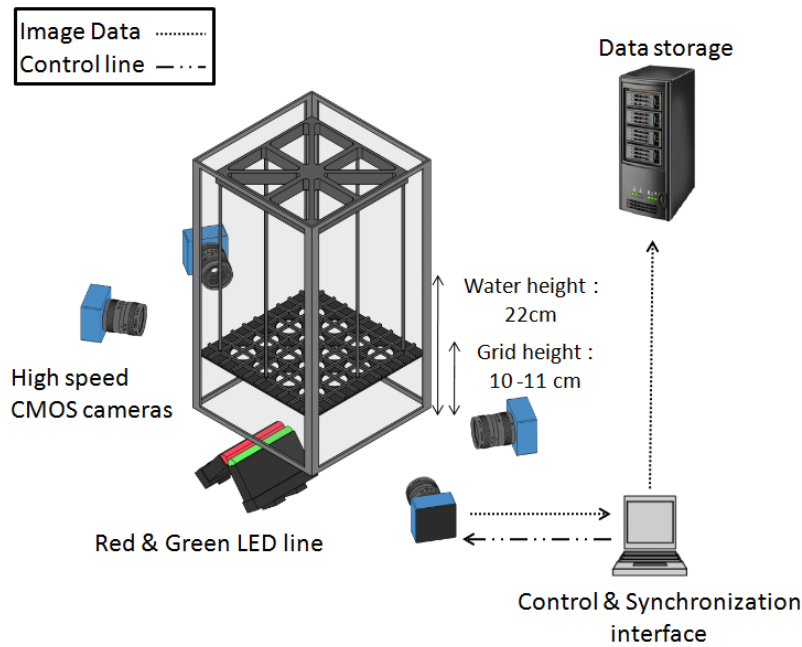


Figure 3.7: 3D-PTV Experimental setup scheme

The instantaneous velocity vector fields received were in pixel units, to receive the velocity in SI units the velocity values had to be multiplied by the pixel to mm ratio. The field of view in every image was 29.5cm X 8.9cm. Therefore, the number of pixels was divided by the length of the grid chamber in order to calculate the calibration ratio of 8.98pixel/mm . The resultant velocity maps were exported to Matlab post-processing software (www.openpiv.net) for further analysis of flow parameters: Reynolds stresses, mean and fluctuating velocity components.

3.3 3D-PTV method

3.3.1 Experimental setup

The 3D-PTV experimental system included the following components, as described in Fig.3.7.

The digital video recording system is based on the technology and software of IO Industries (Canada) that consists of four high speed CMOS cameras (8 bit, 1280×1024 pixels, EoSens GE, Mikrotron), a 60mm lens (Nikon) used for image acquisition and a control and data recording software tool, Streams 5TM. The cameras simultaneously captured (maximum possible time jitter of 0.001fps) and stored the digital video at maximum

rate of 700 Mb/sec using a digital video recording system that consists of 48 hard drives and four Camera Link Full frame grabbers (CLFC, IOI). The system is installed with the 3D-PTV open source software (www.openptv.net). Cameras were located in an angular array from two sides of the grid chamber, as shown in Fig.3.7. Four cameras arrangement reduces the number of ambiguities and allows reliable determination of most the particles which are completely hidden in one of four images [10]. Image acquisition rate was set to 160fps. The observation volume was 7.5cm long, 4cm depth and 6cm height. Two light emitting diodes (LED) line sources (MB– LL306–R–24; Metaphase, USA), green (530nm) and red (630nm), illuminated the observation volume of interest in the center of the grid chamber. The two LEDs were located 1cm below the glass chamber, facing each other in an angle : their upper part touching, and the bottom remote, as described in Fig.3.7. The combination of the two LED light sources and their locations provided a nearly uniform light intensity across a wider observation volume.

The fluid was seeded with poly amide particles with mean diameter of $50\mu m$ and density of $1.03 g/cm^3$ (Dantec Dynamics Inc.). To ensure the ability of the seeding particles to be used as reliable flow tracers, their relaxation time was calculated according to Eq.3.3, and is equal to $0.143 msec$, significantly smaller than the Kolmogorov time scale of the flow characterized by 0.07-0.1s, therefore the $St \ll 0.01$. Furthermore, the particles fulfill the conservative restrictions shown in Dracos [10] (neutrally buoyant, $d_p < 60\mu m$) for flows with acceleration of $|a| < 10m/s^2$, and therefore behave as tracers. The test solid particles (Silica gel particles with red coating) were randomly distributed on the bottom of the grid chamber.

3.3.2 Calibration

In 3D-PTV method, pixel position of the particles in four image planes are translated into 3D physical coordinates (x, y, z) based on the calibration of the imaging system. An accurate calibration of the system (definition of 16 parameters for each camera: camera exterior and interior orientations, lens distortion and further disturbances) is important in order to get the exact complex geometric modeling which is affected by three optical media with different refractive indicates. Two step calibration method was used in the experiment:

- Static calibration.
- Dynamic or so-called “dumbbell” calibration.

3.3.2.1 Static calibration

The basic calibration process includes a 3D reference body with known points that is placed inside the observation volume and imaged once by all four cameras. Given the spatial coordinates of the target points and the measured image coordinates of these points, the co-linear perspective projection model described (in chapter 2) can be applied to determine the 16 parameters describing each camera. The target points should cover the entire observation volume; the distance between the points will determine the accuracy of the measurement [10].

A calibration target ($60 \times 60 \times 60$ mm) made of a non reflective black metal alloy with 20 holes located at fixed distances (target points), was used to calibrate the system. The reference body was placed at the bottom of the grid chamber, in the center of the PIV plane, 12.5cm from one side of the tank (0.5cm from the beginning of the PTV area) and 11cm from the other side on the x axis. Distance between the target points was 1cm, one of the lowest target point (located 2cm from the bottom of the grid chamber) was defined as the axis origin of the system, i.e., measured particle coordinates refer to that point as origin. The $x - y$ plane was chosen parallel to the reference body and the z axis was chosen parallel to the bottom of the chamber, as described in Fig.3.2.

For each camera, a calibration file containing the following data should be defined: spatial location and rotation angles of the camera relative to the origin point of the calibration body, camera focal point, refractive indexes of the three optical medias: air, solid and liquid, thickness of the solid optical media (glass tank wall in this case) and the distance from the solid media to the calibration body, i.e. thickness of the liquid media. The calibration file serves as an initial guess for the software algorithm which performs an iterative process to solve the multi geometry projection model. The final solution is sufficient to solve the calibration problem approximately.

3.3.2.2 Dynamic calibration

In the current experimental setup, the standard calibration body could not be placed underneath the grid. After the stationary calibration stage, the calibration body was removed and the grid was installed inside the chamber. The process could have caused minor changes in the chamber position which could affect the calibration. Furthermore, the lowest target points on the reference body were located 2 cm from the bottom of the chamber, leaving the important area near the bottom, where the resuspension events occur, without sufficient calibration. Therefore, a further calibration was required.

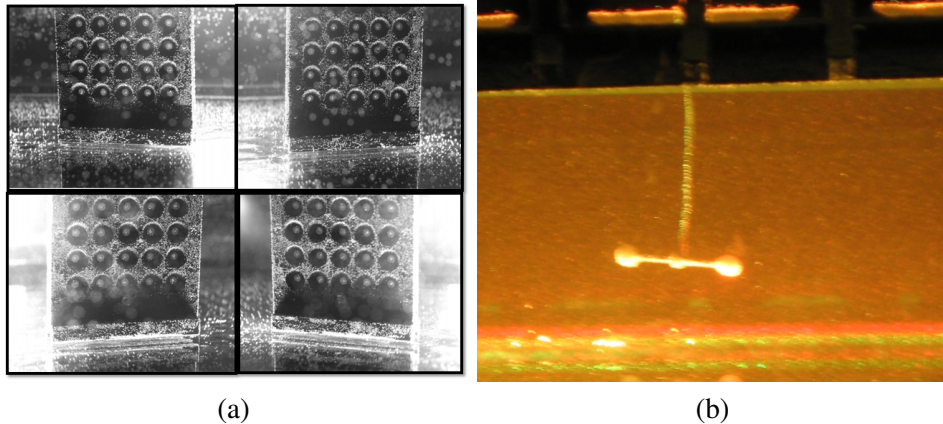


Figure 3.8: The two calibration methods : (a) Static calibration body as was captured at the same time by the four CMOS cameras (b) Dynamic calibration using a dumbbell, seen in the frame of one of the cameras during the calibration recording.

In a dynamic calibration, a dumbbell shaped target (see Fig.3.8b) comprised of two bright points with a known diameter (5 mm in our case) and a fixed distance (23 mm) is placed inside the measurement volume. The target is imaged by all four cameras as it moves inside the observation volume and provides a 3D domain. The initial guess for the camera parameters was taken from the stationary calibration. The target was moved inside the observation volume, 600 images were taken from each camera with the dumbbell in different positions within the field of view. For each camera frame, the center points of the two spherical bodies were identified and a target file containing the coordinates of their position was written for each image using custom-made code (www.openptv.net) and was used as reference for the image plane coordinates. Solving the projection model using the multiple image coordinate data in an iterative process improved the calibration to the necessary level of accuracy.

3.3.3 3D- PTV post processing

Initial post processing of 3D-PTV data, including particle identification and tracking, was preformed separately for the test particles and tracers in Streams 5, and resulted in Lagrangian trajectories of test and tracer particles. Only trajectories that were traceable for more than 5 frames were considered for analysis. Further data processing was preformed on Matlab[®] (www.openptv.net).

4 Results

This chapter presents the results obtained from the experimental setup as described in Chapter 3. Section 4.1 presents the settling test results, section 4.2 presents the visualization results of the resuspension events, section 4.3 presents the flow field characterization for the investigated area and section 4.3 is devoted to the Lagrangian results obtained from the 3D-PTV analysis.

4.1 Settling test results

Preliminary settling test was conducted in order to determine the settling (terminal) velocity of the test particles and their effective density, as described in section 3.1. Ten test particles were randomly chosen for the experiment; Table 4.1 and Fig.4.1 presents their diameter and calculated settling velocity respectively.

The average settling velocity was 10.79 mm/s . Particles effective density was calculated according to Eq.3.2, and was determined as $\rho_p = 1062 \text{ kg/m}^3$.

4.2 Visualization results

Re-suspension events were recorded using 3D-PTV system and manually analyzed. For the conditions of these experiments, particles resuspension occurred in different modes: sometimes rolling and/or sliding followed by lift-off and some particles were lift-off immediately. It is noteworthy that detachment of the particle from the bottom surface was

Particle	1	2	3	4	5	6	7	8	9	10
$d_p [\mu\text{m}]$	542.37	556.87	562.46	545.54	553.74	541.69	557.02	546.22	541.09	560.57

Table 4.1: Diameters of 10 test particles that were used in the settling test.

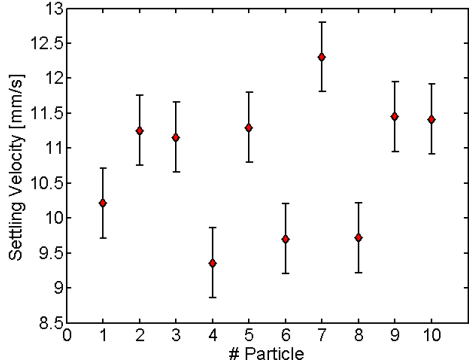


Figure 4.1: Settling velocity of test particles.

not necessarily followed by reentrainment, some particles were deposited almost immediately. There are also particles that remained adherent to the bottom after rolling or sliding. Particles motion during resuspension was divided into two main events; Initial movement (detachment) - beginning of particle movement on the bottom surface from a stationary position to either rolling or sliding, and lift off - beginning of particle movement upwards from the bottom surface. Before the initial movement, adhesion and contact forces are the major forces that prevents particles from resuspension. After detachment, particle contact time with the surface is limited, therefore adhesion and contact forces decreases and their effect on the lift-off event is reduced. Therefore, the next sections will focus on the second event (moment of lift off), which enables to neglect the adhesion force and investigate the influence of flow characteristics on its occurrence.

In this section, resuspension is described as a fraction of lift-off particles, the so-called “pick-up rate”, defined as:

$$n(t) = 1 - \frac{n(t)}{n(0)} \quad (4.1)$$

where $n(t)$ is the number of particles on the surface at time t_i . Practically in each video frame the number of particles was counted manually and the ratio was estimated using recordings of different cameras. Four experiments were preformed for every frequency, time of the examination: from the beginning of the grid oscillation till the end of the experiment, was kept constant - 1 min. Fig.4.2 presents the first time instant t_i at which the resuspension initiated, i.e $n(t_i) < 1$, and Fig.4.2 presents the result at large times, i.e. $n(t \rightarrow \infty)$ versus the frequency of grid (f). There are clear trends in the results: the oscillating frequency of the grid initiates the lift-off events at shorter times and the total

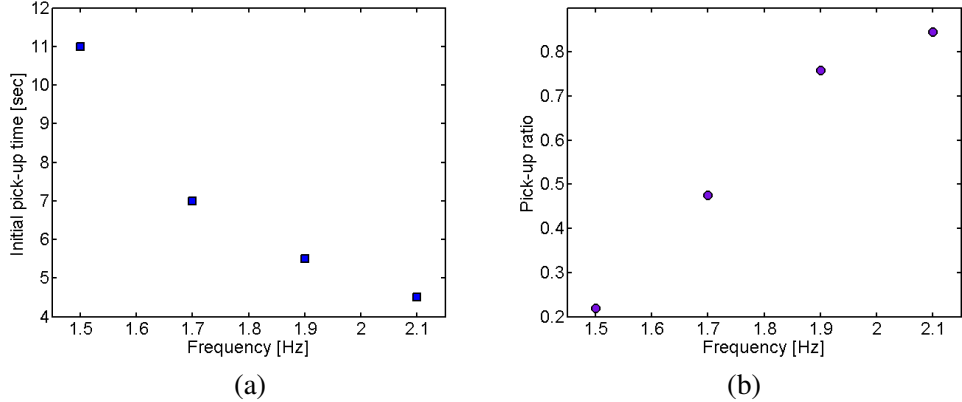


Figure 4.2: (a) Initial pick-up time [sec] (b) Pick-up ratio: number of picked-up particles divided by the total number of particles in the field of view.

number of lift-offs increases with increasing frequency. However, increase in pick-up ratio and decrease in initial pick-up time are not linear; the difference between values of two consecutive frequencies decreases as the frequency increases i.e, the largest differences are shown between 1.5Hz to 1.7Hz and the smallest between 1.9Hz to 2.1Hz. Analysis in the next section will focus on disclosing the reasons for these trends.

4.3 Flow field characterization

Detailed measurements and quantification of flow characteristics under the oscillating grid were preformed to characterize the relationship between mean flow, turbulence, and lift-off events. Fig. 4.3 shows instantaneous velocity contour maps of the two velocity components $u(x,y)$ and $v(x,y)$ for frequency of 2.1Hz. $u(x,y)$ represents the horizontal velocity component (perpendicular to the grid's movement) and $v(x,y)$ represents the vertical velocity component (parallel to the grid's movement). x and y axis are normalized to the width of the grid chamber, L . The zero point matches the zero point chosen for the Lagrangian trajectories (PTV experiments) as shown in Fig.3.2 on the bottom of the chamber. Both instantaneous fields indicate on a non uniform flow that was generated by the grid's movement. In both velocity components a rapid and constant changes in the direction and magnitude of the flow along the chamber cross-section is seen, indicating on a turbulent flow. The magnitude of the instantaneous velocities and the constant changes decreases as the distance from the grid (top of the contour maps) increases (on the y axis). This trend is more noticeable for the vertical velocity component $v(x,y)$. At the top, near the grid the $v(x,y)$ absolute values are 50-150mm/s and it decreases to 30-70mm/s near the

bottom of the grid's chamber. The same behavior was observed in the instantaneous velocity maps of all 4 different frequencies. The range of the PTV measurements is between -0.05 to 0.13 on the x axis, and 0 to 0.2 on the y axis (60mm height). Mean and turbulent flow properties were calculated 20mm from the bottom (0.07 on the y axis, marked as red line in Fig.4.3).

4.3.1 Mean flow

The average velocities were calculated from the instantaneous velocity vector fields for each frequency according to Eq.4.2:

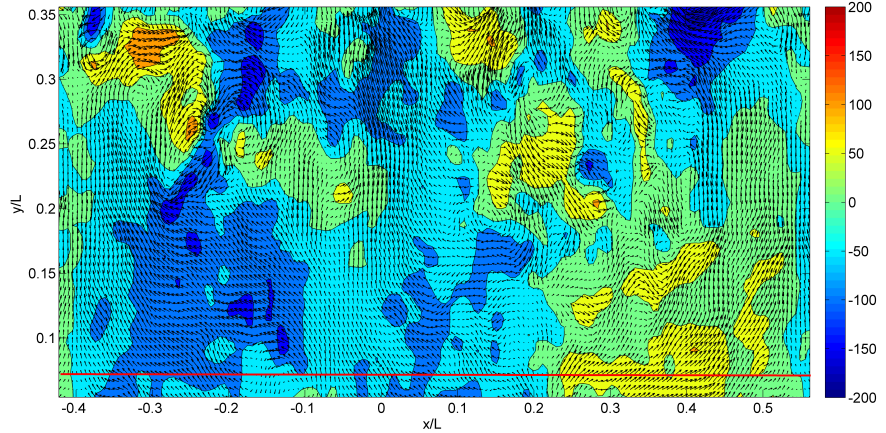
$$U = \frac{1}{N} \sum_{i=1}^N u \quad (4.2)$$

N is the total amount of velocity vector fields ($N = 500$ in the present study) and u is an instantaneous velocity vector field. Velocity magnitude is calculated according to Eq.4.3 :

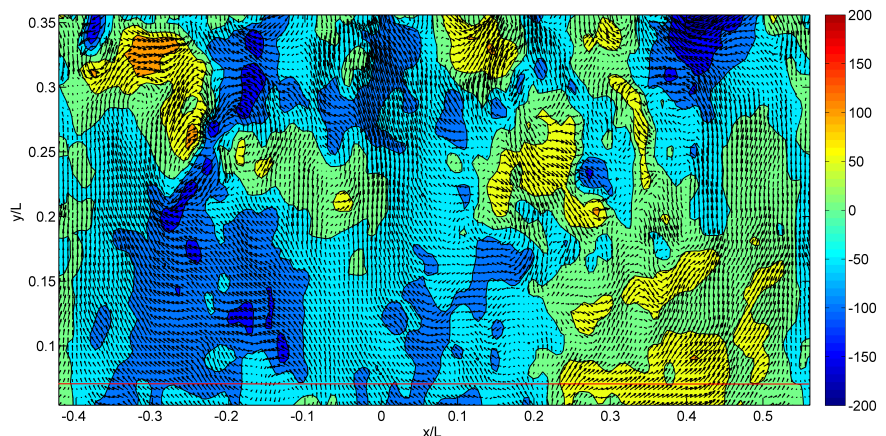
$$U_{mag} = \sqrt{U^2 + V^2} \quad (4.3)$$

The mean flow properties are shown in Fig.4.4 as a function of x axis normalized to the width of the chamber. At the top of each figure a sketch of the grid's cross-section was drawn; black mark represents a blocked area (bar), white represents an open area (hole) in the grid. Fig.4.4(a) and 4.4(b) present the mean horizontal and vertical velocity components respectively. Horizontal mean velocity (U) increases and decreases alternately along the x axis, respectively to the mesh size: High absolute values are obtained beneath the holes while underneath the bars, between the holes, the values transform from positive to negative. Near the walls of the chamber the mean horizontal velocity is approximately zero. Likewise, mean vertical velocity also increases and decreases alternately along the x axis: increases are shown under the holes and decreases of 10-15 mm/s under the large bars (which separates between the four holes in the grid). Beneath the small bars (which intersect each hole), flow direction reverses and the flow is being pushed downward (towards the bottom of the grid's chamber). Maximal values of V , are obtained approximately at the center of the chamber ($x/L = 0.04$ and $x/L = 0.11$). Near the walls, mean vertical velocity is negative and the fluid is moving towards the bottom of the chamber .

An appreciable existence of mean flow is shown, indicating on the existence of large-scale secondary flow cells in the tank. The received mean velocity profiles reinforce the argument that the flow generated by the oscillating grid creates a recurring flow pattern proportional to the mesh size. The recurring flow regime is similar to a vortex ring form:



(a)



(b)

Figure 4.3: Instantaneous velocity fields for frequency of $2.1 Hz$, x and y axis are normalized by the width of the grid's chamber, L . (a) Contours of horizontal velocity component $u(x,y)$. (b) Contours of vertical velocity component $v(x,y)$.

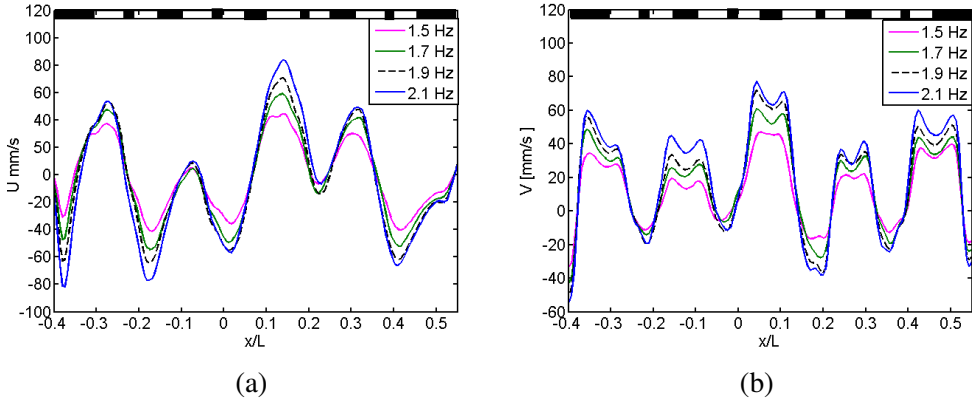


Figure 4.4: Mean flow profiles as a function of x axis normalized to the width of the grid's chamber :(a) Mean horizontal velocity component [mm/s] (perpendicular to the grid's movement U). (b) Mean vertical velocity component [mm/s] (parallel to the grid's movement V).

beneath the grid, the liquid is pushed away (downwards) from the grid and to both opposing sides of the chamber, while it is pulled towards the grid at the open areas (holes around the bars) creating unsteady swirling flows near the bottom of the chamber.

The mean velocity profiles show the same trend for all frequencies, but the range of their values increase with increasing the frequency. For example: the horizontal velocity values for 1.5Hz range between -40 to 40mm/s while for 2.1Hz it ranges between -80 to 80mm/s, an increase of 200% between the lowest and the highest frequency. In addition, the difference between two consecutive frequencies decreases with increasing the frequency. As was shown in Fig.4.2, the number of lift-off events also increases with frequency in a similar trend. Therefore, by only observing the mean velocity profiles throughout the whole length of the grid chamber (x axis), it can be assumed that the entrainment of particles into suspension (under the oscillating grid), is at least to some extent, related to mean velocities.

In order to link directly individual particle lift-off with mean and turbulent flow characteristics, a distribution of lift-off events locations on the $x-z$ plane was preformed (as shown in Fig.4.15), by using the Lagrangian trajectories of the particles (PTV results). Fig.4.5(a) and 4.5(b) present a coordination between the locations of the lift-off events and the mean horizontal and vertical velocity components respectively; red mark represents the area where most lift-off events occurred, yellow - few events occurred and black - none of the events occurred. In order to verify the possibility that the lift-off events are related not only to turbulent but also to the mean velocity, different values of the mean

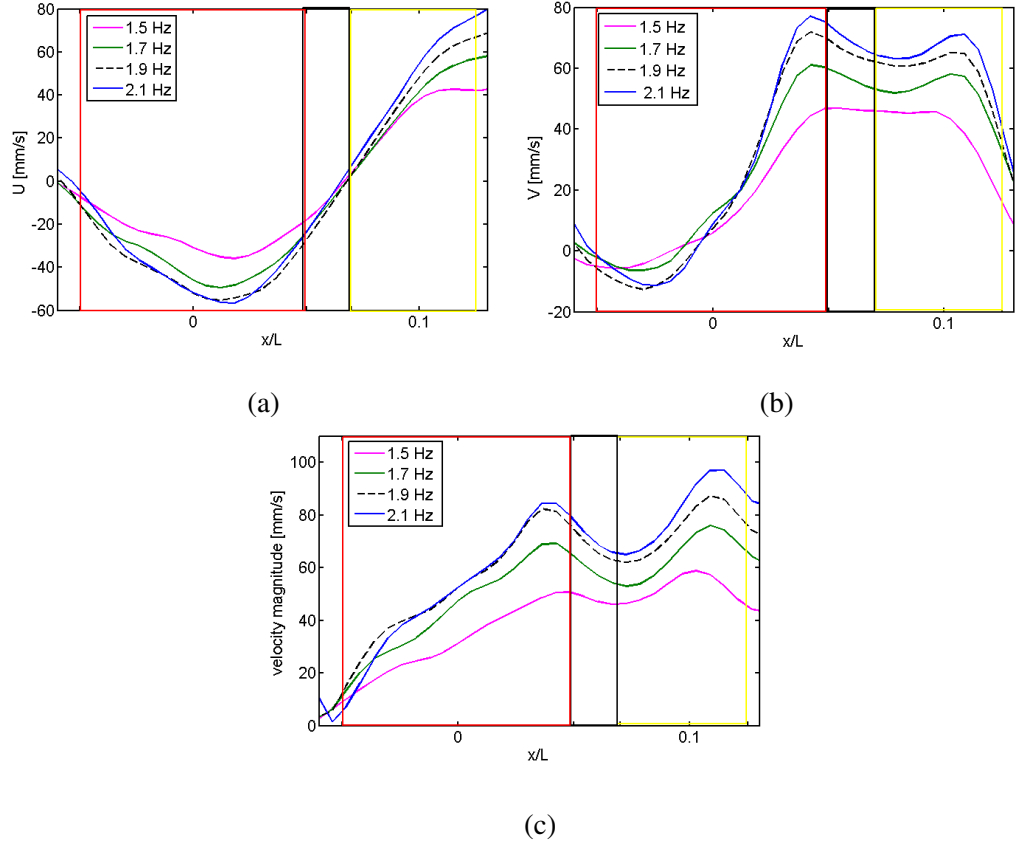


Figure 4.5: Coordination between the locations of lift-off events and mean flow properties: (a) Mean horizontal velocity component [mm/s] (b) Mean vertical velocity component [mm/s] (c) Mean velocity magnitude [mm/s]. Red mark - area where most lift-off events occurred, yellow - few events occurred and black - none of the events occurred.

velocities between areas where lift-off events occurred and areas where none of the events occurred, were expected. As shown in Fig.4.5(a) the absolute value of the horizontal velocity component (U) is high where lift-off events occurred and approximately zero where none of the events occurred, which indicate on a good correlation. However, the values of the vertical velocity component (V) and velocity magnitude are high for both areas and therefore less correlated with lift-off. Therefore, lift-off events could be associated with high absolute value of the mean horizontal velocity (U) but not with the mean vertical velocity (V) or mean velocity magnitude.

4.3.2 Turbulent flow properties

Velocity fluctuations were defined according to Eq.4.4, where u is the instantaneous velocity and U is the mean velocity. Turbulent properties were calculated according to Eq.4.5 and Eq.4.6 respectively; the root mean square (r.m.s.) of the fluctuating velocity components and the Reynolds stress. The r.m.s. values and the Reynolds stress indicate on the amount of turbulence in the grid chamber.

$$u' = u - U \quad (4.4)$$

$$u_{rms} = \sqrt{\overline{u'^2}} \quad (4.5)$$

$$\tau_T = -\rho \overline{u'v'} \quad (4.6)$$

Fig.4.6(a) and Fig.4.6(b) present the r.m.s. profiles for the horizontal, u_{rms} , and vertical, v_{rms} , velocities respectively. In Both u_{rms} and v_{rms} profiles a recurring flow pattern proportional to the mesh size is observed: Beneath the holes, the v_{rms} and u_{rms} values increase and then decrease 5-10mm/s, beneath the large bars (separating the four holes in the grid), beneath the small bars (which cross each hole) r.m.s. values decrease 10-15mm/s more. The ratio of vertical r.m.s to the horizontal r.m.s., $\frac{v_{rms}}{u_{rms}}$, is higher than 1.4, indicating on an anisotropic structure of the grid generated turbulence. Reynolds stress profiles are presented in Fig.4.6(c). Along most of the x axis the Reynolds stress absolute value constantly fluctuates between 0 to 0.6Pa for frequencies of 1.5 and 1.7Hz and between 0 to 1.1Pa for frequencies of 1.9 and 2.1Hz, which indicate that the flow is characterized with various levels of turbulence. At $x/L = 0.02$, approximately at the center of the grid's chamber, the Reynolds stress value exceeds to 1Pa for 1.5Hz and between 1.8 to 2.5Pa for the other frequencies, an increase of 200 - 250%, indicating on high level of turbulence in the center of the examined area.

Turbulent flow profiles show the same trend for all frequencies, but the range of their values increase with increasing the frequency. For the horizontal fluctuations u_{rms} and the Reynolds stress profiles the difference between two consecutive frequencies decreases with increasing the frequency, similar to the trend observed for the pick-up ratio in Fig.4.2. However, this trend is not shown for the vertical fluctuations v_{rms} , i.e: difference between two consecutive frequencies is constant. Therefore, a small increase in the amplitude of horizontal turbulent fluctuations can significantly increase the amount of lift-off events,

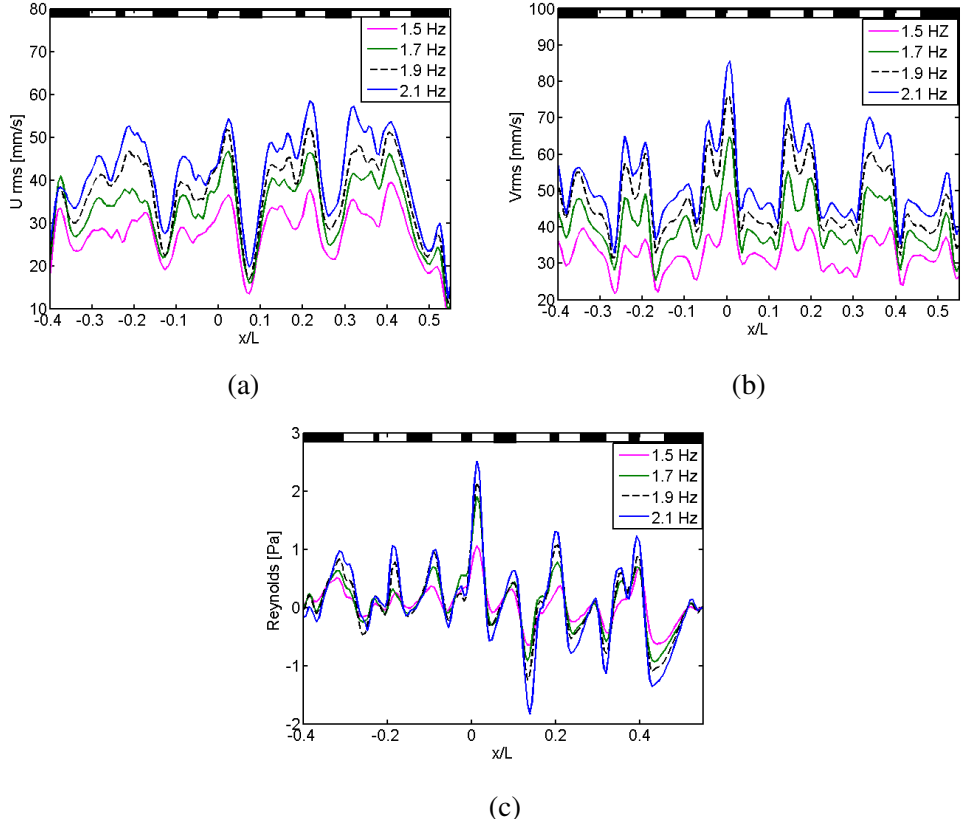


Figure 4.6: Fluctuating flow properties as a function of x axis normalized to the width of the grid's chamber. (a) u_{rms} of the fluctuating velocity [mm/s] (b) v_{rms} of the fluctuating velocity [mm/s] (c) Reynolds [Pa].

but the vertical fluctuations (v_{rms}) are less correlated with the lift-offs.

Fig.4.7(a) ,4.7(b) and 4.7(c) present a coordination between the locations of lift-off events and turbulent properties: u_{rms} , v_{rms} and Reynolds stress respectively; red mark represents the area where most detachment events occurred, yellow - few events occurred and black - none of the events occurred. u_{rms} values increase where lift-off events occur and decrease where none of the events occur. Weak correlation is shown for v_{rms} ; Lift-offs occur at both high and low v_{rms} values. Significant differences in Reynolds stress values between different areas are observed, lift-offs occur concomitantly to higher Reynolds stress: Most lift offs occur where Reynolds stress values are between 1-2.5 Pa, none of the events occur where the values are approximately 0 and few events occur where the values are 0.4-0.8 Pa.

Turbulent intensity was calculated according to Eq.4.7.

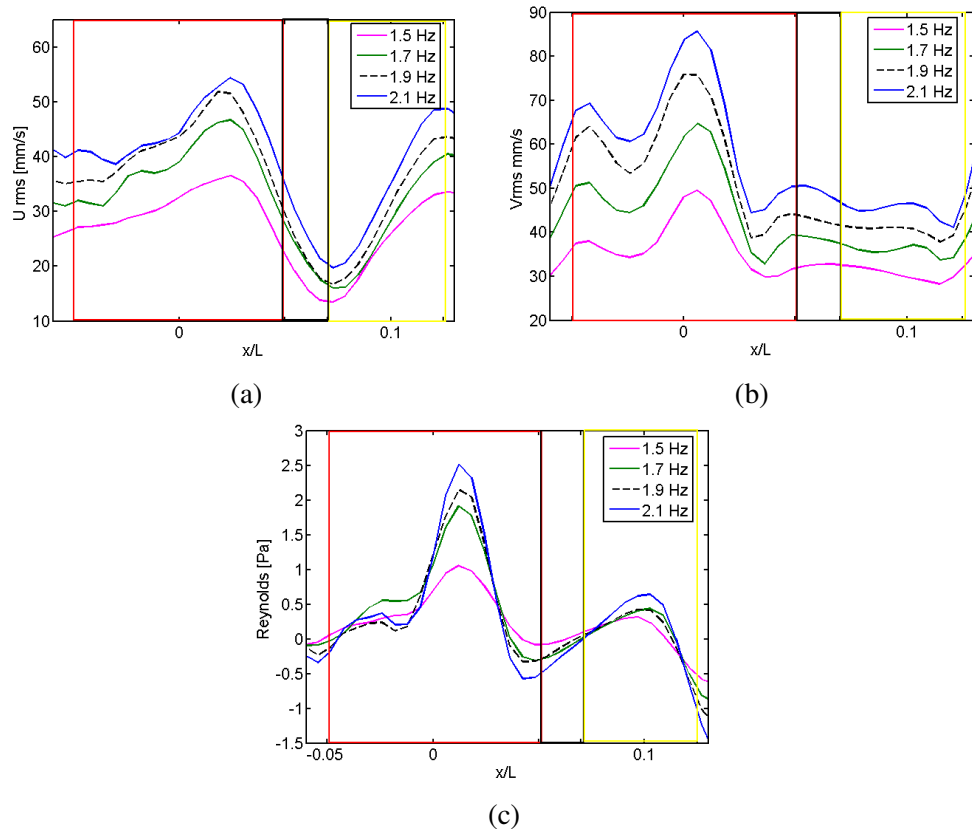


Figure 4.7: Coordination between the locations of the lift-off events and fluctuating flow properties. (a) u_{rms} [mm/s] (b) v_{rms} [mm/s] (c) Reynolds [Pa]. Red mark - area where most lift-off events occurred, yellow - few events occurred and black - none of the events occurred.

f [Hz]	I_u	I_v
1.5	1.4	1.8
1.7	1.5	2.0
1.9	1.5	2.1
2.1	1.5	2.2

Table 4.2: Horizontal and vertical turbulent intensity of the four frequencies.

f [Hz]	u_{rms} [mm/s]	v_{rms} [mm/s]
1.5	0.88	0.95
1.7	1.00	1.08
1.9	1.11	1.21
2.1	1.24	1.34

Table 4.3: Expected r.m.s. velocity fluctuations according to Hopfinger and Toly [18] empirical relationship .

$$I = \frac{u_{rms}}{U} \quad (4.7)$$

Table 4.2 presents the average horizontal (I_u) and vertical (I_v) turbulent intensities calculated in the locations of the lift-off events (i.e : between -0.05 to 0.13 on the x axis) for the four different frequencies. Although appreciable existence of mean flow was observed, both horizontal and vertical turbulent intensities are higher than 1.4. Therefore the fluctuations are always dominant compared to the mean components indicating on a high level of turbulence. Vertical turbulent intensity increases with frequency while horizontal turbulent intensity only increases between the 1.5Hz and 1.7Hz and then remains constant. Therefore, the ratio between vertical to horizontal turbulent intensities increases with frequency creating different types of turbulent flows for each frequency.

The expected r.m.s of velocity fluctuations can be estimated according to Hopfinger and Toly [18] empirical relationship for grids (Eq.4.8).

$$u_{rms} = C_1 M^{0.5} s_l^{1.5} f z^{-1}, v_{rms} = C_2 M^{0.5} s_l^{1.5} f z^{-1} \quad (4.8)$$

For the current experiments, parameters were estimated as $z = 8.5\text{cm}$, $M = 4\text{cm}$ (diameter of grid's circular holes) and $C_1, C_2 - 0.25$ and 0.27 receptively (according to Hopfinger and Toly [18] reported values). Table 4.3 summarizes the results.

As shown in Fig. 4.6, empirical u_{rms} and v_{rms} are almost one order of magnitude higher than the expected values according to Eq.4.8. Although, the measurements were

performed at distance of 8.5cm from the grid, which is greater than required for the operating conditions (i.e. $:z > 2M = 8\text{cm}$), the grid structure used in the experiments did not follow the design restrictions: grid solidity was higher than 40%, it was based on a circular holes arrangement with large opaque regions and its ending, close to the wall, did not follow the reflection-symmetry condition. Mean secondary circulation and stronger jets were formed. Therefore, turbulence generated behind the grid was not isotropic nor homogeneous. In this case, the spatial decay of turbulence is irregular and may not follow Eq.4.8.

4.3.2.1 Length and time scales

This part presents a set of calculations preformed in order to evaluate several lengths, time and other scales which describes the turbulent flow. In order to discuss the various scales of the flow in the following analysis, a definition of the scales and the range of scales is required: large (energy containing range), inertial and Kolmogorov (i.e dissipation scale).

Integral length scale: considered as the largest scale of the system in turbulent flow (excluding the external scale of the system: geometric scale, which is larger than this length). A convenient measure of this scale is as follow:

$$L_{ij} = \frac{1}{R_{ij}(0)} \int R_{ij}(r) dr \quad (4.9)$$

where i and j are velocity components and r defines the vector along (x,y). $R_{11}(R_{uu}(x))$ and $R_{vv}(y))$ is the Longitudinal correlation function of velocity components. . On the same manner $R_{22}(R_{uu}(y))$ and $R_{vv}(x))$ is the transverse correlation function. Scales larger than integral scales are characterized by L , the width of the flow or the size of the largest eddy. In order to obtain the integral scales of the flow an analysis based on the velocity correlation function defined below was applied.

$$R_{ij}(r) = \overline{u'_i(x+r)u'_j(x)} \quad (4.10)$$

Velocity correlation functions were calculated 20mm from the bottom throughout the whole length of the grid's chamber (at the same line mean and turbulent flow properties were calculated). Fig.4.8 presents the longitudinal correlation function applied for the fluctuating velocity for all frequencies. As shown, the correlation function fluctuates around zero and does not show compatibility with the theoretical shape of the velocity correlation function [36]. In addition, the assumptions of homogeneous and isotropic

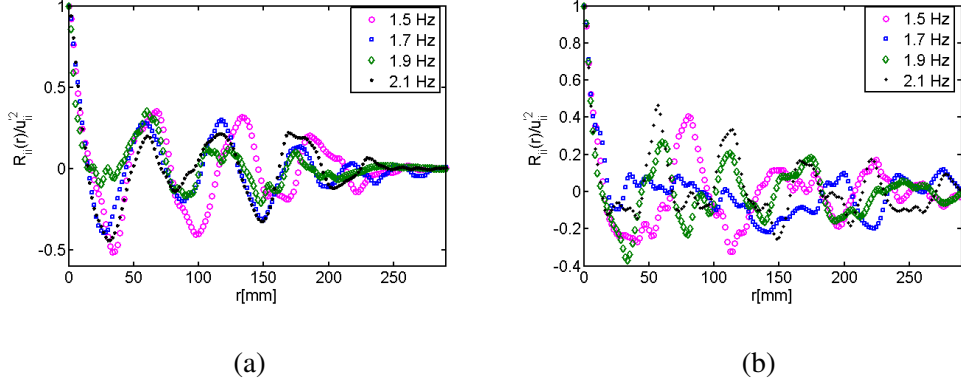


Figure 4.8: Longitudinal correlation of velocity fluctuations for the 4 frequencies.(a) $R_{uu}(x)$ (b) $R_{vv}(y)$

turbulence could not be applied for this case (i.e turbulence near the bottom was not homogeneous nor isotropic).

Therefore, the longitudinal and transverse integral scales could not be calculated from the velocity correlation function and a theoretical estimation was required. A theoretical way of estimating turbulent length scale is to evaluate it as 1/6 of the geometric scale [36]. The largest scale of the flow (geometric scale) is the width of the grid's chamber: 0.3m, therefore a good approximation for the integral scale is $l \sim 0.05m$.

In addition to integral scale, there are more scales that should be presented when discussing turbulent flow. The smallest scales (i.e Kolmogorov length scale) are defined using the average turbulent energy dissipation , $\varepsilon[m^2/s^3]$, defined as $\varepsilon = 2\nu s_{ij} s_{ij}$, where $s_{ij} = \frac{1}{2}(\frac{\partial u'_i}{\partial x_j} + \frac{\partial u'_j}{\partial x_i})$. u'_i is the i component of the fluctuating velocity [46]. Kolmogorov scales: the Kolmogorov length, velocity and time scales are defined on dimensional ground as:

$$\eta = (\nu^3 / \varepsilon)^{1/4} \quad (4.11)$$

$$\tau_\eta = (\nu / \varepsilon)^{1/2} \quad (4.12)$$

Taylor micro-scale λ , is defined from the relation of the fluctuating velocity and dissipation as shown in Eq.4.13. Taylor micro-scale is not the smallest relevant scale in turbulent flow, and it is different from the Kolmogorov scale. Though, λ is not a physically representative length scale it is used as a convenient length scale in evaluating the

Frequency [Hz]	$\varepsilon \cdot 10^{-4} [m^2/s^3]$	$\eta \cdot 10^{-4} [m]$	$\tau_\eta [s]$	$\lambda [m]$	Re_λ
1.5	0.92	3.2	0.1	0.016	650
1.7	1.4	2.9	0.08	0.018	1000
1.9	1.75	2.8	0.075	0.019	1230
2.1	1.96	2.7	0.07	0.02	1350

Table 4.4: Kolmogorov and Taylor length and time scales.

Taylor Reynolds number (Re_λ) associated with the field of velocity derivatives as shown in Eq.4.14.

$$\lambda = \sqrt{\frac{15v\bar{u}_{rms}^2}{\varepsilon}} \quad (4.13)$$

$$Re_\lambda = \frac{\lambda \bar{u}_{rms}}{v} \quad (4.14)$$

Table 4.4 presents the dissipation, Kolmogorov and Taylor scales calculated for 4 frequencies of the grid; \bar{u}_{rms} was calculated as the arithmetic average of the horizontal and vertical r.m.s of fluctuating velocity. The results provide a comparative view of the flow field and turbulence under the oscillating grid. Re_λ is in the range of 650-1350 which indicates on a high level of turbulence and fluctuations.

Fig.4.9 shows the pick-up ratio as a function of Re_λ . A linear correlation is shown between the pick-up ratio and Re_λ as opposed to the half parabolic correlation between the pick-up ratio and the frequency of the grid (Fig.4.2). Since Re_λ indicates on the amount of turbulence and fluctuations in the flow, it can be assumed that increase in turbulence under the oscillating grid affects the number of lift-offs more strongly than simply increasing the frequency of the grid.

4.4 Lagrangian results (3D-PTV)

The major results of particle tracking velocimetry experiments are Lagrangian trajectories defined as locations of particles in time and space. Fig.4.10 presents an isometric sketch of the Lagrangian trajectory demonstrating the incipient motion of a particle as it moves upwards and the trajectory of the tracer particles surrounding it, obtained for frequency of 1.7 Hz. Coordinates are given in millimeters in respect to the origin predefined by the calibration target, y is the vertical direction. Fig.4.10 demonstrates a quantitative analysis of the position, velocity and acceleration of the resuspended particle in x,y and z directions

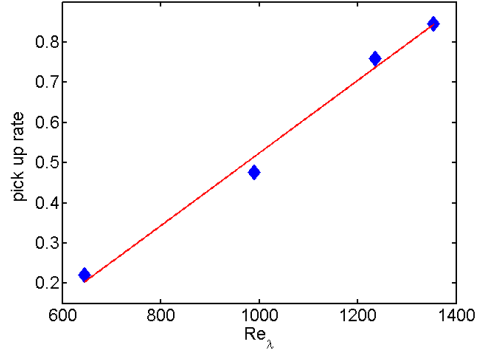


Figure 4.9: Taylor Reynolds number , Re_λ , versus the pick-up ratio.

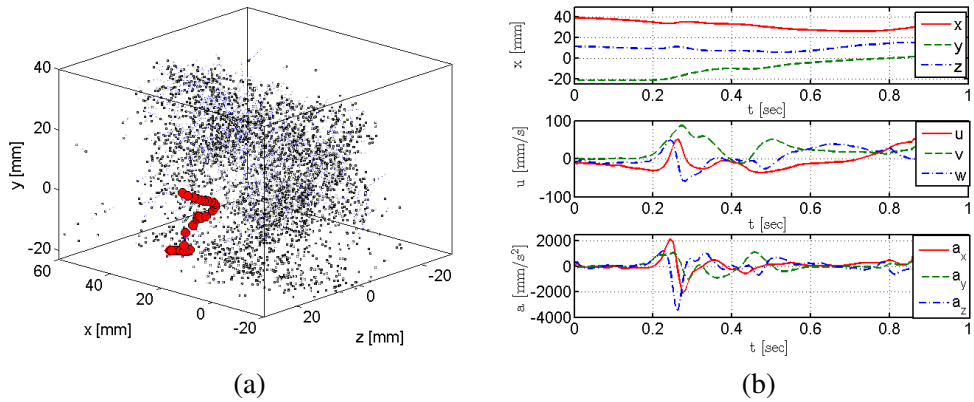


Figure 4.10: (a) Isometric sketch of a Lagrangian trajectory of a resuspended particle. (b) Position [mm], velocity [mm/s] and acceleration [mm/s²] of a resuspended particle during the incipient motion and lift-off phases.

in time. Both figures illustrates the particle complex movement: at the beginning of the motion for about 0.2 sec, the particle moves only in x and z direction, which means that it is either sliding or rolling on the bottom and only then lifted off and entrained into suspension. After pick up the velocity and acceleration , although not high, change in all directions consistently, result in a 3D motion.

4.4.1 Comparison with PIV results

Comparison between the probability distribution function (PDF) of the instantaneous velocity components measured by 3D-PTV and by PIV for frequency of 1.5Hz is presented in Fig.?.?. The PDFs of PIV and 3D-PTV instantaneous velocities were calculated at the same location, i.e: middle of the chamber (x axis Fig.3.2) between 1.5 to 2cm from the

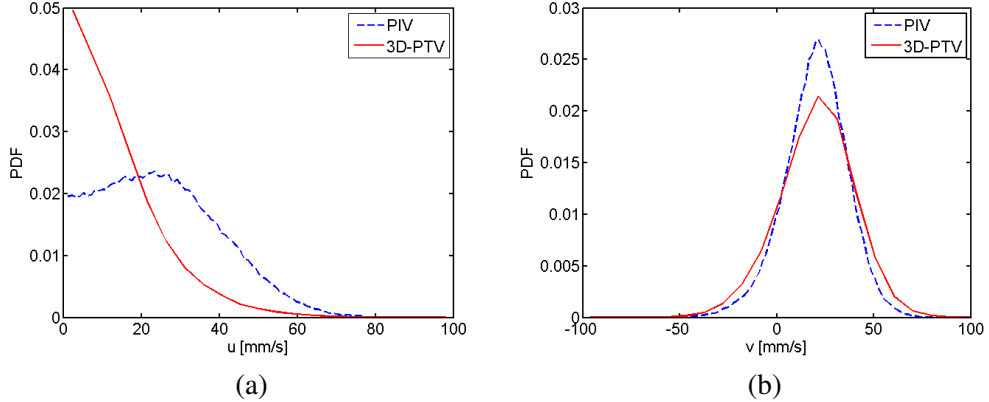


Figure 4.11: Comparison between PDFs of instantaneous velocity components measured by PIV and 3D-PTV for frequency of 1.5Hz. (a) Horizontal velocity component. (b) Vertical velocity component.

bottom (y axis). In order to avoid deviation due to different location of the zero point (on x axis) between the two measurement techniques, PDFs of the horizontal velocities absolute values, are presented. It can be seen that the velocity values measured from the PIV are of the same order of magnitude as the values measured from the 3D-PTV and they range between the same values: 0 - 70mm/s for the horizontal velocity and -70 - 100mm/s for the vertical velocity. Deviation can be seen between the PDFs of the horizontal instantaneous velocity; the PDF of the 3D-PTV is thinner and has higher values closer to zero. This may be explained by the fact that zero values of the velocity could be obtained using a PIV measurements only by decline from positive to negative values (and vice versa), while in 3D-PTV it is also possible when a particle remains in its place. Therefore, it is possible to obtain more zero values of the velocity in 3D-PTV. Moreover, the flow under the grid is inhomogeneous and characterized with substantial amount of fluctuations, hence the smallest difference between the area of calculations could cause deviation in the PDF of the velocities. Since the 3D-PTV measurements also has a third dimension, PDFs of 3D-PTV and PIV were not calculated at the exact same area. Therefore, the level of deviation between the velocity values from the two measurements techniques is acceptable and can be considered reasonable. Same results were observed for all frequencies of the grid, indicating that the measured data from both techniques can reliably describe the flow properties in these particular frequencies.

PIV measurements were performed 1.5-2cm above the bottom wall. Therefore, in order to perform a quantitative analysis that combines mean velocities or turbulent characteristics obtained from PIV with Lagrangian velocities obtained from 3D-PTV near the

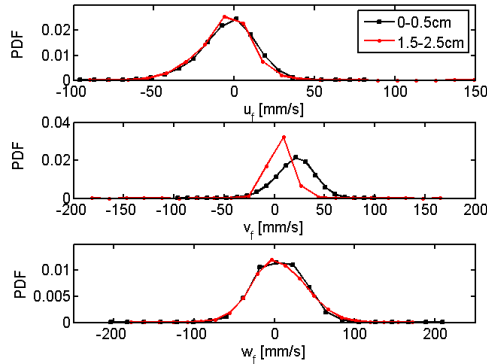


Figure 4.12: Comparison between PDFs of instantaneous velocity components measured by 3D-PTV at two different heights from the bottom of the chamber, for frequency of 1.5 Hz.

bottom (0-0.5cm from bottom), flow velocities at those distances should be of the same order of magnitude. Fig.4.12 presents PDFs of instantaneous velocity components measured by 3D-PTV at two different heights from the bottom; 0-0.5cm and 1.5-2.5cm (area of PIV measurements) from bottom, for frequency of 1.5Hz. As shown, the range of velocities PDF increases as the distance from the bottom increases. Hence, flow velocities near the bottom and 1.5cm away are different and only spatial,qualitative comparison between PIV and 3D-PTV results can be made.

4.4.2 Defining the lift-off events

As was previously described (section 4.2), particles motion during resuspension was divided into two main events; the first is the initial movement (detachment - beginning of particle movement on the bottom surface from a stationary position) and the second is the moment of lift off. The moment of lift off and the influence of flow characteristics on its occurrence, was determined as the focus of this study. Lift-off event was defined as the displacement of a single particle from the bottom of the grid chamber, moving upwards in the positive y direction. Determination of the exact time point at which the lift-off event occurs varies depending on either the change in position, velocity or acceleration. As shown in Fig.4.13, first the acceleration in y direction changes and its value increases, after 0.02s (3 time steps) the velocity changes and after 0.03s more (5 time steps) the position changes.

Although the time differences are smaller than the Kolmogorov time scale (0.07-0.1s), determination by either one of the properties might affect analysis and results. Time point

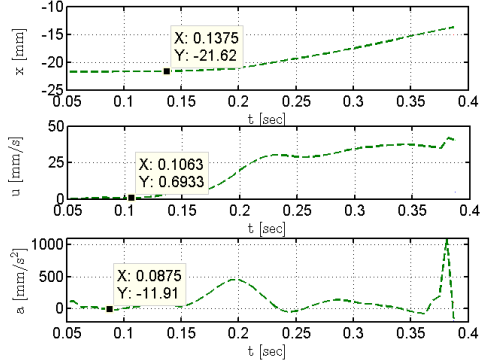


Figure 4.13: Position,velocity and acceleration (on y axis) of a re-suspended particle during lift-off.

for lift-off was defined as the first time step in which the position of the particle in y direction (in mm) changes in the first digit after the decimal point (i.e change in 0.1mm). In order to examine the possible impact of precise determination on the calculation of flow characteristics at the moment of lift-off, PDFs of velocity and acceleration components of tracers at distance of up to 25mm from the particle before and during lift-off were drawn (Fig.4.14). Velocity PDF are compatible. However, a deviation is observed between moment of lift-off and 0.3s,0.6s before in the z axis acceleration PDFs. A high peak at zero is shown in the PDF before lift-off , but is not shown in the PDF of lift-off. In addition in y and z axis, PDF before lift-off obtain higher positive values than during lift-off. Therefore, to reduce possible errors in further analysis, properties/parameters which involve acceleration of the tracers or velocity/acceleration of the test particles were calculated few time steps before and during lift-off. Time range of analysis was determined from the first time the resuspended particle enters the observation volume till the moment of event. In order for the event to be considered as a lift-off event , the particle must remain in suspension for at least 10 frames (1/16 sec). If a particle returned to the bottom of the grid chamber and remained at rest for at least 10 frames (1/16 sec) before moving again, a separate lift-off event was identified.

3D-PTV measurements were preformed in the center of the PIV measurements. Therefore a plain of overlap between the two methods enabled to link directly the location of individual particle lift-off with mean and turbulent flow characteristics. A distribution of the lift-off events locations on the x-z plane was preformed, by using the Lagrangian trajectories of the particles (3D-PTV results) as shown in Fig.4.15. For all frequencies, most of the lift-offs occurred on the x axis between -0.05 to 0.05, some occurred between 0.07 to 0.15 and none of the lift-offs occurred between 0.05 to 0.07. Coordination between

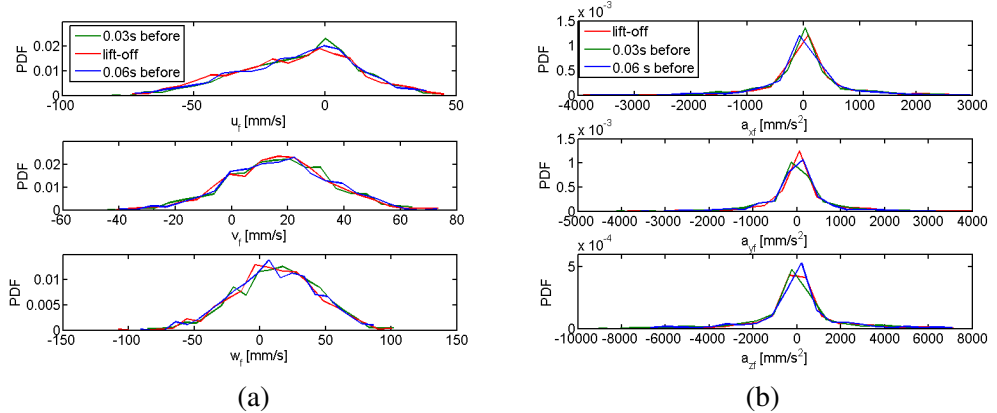


Figure 4.14: PDFs of flow tracers at distance of up to 25 mm from the particle, at three different time steps: During lift-off, 0.03s and 0.06s before lift-off. (a) Velocity components. (b) Acceleration components.

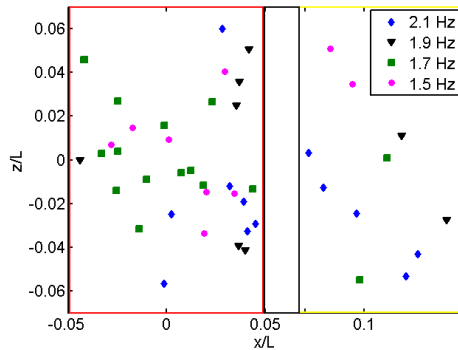


Figure 4.15: Spatial distribution of the location of lift-off events on x-z plane for 4 frequencies of the grid. Axis are normalized by the length of the grid chamber.

the areas of lift-offs and mean and turbulent flow characteristics was preformed (sections 4.3.1 and 4.3.2).

4.4.3 Correlations

Lagrangian velocity correlations between the particle and the tracers were calculated in order to estimated the length scales at the moment of lift-off and to determine the tracer-particle distance at which local flow properties will be calculated in the Lagrangian analysis. Eq.(4.16) presents a schematics view of the velocity correlation analysis, Where u_p and u_f are the particle and flow tracer velocities at the moment of lift-off, respectively. r

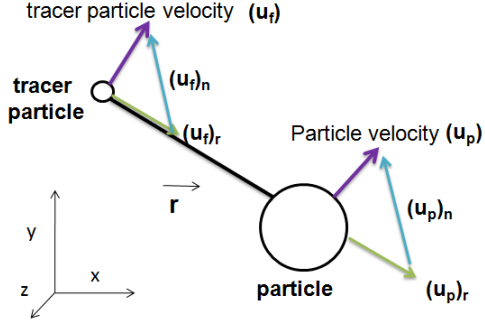


Figure 4.16: Lagrangian particle-fluid velocity correlations description: small circle denotes one of the flow tracers and the large circle represents a test particle.

is the distance vector between particle and tracer, $(u_p)_r$ and $(u_f)_r$ are the particle and flow tracer velocity vector projections on r , respectively. $(u_p)_n$ is the velocity vector perpendicular to $(u_p)_r$ and u_p , $(u_f)_n$ is the velocity vector perpendicular to $(u_f)_r$ and u_f .

Correlation coefficients were obtained according to Eq. 4.15.

$$R_{pf}(r) = \frac{u_p(x) \cdot u_f(x+r)}{\sqrt{u_p^2 \cdot u_f^2}} \quad (4.15)$$

Where $u_p(x)$ is the particle velocity at location x and $u_f(x+r)$ is the tracer velocity at distance r from the particle. The correlation coefficient of velocity vectors projection on r was marked as R_{rr} and the correlation coefficient between the perpendicular velocity vectors was marked as R_{nn} . Distance values between particle and tracers were divided into bins, in each bin an average of the correlation coefficient was estimated. Fig.(4.17) presents the average correlation coefficient as a function of the distance between the particle and tracers for frequency of $1.5Hz$. Since the flow was inhomogeneous, the average could have been affected by different selection of bin division. Therefore, the average of the correlation coefficient were calculated and presented for different bin division. At distances of 0-25mm, both correlation functions decreases and approach zero at distance of 20-25mm. At distances of 25-65mm, correlations values fluctuate: R_{rr} between 0-0.2 and R_{nn} between 0 -0.1, above distance of 65mm, correlations value increase. The number of tracers was low for distances smaller than 10mm and larger than 70mm, causing an insufficient statistics at those distances. Therefore, correlation coefficients at those distances were disregarded. Correlation functions of all frequencies showed similar trends. Thus, correlation between test particles and tracers exist both near (less than 25mm) and

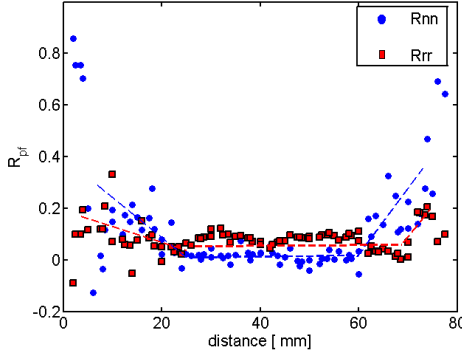


Figure 4.17: Particle-fluid velocity correlation functions at the moment of lift-off as a function of the distance [mm] particle-tracer, for $f = 1.5\text{Hz}$

away from the particles. It can be assumed that ,at the moment of lift-off, test particles are affected by the flow at small and large scales. In order to calculate flow properties close enough to the particle at the moment of lift-off, a compromise between the number of tracer and the distance from the particle had to be taken. It was decided that for further Lagrangian analysis, local flow properties will be calculated at a distances of up to 25mm from the particles, where 30% of the tracers quantity is achieved.

4.4.4 Vertical velocity

Since the same test particles were used in all the experiments, local flow conditions should be similar for all the events regardless of the frequency at which the experiment was done, in order to be determined as the sufficient conditions that cause lift-off occurrence. Whereas, the increase or decrease in frequency, should change the probability for a lift-off event to occur.

It was proposed that in order to suspend particle from bed, the vertical fluctuations, v_{rms} , must exceed a critical value of the submerged weight of the particles. Therefore, an estimation of vertical velocity fluctuations v' was preformed by calculating the local instantaneous vertical velocity fluctuations according to Eq.4.16.

$$v_t = v - \langle v \rangle \quad (4.16)$$

where $\langle v \rangle$ is the local average of velocity component, v is the instantaneous velocity component and v_t is the local fluctuating velocity component. Local average of instantaneous velocity fluctuations $\langle v_t \rangle$ over the local area (i.e radius up to 25 mm from the

particle) tend to zero, i.e. its magnitude is of the order of 10^{-18} and $\bar{v} \approx \langle v \rangle$. Therefore, v_t provides a reasonable estimate of velocity fluctuations u' . Local R.M.S of vertical velocity $\sqrt{\langle v_t^2 \rangle}$ was calculated as an estimation for v_{rms} . Fig. 4.18 present the local R.M.S of vertical velocity calculated within the radius of 25 mm from the test particles at every time step along their trajectories, normalized to the settling velocity of the test particles. Trajectories were shifted along the time axis, so the moment of lift off (marked in red) will be located at zero. The blue line describe the average of all the trajectories at the same frequency. For most particles (at all frequencies) the ratio of local R.M.S vertical velocity to settling velocity of the particle, i.e. $\frac{\sqrt{\langle v_t^2 \rangle}}{W_s}$, at the moment of lift-off, range between 0.1-1.6, few events occurred when the ratio was lower: 0.02-0.05. Most particles were lift-off a long period of time after the local R.M.S vertical velocity value obtained during lift-off was reached. Furthermore, no constant and repetitive change in the local R.M.S vertical velocity value (for all trajectories) was observed before the moment of lift-off. Therefore, instantaneous value of fluctuating vertical velocity could be considered ,on its own, only as a necessary but not as a sufficient condition for the occurrence of lift-off.

4.4.5 Turbulent kinetic energy

Turbulent kinetic energy (TKE) of the turbulence flow was proposed as a basis for comparing mass transfer under different flow conditions. The TKE can be defined from the r.m.s velocity fluctuation. The average of local fluctuating kinetic energy (LFKE) was calculated according to Eq.4.17 as an estimation for the turbulent kinetic energy of the flow near the particle. u_t, v_t, w_t are the instantaneous fluctuating velocity components of flow tracers, R is the radius from the particle position.

$$LFKE = \langle 0.5 \cdot (u_t^2 + v_t^2 + w_t^2) \rangle_R \quad (4.17)$$

Fig. 4.19 presents the average local fluctuating kinetic energy (LFKE) in radius up to 25 mm from the particle at every time step along particles trajectories for 4 different frequencies of the grid. Trajectories were shifted along the time axis, so the moment of lift off (marked in red) will be located at zero. As shown, in all four frequencies, lift-off events occurred when the range of the LFKE is between $0.3 \div 1.5 \times 10^{-3} m^2 s^{-2}$. The threshold value of LFKE required to lift-off the particles was defined empirically as the lowest value obtained at the moment of lift-off, e.g: about $4 \times 10^{-4}, 3 \times 10^{-4}, 5 \times 10^{-4}, 5 \times 10^{-4} m^2 s^{-2}$ for frequencies of 1.5, 1.7, 1.9 and 2.1 Hz, respectively. The differences in both LFKE and threshold values between the frequencies are insignificant and reflect the relatively low number of identified lift-off events. However, most particles were lift-off a long period

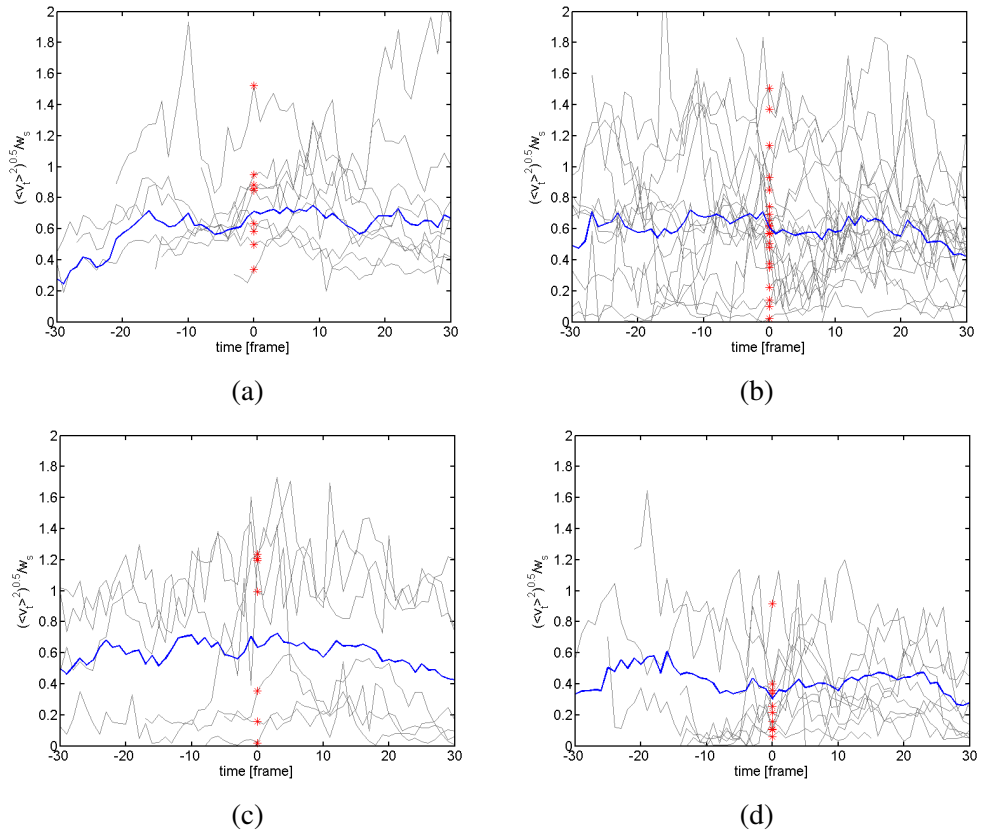


Figure 4.18: Local R.M.S vertical velocity around the resuspended particles, along their trajectories, for all frequencies. Velocity values are normalized by settling velocity of test particles. Trajectories are shifted along the time axis, so the moment of lift off (marked in red) will be located at zero. The blue line describe the average of all the trajectories at the same frequency. (a) 1.5 Hz (b) 1.7 Hz (c) 1.9 Hz (d) 2.1 Hz.

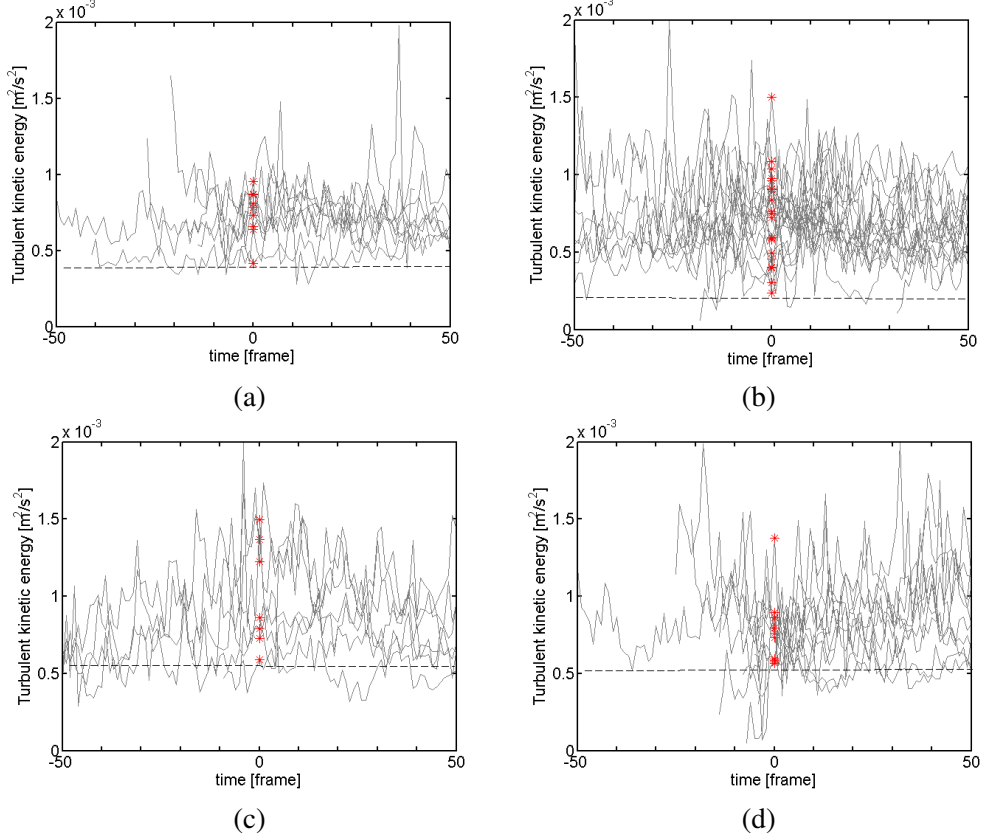


Figure 4.19: Local average fluctuating kinetic energy measured along the trajectory of the resuspended particles. Trajectories are shifted in respect to the lift-off event (marked by the red stars). (a) 1.5 Hz (b) 1.7 Hz (c) 1.9 Hz (d) 2.1 Hz.

of time after the threshold value was reached. Furthermore, no constant and repetitive change in LFKE value (for all trajectories) was observed before the moment of lift-off. Therefore, LFKE could be considered only as a necessary but not as a sufficient condition in order to compare lift-off events.

Using the lowest empirical threshold value of LFKE (i.e $0.0003 \frac{m^2}{s^2}$), the modified Shields parameter for the experimental conditions was estimated according to Eq.4.18 (Orlins and Gulliver [34]) as:

$$\theta^* = \frac{LFKE}{g(s-1)d_p} = 0.87 \quad (4.18)$$

As aforesaid the critical Shields parameter for the test particles in water ($Re_p \approx 10$) is $\theta_{cr} \approx 0.052$, more than one order of magnitude smaller than the modified Shields param-

eter. One possible explanation for the significant difference is the use of instantaneous fluctuating velocities for the kinetic energy calculation instead of the r.m.s. velocities ($TKE = 0.5 (u_{rms}^2 + v_{rms}^2 + w_{rms}^2)$), due to limitation of the 3D-PTV technique. Furthermore, due to lack of tracers in the very proximity of the particle at the lift-off moment, the calculation uses the information of the flow tracers within the distance of 25 mm. As was shown in Fig.4.12, tracers velocities increase as the distance from the bottom increases (i.e: distance from the particle at the moment of lift-off), therefore it is possible that the calculated values of LFKE and the modified Shields parameter are higher than the actual ones. In addition, the modified Shield parameter was determined (Bellinsky et al. [3]) for the moment of detachment (incipient movement of the particles on the bottom surface: rolling or sliding). It is possible that the kinetic energy of the flow required for lift-off is higher than required for detachment, hence the modified Shields parameter for lift-off is higher as compared to the values reported by Bellinsky et al. [3].

4.4.6 Forces

The forces acting on the particles during resuspension and lift-off were calculated according to Sridhar and Katz[?] method, the stokesian drag was replaced with a general drag and lift terms (because non-stokesian drag is known phenomenon in turbulent flows). The equation of the balance of forces was written as:

$$0 = F_g + F_p + F_i + F_b + F_d + F_l \quad (4.19)$$

Where the terms in the right side are, in order, buoyancy, pressure, inertia, Basset, drag and lift. The procedure involved measurement of the pressure, inertia, Basset and buoyancy forces on each particle and balancing their resultant (F_t) with lift and drag forces. Drag is parallel to the relative velocity between the particle and the fluid and the lift is perpendicular to it.

$$F_t = F_d + F_l = -(F_g + F_p + F_i + F_b) \quad (4.20)$$

Tracers velocity changes significantly as a function of their distance from the bottom (in y axis). In order minimize this effect, local fluid velocity and acceleration were calculated from the trajectories of tracer particles in radius up to 25mm and less than 10mm distance in y axis direction from the test particle. As an outcome, in each time step, local fluid properties were calculated according to 20-100 tracer particles. Relative Reynolds number ($Re_r = \frac{d_p U_{rel}}{\nu}$) was calculated based on the relative velocity U_{rel} between

the particle and local fluid at the moment of lift off and was found to range between 2-50. Buoyancy was computed from the average particle size and density according to Eq.A.14. Buoyancy acts on the test particle in parallel to gravitation direction ,opposite to the positive y axis direction and equals to $-5.7 * 10^{-8} N$.

$$F_g = \frac{4}{3}(\rho_p - \rho_l)g\pi r_p^3 \quad (4.21)$$

The pressure and inertia were calculated from the Lagrangian acceleration of the test particle and the local fluid surrounding it according to Eq.A.16 and A.18 respectively.

$$F_p = \frac{4}{3}\rho_l\pi r_p^3 \left\langle \frac{DU_f}{Dt} \right\rangle \quad (4.22)$$

$$F_i = -\frac{4}{3}\pi r_p^3 \left(\rho_p \frac{du_p}{dt} + m_a \rho_l \left\langle \frac{Du_p}{dt} - \frac{Du_f}{Dt} \right\rangle \right) \quad (4.23)$$

$\frac{DU_f}{Dt}$ is the average acceleration of local tracer particles, $\left\langle \frac{Du_p}{dt} - \frac{Du_f}{Dt} \right\rangle$ is the average difference between particle and local tracers accelerations. The first term in the inertia force is the body force of the particle ,which depends on the mass and acceleration of the particle. The second term is the apparent mass force. Based on Meng and Van der Geld [29], m_a (added mass coefficient) is 0.5 . Basset force was estimated according to Eq.A.20.

$$F_b = 6\pi r_p^2 \mu \int_0^t \frac{d\langle u_p - u_f \rangle / d\tau}{\sqrt{\pi v(t-\tau)}} \quad (4.24)$$

Where $\langle u_p - u_f \rangle$ is the average relative velocity between the particle and the local tracers. The average relative velocity was differentiated in time to obtain the relative acceleration. At each time step, Basset force was calculated based on the previous 6 time steps, i.e. $t = 6$ in the integral above. After calculating this forces, the force requires to balance them (F_t), was decomposed into two components to obtain the drag and the lift according to Eq.4.25 and 4.26.

$$F_d = \frac{F_t \cdot U_{rel}}{|U_{rel}|} \quad (4.25)$$

$$F_l = F_t - F_d \quad (4.26)$$

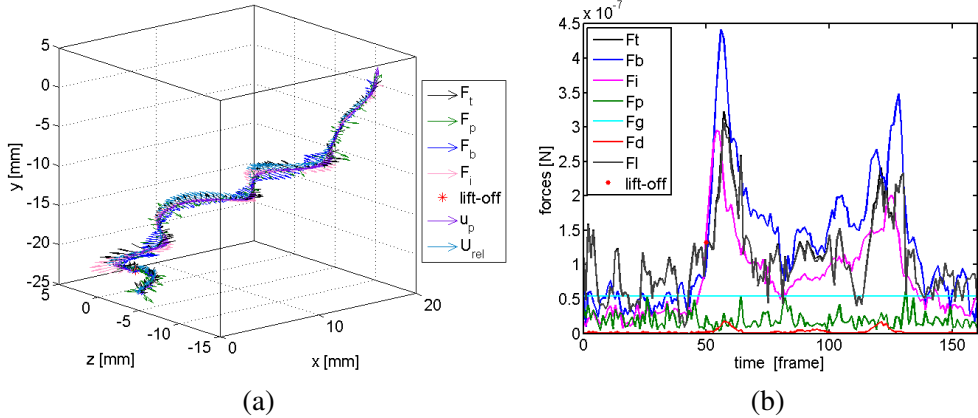


Figure 4.20: (a) presents an isometric sketch of a Lagrangian trajectory of a particle demonstrating the magnitude and direction of the forces acting on the particle at each time step, obtained for frequency of 1.7 Hz. (b) Magnitude of the forces acting on the particle in time, moment of lift-off is marked in red.

Fig. 4.20(a) presents an isometric sketch of a Lagrangian trajectory of a particle obtained for frequency of 1.7Hz, demonstrating the relative magnitude and direction of the forces acting on the particle, particle velocity (u_p) and the relative velocity (U_{rev}) between the particle and local fluid at each time step: before, during and after lift-off. Coordinates are given in millimeters in respect to the origin predefined by the calibration target, y is the vertical direction. Fig. 4.20(b) presents the magnitude of the forces acting on the particle in time, moment of lift-off is marked in red. As shown, magnitude of all forces (except for the drag) before lift-off is similar, close to the magnitude of buoyancy force and range between $0.2 \times 10^{-7} N$ to $1.5 \times 10^{-7} N$. Magnitude of lift, inertia and Basset forces increase from 4-10 time steps before lift-off until 10 time steps after lift-off, than they decrease, but remain higher then before lift-off. Magnitude of Basset force is approximately half of lift before lift-off and the highest of all forces after lift-off. Therefor, effect of Basset force is found to be important and could not be neglected. Magnitude of the drag is the lowest, approximately two orders of magnitude lower than lift. Namely most of F_t is perpendicular to the relative velocity (U_{rev}) between the particle and local fluid and the magnitudes of F_t and lift are similar. Error propagation of the forces (Appendix A.3.1) shows reasonable accuracy for buoyancy, pressure and basset forces. The accuracy of the inertia force ($\varepsilon_{F_i} = 1.2 \cdot 10^{-7} N$) is fairly low since its value is determined by subtracting accelerations, consequently the accuracy of drag and lift is also low since it is the sum of all forces errors.

Since the vector of U_{rev} changes its direction constantly, it was difficult to assess the impact of the forces on the lift-off event by dividing them to parallel and perpendicular

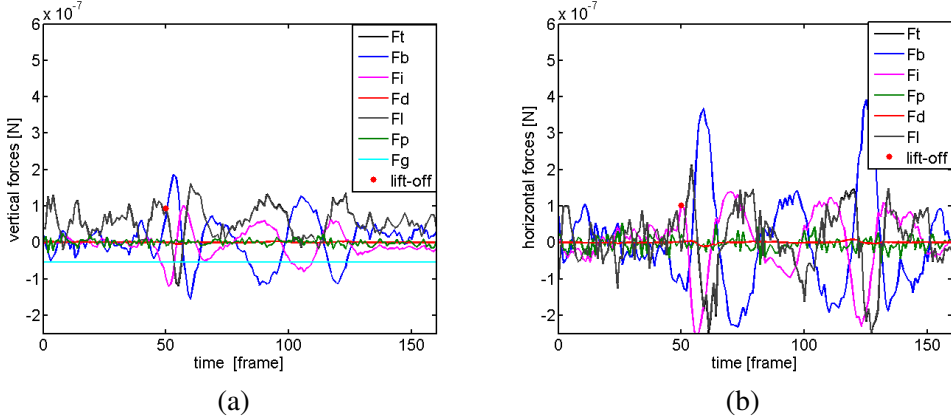


Figure 4.21: Forces acting on the particle in time, obtained for frequency of 1.7 Hz, moment of lift-off is marked in red. (a) Vertical forces (b) Horizontal forces.

components in respect to U_{rev} . Therefore, all forces were divided to vertical (y axis), which act in parallel to buoyancy, and horizontal (x and z axis) components as shown in Fig.4.21. In the horizontal direction, magnitude of all forces (except for the drag) before lift-off are similar, while in the vertical direction, magnitude of Basset and lift before lift-off are higher than pressure and inertia.

The inertia force equation includes two terms: the first is the (-) body force of the particle ($-m_p a_p$), while the second is the apparent mass force. Fig. 4.22 presents the vertical component of the first term in the inertia force, for frequencies of 1.7 Hz and 1.9Hz. At each frequency, the trajectories were shifted along the time axis, so the moment of lift off (marked in red) will be located at zero. The blue lines describe the average of all the trajectories at the same frequency of the grid.

The vertical component of the body force is nearly zero from the beginning of the moment till eight time steps before lift-off, then it decreases significantly. As was previously mentioned (Fig. 4.13), moment of lift-off was determined according to changes in the position of the particle, although the acceleration of the particle started to increase eight time steps earlier. Therefore, the acceleration of the particle in the vertical direction is zero till eight time steps before lift-off, when it starts to increase. However, few trajectories in Fig.4.22 show a minor deviation from zero before lift-off. This could be due to the error in the value of particle acceleration. Another possible explanation is that during the identification process in 3D-PTV, some particles, which were rolling on the bottom before lift-off, were identified once at their upper part and once at their bottom, causing a “fake”, low vertical acceleration. The same trends were observed for all frequencies.

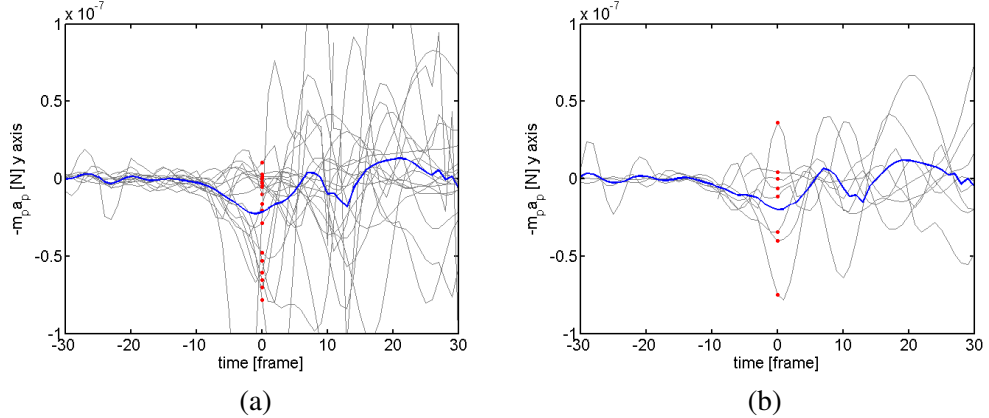


Figure 4.22: Vertical (y axis) component of the first term in the inertia force. Trajectories are shifted along the time axis, so the moment of lift off (marked in red) will be located at zero. The blue line describe the average of all the trajectories at the same frequency of the grid. (a) 1.7 Hz (b) 1.9 Hz.

Fig. 4.23 present the vertical components of (-) body force, apparent mass force, pressure force and Basset force, for frequencies of 1.7Hz and 1.9Hz. Each line presents the average quantity of all trajectories at the same frequency. Eight time steps before lift off, vertical component of body force ($-m_p a_p$) decrease below zero, indicating on an increase in particles vertical acceleration. This is also the first time, vertical component of the body force and vertical components of apparent mass and pressure forces are separated from one another. The difference between them increases until lift-off, then the vertical acceleration decreases and difference between forces decrease as well. Six to eight time steps after lift-off, vertical forces re-combined. Since the pressure force depends fully on fluid accelerations and the apparent mass force depends both on the fluid and the response of the particle, this is understandable; Initially the particle moves quite rapidly compared to the flow, moving away from the surface. As the particle moves into the faster flow away from the bottom of the chamber, the velocity difference between particle and flow decreases. Ten to eight time steps before lift off, respectively to the increase in vertical acceleration of the particle, the value of the vertical Basset increases significantly till ten time steps after lift-off, when it decreases and then increases again. The same trend was observed for all frequencies.

In order to assess and determine the causes for lift-off, a change in the forces exerted by the fluid on the particle (i.e: pressure, apparent mass or Basset force) should be observed before the increase in vertical acceleration of the particle. The change should be similar and constant for all frequencies. Pressure force acts on the particle by the non-uniform ambient fluid and depends fully on fluid acceleration. Its vertical value fluctuates

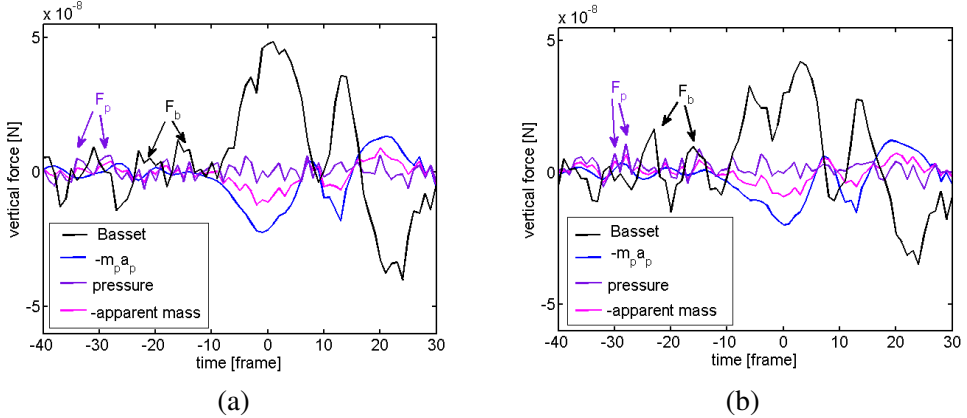


Figure 4.23: Vertical components of first term ($-m_p a_p$), second term (apparent mass force) of inertia force, pressure and Basset force. Each line presents the average quantity of all trajectories at the same frequency. (a) 1.7 Hz (b) 1.9 Hz.

constantly, probably since it was calculated by averaging together all tracers accelerations in distance of 25 mm from the particle. Two consecutive, high picks in the vertical value are observed around 30 time steps before lift-off (approximately 20 time step, i.e.: 1/8s, before the change in the acceleration) at all frequencies. Apparent mass force, which depends on both the fluid uniforms and the response of the particle, show similar trend, before the change in the acceleration of the particle. In addition, Two consecutive, high picks in the vertical value of Basset force are observed around 25 and 15 time steps before lift-off at all frequencies. Both changes, in pressure and Basset could be a possible trigger for the lift-off event.

Fig.4.24 presents the vertical (y axis direction) and horizontal component of F_t force respectively for frequencies of 1.5 and 2.1 Hz. Both components of F_t include the drag and lift, acting on the particle along its trajectory, however most of F_t is perpendicular to the relative velocity (U_{rev}) between the particle and local fluid, namely the magnitudes of F_t and lift are similar, therefore F_t can represent the lift. The blue line describes the average force of all the trajectories at the same frequency of the grid. At all frequencies, the range of both horizontal and vertical components of F_t increases gradually from eight time steps before lift-off till eight-ten time steps after lift-off when it decreases. Increase and decrease are compatible to particle vertical acceleration. The particle will start to move upwards when lift exerted by the fluid on the particle is enough to pull it away from the surface. When the particle moves away from the bottom, the velocity difference between particle and flow decreases and lift should be decreases. However, no significant changes in both horizontal and vertical components of F_t are shown previous to the change

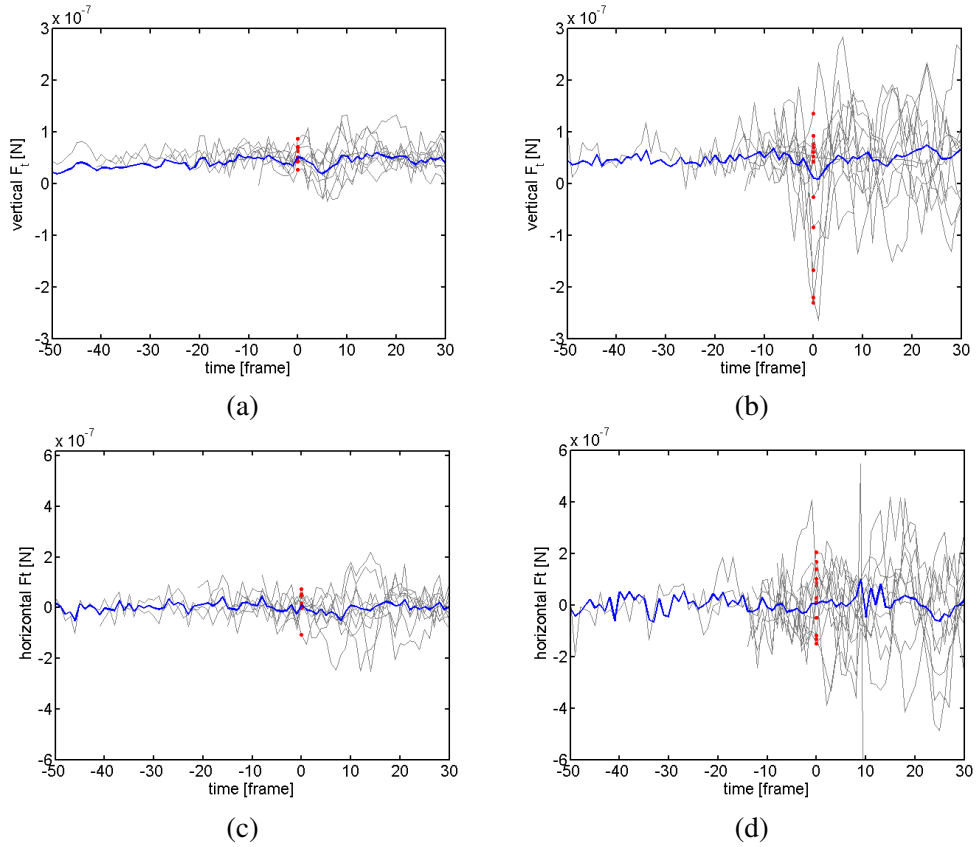


Figure 4.24: Vertical and horizontal components of F_t force (the sum of lift and drag forces) acting on the particle along its trajectory. Trajectories were shifted along the time axis, so the moment of lift off will be located at zero. Moment of lift-off is marked in red and the blue line describes the average force of all the trajectories at the same frequency of the grid. (a) Vertical, 1.5Hz (b) Vertical, 2.1Hz (c) Horizontal, 1.5Hz (d) Horizontal, 2.1Hz.

in particle vertical acceleration.

5 Summary and discussion

The scope of the present study is to explore the necessary conditions for lift-off of spherical particles, that are free to move on a smooth bed, into a turbulent flow in an oscillating grid chamber. Simultaneous measurements of local flow conditions and 3D Lagrangian trajectories of test particles before and during lift-off were preformed using 3D-PTV technique for 4 different frequencies of the grid. In addition, detailed turbulent flow field measurements near the bed were obtained using PIV technique.

Turbulence generated under the grid is not isotropic nor homogeneous, for instance the ratio of horizontal to vertical turbulent intensities was as high as 1.4. Although some sort of the mean flow due to secondary motion was observed, fluctuations were always dominant compared to the temporally averaged components indicating on a high level of turbulence. The spatial decay of turbulence with the distance from the grid was irregular and did not follow Eq.4.8. The time averaged pick up ratio was strongly correlated with the turbulent Reynolds number, Re_λ as opposed to the weaker relation to the frequency of the grid (Fig.4.2). This result indicate that a small increase in the amplitude of turbulent fluctuations can significantly increase the probability of lift-off events. These macroscopic measurements have revealed also that there are preferential locations under the grid at which most of the lift-off events occur. In order to learn in details the necessary conditions for the lift-off events, a large set of 3D-PTV measurements was performed, as explained in Section 4.4.

Direct determination of the location and moment of lift-off of solid particles, along with simultaneous 3D Lagrangian trajectories of flow tracers near the test particles, enabled to investigate in-situ the mechanisms that lead to the lift-off event. 3D-PTV recordings of the resuspension events were performed in the center of the PIV plane and thus probability distribution function (PDF) of the instantaneous velocity components measured by 3D-PTV and by PIV show good agreement (Fig.4.11). Therefore spatial, qualitative coordination between the location of the lift-off events obtained from the trajectories of test particles and the statistical properties of turbulence from the flow field was made

(Fig. 4.13). Turbulent statistics could for the first time be linked directly to the moment of lift off and to the local flow properties. Lift-off events occur concomitantly to high Reynolds stress, horizontal velocity fluctuations (u_{rms}) and absolute value of horizontal mean velocity (Fig 4.5 and Fig. 4.6). These findings reinforce the significance of these specific turbulent-particle interaction on mobilizing the particles.

The average of local fluctuating kinetic energy (LFKE) was calculated as an estimation for the turbulent kinetic energy (TKE) of the flow near the particle. Modified Shields parameter, Θ^* , calculated for the experimental conditions according to Eq.4.18 [34] deviated from the critical Shields parameter by more than one order of magnitude. One possible explanation for the significant difference is the use of instantaneous fluctuating velocities for the kinetic energy calculation instead of the r.m.s. velocities. Empirical u_{rms} and v_{rms} (Table 4.3), based on statistical turbulent flow field, obtained from PIV measurements, are also one order of magnitude higher than the expected values according to Eq. 4.8, indicating that the estimation of TKE by LFKE is a good approximation. Another possible explanation is that Bellinsky et al. [3] have neglected the effect of the bottom wall, which makes the turbulence anisotropic, and assumed approximate isotropy of turbulence induced by the oscillating grid. Furthermore, their calculation of the modified Shield parameter was based on equation 4.8 and not on direct turbulent flow measurements. Similar to our results, Wan Mohatar and Munro [50] modified Shields parameter calculated for anisotropy turbulence in the near bed region, differ by two orders of magnitude from the values predicted by Shields diagram. This evidence points out that the any attempt to model the resuspension of the particles has to take into account the level of anisotropy in the streambed boundary layer.

Since, the same test particles were used in all the experiments, local flow conditions should be similar for all the events regardless of the frequency at which the experiment was done, in order to be determined as the sufficient conditions that cause lift-off occurrence. Whereas, the increase or decrease in frequency, should change the probability for a lift-off event to occur. No constant and repetitive change in LFKE value (for all trajectories) was observed before the moment of lift-off. Furthermore, most particles were lift-off a long period of time after the threshold value, defined empirically as the lowest value obtained at the moment of lift-off, was reached (Fig.4.19). Therefore, LFKE can be considered only as a necessary but not as a sufficient condition in order to compare lift-off events.

The most important innovative side of this thesis is that by applying Sridhar and Katz[?] method, we could estimate the forces acting on the freely moving test particles before and during lift-off. The pressure, inertia and Basset forces were calculated from the

Lagrangian acceleration of the test particle and the local fluid surrounding it. Magnitude of all forces (except for the drag) before lift-off was similar and close to the magnitude of buoyancy force. Basset force was calculated based on the previous six time steps, its magnitude is approximately half of lift before lift-off and the highest of all forces after lift-off. We can conclude that this typically neglected term, can not be neglected in the problem of resuspension of freely sliding or rolling particles. Since $Re_w = \frac{W_s d_p}{\nu} < 4000$ and $s = \frac{\rho_p}{\rho_f} \sim 1$, this finding is in very good agreement with recent investigations that took numerical approach [20, 4, 33]. Magnitude of the drag is the lowest among the force terms, approximately two orders of magnitude lower than lift term, indicating that the turbulent lift is the dominant force in this study. The magnitude of the total force, measured from particle acceleration, F_t and lift are similar, therefore F_t can represent the lift in this problem and be estimated directly from simpler experiments. However, no significant changes in both horizontal and vertical components of F_t were shown previous to the change in particle vertical acceleration (Fig. 4.24). Two consecutive high peaks in the vertical average values of pressure and Basset forces were observed before the change in the vertical acceleration of test particles at all frequencies (Fig.4.23). Both peaks, to the best of our understanding, point out a possible trigger for lift-off events. Since the Basset force is the only force calculated as a integral over time, this observation raise the assumption that the duration of the period of force is also important, similarly to the proposal of Celik et al. [8]. Previous studies have already mention the importance of the pressure gradient in mobilizing particles, e.g. [40, 53]. However, a significant change before lift-off should have also appeared in lift force, which was not obvious from our measurements. It is important to notice that in order to calculate flow properties close enough to the test particle, we had to compromise between the number of tracers and the radius of the local flow region around the particle. Local flow properties were calculated at a distances of up to 25 mm from the particles, where 30% of the tracers quantity was achieved (Fig4.17). This trade-off could lead to over- or under-estimate of the force terms. On the one hand it is possible that as a result, some force peaks could have been disappeared in the overall data due to averaging of distant particles. On the other hand, it is also possible that the observed pressure force was due to distant particles and the high peaks do not necessarily correlate directly to the lift-off events. In order to get a better proof of the proposed mechanisms, a much higher resolution of the instantaneous 3D flow fields and additional pressure gradient measurements below and above the test particles before and during the moment of lift-off, is required. Such experiment, however, seems to not to be feasible in the visible future as it will require super-resolution 3D-PTV along with the pressure-sensitive painting or miniature pressure catheters embedded in the flow at the place and time of particle resuspension.

It is nevertheless important to understand that despite the limitation of relatively large region required to collect statistics of inertia, lift and drag forces, this study is probably the only experimental study that measured entrainment of the particles as they freely move on a smooth bed, directly, three-dimensionally and simultaneously with the flow field and forces on particles during the lift-off events.

6 Conclusion

- Direct determination of the location and moment of lift-off of solid particles, along with simultaneous 3D Lagrangian trajectories of flow tracers near the particles, enabled to investigate in-situ the mechanisms that lead to the lift-off event.
- Lift-off events, under the OGT, occur concomitantly to high Reynolds stress, horizontal velocity fluctuations (u_{rms}) and absolute value of horizontal mean velocity. These findings reinforce the significance of these specific turbulent-particle interaction on mobilizing the particles.
- Any attempt to model the resuspension of particles has to take into account the level of anisotropy in the streambed boundary layer.
- Estimation of TKE (turbulent kinetic energy) by LFKE (local fluctuating kinetic energy) is a good approximation. LFKE can be considered only as a necessary but not as a sufficient condition in order to compare lift-off events.
- Basset force term can not be neglected in the problem of resuspension of freely sliding or rolling particles.
- Two consecutive high peaks in the vertical average values of pressure and Basset forces were observed before the lift-off of the test particles, at all frequencies. Both peaks might point out a possible trigger for lift-off events. More measurements are required in order to get a better proof of the proposed mechanisms.

6.1 Research limitation and recommendations for future work

Simultaneous direct 3D measurement of the entrainment of freely moving test particles with local flow at a sufficient frame rate, in order to investigate in-situ the mechanisms

that lead to the lift-off event, poses complex experimental challenges. First, the amount of tracers at the vicinity of the particle should be sufficient at every time step. However, the amount of tracers change at each time step. Furthermore tracers ,near the particle, could be shaded by the particle resulting in shorts trajectories and reduction in the accuracy of measurements. On the other hand, measurements at larger regions could lead to over- or under-estimate of the force terms. Comparison between measured forces and flow properties at different regions from the particle could shed light on the problem. Second, measurement of particle movement from the moment of detachment til moment of lift-off is difficult since particles are in and out of the observation volume leading to relatively low number of lift-off event detected. Therefore multiple number of measurements is required.

The possible importance of Basset force raise the assumption that it is not only the magnitude of the applied force that is important for resuspension, but also the duration of the force. Therefore, it is recommended to test this assumption in future work by observing the joint distribution of magnitude and duration of forces on lift-off .

References

- [1] J.F. Atkinson, L. Damiani, and D.R.F Harleman. Physics and modelling of turbulent particle deposition and entrainment: Review of a systematic study. *Physics of fluid*, 35:827–839, 1987.
- [2] R.A. Bagnolds. The nature of saltation and "Bed-load" transport in water. *Prof. Royal Soc. London*, A332, 1973.
- [3] M. Bellinsky, H. Rubin, .Y Agnon, E. Kit, and J Atkinson. Characteristics of resuspension, settling and diffusion of particulate matter in a water column. *Enviromental fluid mechanics S*, 5(5):415–441, 2005.
- [4] F. A. Bombardelli, A. E. González, and Y. I. Niño. Computation of the particle Basset force with a fractional-derivative approach. *J. Hydraul. Eng*, 134(10), 2008.
- [5] M Bourgoin and X Haitao. Focus on dynamic of particles in turbulence. *New journal of physics*, 16, 2014.
- [6] J.M. Buffington. The legend of A.F. Shields - Closure. *Journal of Hydraulic Engineering*, 126:721–723, 2000.
- [7] E. Calzavarini, R. Volk, E. Leveque, J.F. Pinton, and F. Toschi. Impact of trailing wake drag on the statistical properties and dynamic of finite-sized particle in turbulence . *Physics: Nonlinear phenomena. Special issue on small scale turbulence*, 241, 2012.
- [8] A.O. Celik, P. Diplas, C. L. Dancey, and M. Valyrakis. Impulse and particle dislodgement under turbulent flow conditions. *Phys. Fluids*, 22(4), 2010.

- [9] S. Corrsin and J. Lumely. On the equation of motion for a particle in turbulent fluid . *Applied Scientific Research*, 6, 1956.
- [10] T. H. Dracos. *Three-Dimensional Velocity and Vorticity Measuring and Image Analysis Technique: Lecture Notes from the short course held in Zurich, Switzerland*. Kluwer Academic Publisher, 1996.
- [11] A. Dwivedi, W.B. Melville, A.Y. Shamseldin, and T.K Guha. Analysis of hydrodynamic lift on a bed sediment transport. *Journal of geophysical research*, 116, 2011.
- [12] F. Engelud. A criterion for the occurrence of suspended load. *Notules hydruliques, La houille Blanche*, 6, 1965.
- [13] H. J. S. Fernando and I. P. D. De Silva. Oscillating grids as a source of nearly isotropic turbulence . 6(7):2455–2464, 1994.
- [14] H.J.S. Fernando and I.P.D. De Silva. Note on secondary flows in oscillating-grid, mixing-box experiments. *Phys. Fluids* , 5:1849–1851, 1993.
- [15] M.H. Garcia. The legend of A.F. Shields. *J. Hydraul. Eng.*, 126(9):718–720, 2000.
- [16] L.A. Gimenez-Curto and M.A. Corniero. Entrainment threshold of cohesionless sediment grains under steady flow of air and water. *Sedimentology*, 56, 2009.
- [17] K.G. Heayse, H. Friedrich, and B. W. Melville. Advanced particle tracking for sediment movement on river beds: A laboratory study. In *17th Australasian Fluid Mechanics Conference*, 2010.
- [18] E. J. Hopfinger and J. A. Toly. Spatially decaying turbulence and its relation to mixing across density interfaces. *Journal of Fluid Mechanics*, 78:155–175, 1976.
- [19] Dabiri D. Huang H. and Gharib M. On errors of digital particle image velocimetry. *Measurement Science and Technology*, 8:1427–1440, 1997.
- [20] N. Lukerchenko. Basset history force for the bed load sediment transport. In *IAHR European Division Congress*, volume 5 p (CD-Rom), 2010.
- [21] B. Lüthi, A. Tsinober, and W. Kinzelbach. Lagrangian measurement of vorticity dynamics in turbulent flow. *Journal of Fluid Mechanics*, 528:87–118, 2005.

- [22] D.A. Lyn. Observation of initial sediment motion in a turbulent flow generated in a square tank by a vertically oscillating grid . In *ASCE water Research Engineering Conference, San Antonio*, pages 608–612, 1995.
- [23] H.G. Maas, A. Gruen, and D.A. Papantoniou. Particle tracking velocimetry in three-dimensional flows. *Experiments in fluids*, 15:133–146, 1993.
- [24] N.A. Malik, T.H. Dracos, and D.A. Papantoniou. Particle tracking velocimetry in three dimensional flows, part 2: Particle tracking. *Experiment in Fluids*, 15:279–294, 1993.
- [25] M. R. Maxey and J. J. Riley. Equation of motion for a small rigid sphere in a nonuniform flow. *Physics of Fluids*, 26:883–889, 1983.
- [26] S.R. McLean. Turbulent structure over two dimentional bed forms:Implication for sediment transport . *Journal of Geophysical Research: Oceans*, 99(C6), 1994.
- [27] P. Medina, M.A. Sanchez, and J.M. Redondo. Grid stirred turbulence: Applications to the initiation of sediment motion and lift-off studies. *Physics and chemistry of earth part b-hydrology ocean and atmosphere*, 26(4):299–304, 2001.
- [28] A. Melling. Tracer particles and seeding for particle image velocimetry. *Measurement Science and Technology*, 8(12):1406–1416, 1997.
- [29] H. Meng and C.W.M Van der Geld. Particle trajectory computations in steady non-uniform liquid flows. *ASME Fluids Engineering Division*, 118:183–193, 1991.
- [30] M.A. Nearing and S.C. Parker. Detchment of soil by flowing water under turbulent and laminar conditions. *Soil Science of America Journal*, 58, 1994.
- [31] J.M. Nelson, R.C. Sherve, S.R. Mclean, and T.G. Drake. Role of near bed turbulence structure in bed load transport and bed form mechanics. *Water Resources Research*, 31(8), 1995.
- [32] Y Nino, F Lopez, and M Garcia. Threshold for particle entrainment into suspension. *Sedimentology* , 50(2):247–263, 2003.
- [33] S. Olivieri, F. Picano, G. Sardina, D. Ludicone, and L. Brandt. The effect of the Bas-set history force on particle clustering in Homogeneous and Isotropic Turbulence. *Physics of Fluids* , 26(4), 2014.

- [34] J.J. Orlins and J.S. Gulliver. Turbulence quantification and sediment resuspension in an oscillating grid chamber. *Exp. Fluids*, 34(6):662–677, 2003.
- [35] A.S. Paintal. Concept of critical shear stress in loose boundary open channel . *Journal of hydraulic research*, 9 , Issue 1, 1971.
- [36] S.B. Pope. *Turbulent Flows*. Cambridge University Press, 2000.
- [37] M. Raffel, C. Willert, and J. Kompenhans. *Particle Image Velocimetry*. Springer-Verlag Berlin Heidelberg, 1998.
- [38] J.M. Redondo, X.D. de Madron, P. Medina, M.A. Sanchez, and E. Schaaff. Comparison of sediment resuspension measurements in sheared and zero-mean turbulent flows. *Continental shelf research*, 21:2095–2103, 2001.
- [39] M.M. Sarma, H. Chamoun, D.S.H. Sita Rama Sarma, and R.S. Schechter. Factors controlling the hydrodynamic detachment of particles from surfaces. *Colloid Interface Science*, 149, 1992.
- [40] M.W. Schmeeckle, J.M. Nelson, and R.L. Shreve. Forces on stationary particles in near bed turbulent flows. *Journal of geophysical research*, 112, 2007.
- [41] A. Shields. Application of similarity principles and turbulence research to bed-load movement. Technical report, U.S Dept of Agr., Soil Conservation Service cooperative Laboratory, California Institute of Technology, 1936.
- [42] G. Sridhar and J. Katz. Drag and lift forces on microscopic bubbles entrained by a vortex. *Physics of Fluids*, 7:389–399, 1995.
- [43] E.J. Stadhuis. Basics and principles of particle image velocimetry for mapping biogenic and biologically rlevant flows. *Aquatic Ecology*, 40(4):463–479, 2006.
- [44] B.M. Sumer, L.H.C . Chua, N.S. Cheng, and J. Fredsoe. Influence of turbulence on bed load sediment transport. *Journal of hydraulic engineering*, 129:585–596, 2003.
- [45] Z.J. Taylor, R. Gurka, and A. Liberzon. Particle image velocimetry for biological mechanics. 2014.

- [46] H. Tennekes and J. L. Lumley. *A first course in turbulence*. MIT Press Boston, 1972.
- [47] F Toschi and E Bodenschatz. Lagrangian properties of particles in turbulence. *Annual Review of Fluid Mechanics*, 41:379–404, 2009.
- [48] L.C. Van Rijn. Sediment transport, Part1: Bed load transport . *Journal of hydraulic engineering*, 110 , No. 10, 1984.
- [49] V.A. Vanoni. *Sedimentation engineering: American society of civil engineers, Manuals and reports on engineering practice*, volume 54. ASCE-AMER civil engineers, 1975.
- [50] W.H.M. Wan Mohatar and R.J. Munro. Threshold criteria for incipient sediment motion on an inclined bedform in the presence of oscillating-grid turbulence. *Physics of Fluids*, 25:015103, 2013.
- [51] J Westerweel. Fundamental of digital particle image velocimetry. *Measurement Science and Technology*, 8(12):1379–1392, 1997.
- [52] J Westerweel. Theoretical analysis of the measurement precision in particle image velocimetry. *Experiments in fluids*, 29(7), 2000.
- [53] U.C.E Zanke. On the begining of suspension from bed. *Advances in hydro-science and engineering*, VI, 2003.
- [54] G. Ziskind. Particle resuspension from surfaces: Revisited and re-evaluated. *Reviews in Chemical Engineering*, 22(1-2):1–123, 2006.

A Measurement uncertainty

The aim of uncertainty analysis is to quantify the effect of measurement errors in order to estimate the quality of the reported results. In many cases, the required property is not measured directly but calculated from an acceptable formula. Considering a property y which is a function of n independent variables $y = f(x_1, \dots, x_n)$, the propagation of error ε_y can be evaluated as:

$$\varepsilon_y = \left(\sum_i^n \left(\frac{\partial f}{\partial x_i} \varepsilon_{x_i} \right)^2 \right)^{0.5} \quad (\text{A.1})$$

When \bar{y} is the mean of a set of several repeated measurements, the propagation of error, ε_y , can be evaluated as:

$$\varepsilon_y = \frac{s_d}{\sqrt{N}} \quad (\text{A.2})$$

where s_d is the standard deviation and N is the number of measurements in the set.

A.1 Settling test and Visualization results

The main source of uncertainty in particles settling velocity is the error in the number of frames $\varepsilon_{N_f} = 1 \text{ frame}$; other errors such as: the error in frame rate $\varepsilon_{f_r} = 1/1000$ and the distance measuring error $\varepsilon_{L_{lines}} = 0.01 \text{ mm}$ are negligible and do not affect the total error of the settling velocity. Average settling velocity was calculated as 10.79 mm/s , with an error of $\varepsilon_{W_s} = 0.5 \text{ mm/s}$ and variation of $\sim 1 \text{ mm/s}$ (9%); Main reason for variation was due to the variance in particles diameter: 12%. Particle density was calculated from equation A.3, and evaluated as $\rho_p = 1062 \text{ kg/m}^3$.

$$W_s = \frac{2r_p^2(\rho_p - \rho_l)g}{9\mu} \quad (\text{A.3})$$

The resulting error is: $\varepsilon_{\rho_p} = 3kg/m^3$, the relative error is 0.3%.

Initial pick-up time and pick-up ratio $n(t)$ were determined for each frequency according to the average of four experiments. Error in initial pick-up time for each measurement was 1sec, the variance for every frequency is within the range of 10%. In order to evaluate the pick-up ratio, particles were counted manually. Therefore, the error of pick-up ratio could not be calculated accurately. However, the accuracy of the results at each frequency was evaluated according to their variance - up to 15%.

A.2 PIV

The independent variables from which the velocity is calculated are the particle displacement and the time interval between laser pulses. The time interval between laser pulses is one of the system timing parameters defined by the user. The error $\varepsilon_{\Delta T}$ can be evaluated as the synchronizer response time which is $0.02\mu s$ according to the manufacturer data sheet. Particle displacement is the measured property in the PIV technique. Owing to its complexity, error quantification is a function of various factors. Some depend on the experimental conditions such as: light sheet thickness and intensity, density of tracer particles, diameter of tracer particles, poor image quality, non-uniform illuminations (variation in image intensity), reflection of surfaces and magnification ratio. Other factors arrive from the particle displacement algorithm used. The error in particle displacement evaluation has been studied extensively over the years [52, 37, 19]. The main parameters mentioned in most cases are the IA size in pixels (N_{IA}), image density (N_I) and particle image diameter (d_τ) defined as the ratio between the particle diameter seen in the image and the pixel dimension. Evaluation of the three parameters in the present setup is detailed in the followings. The size of the square interrogation window is $N = 32pixels$, magnification ratio of 7.43, mean particle diameter of $10\mu m$ and particle image diameter is $d_\tau = 5pixels$. Image density is the number of particle images captured in the interrogation area and defined as:

$$N_I = \left(\frac{C_t \Delta Z_0}{M_0^2} \right) D_I^2 \quad (\text{A.4})$$

Where C_t is the number density of the tracing particles, ΔZ_0 is the light sheet width, M_0 is the magnification ratio and D_I is the interrogation window length. The width of the laser sheet is 0.5 mm. The length of a 32X32 pixels interrogation window is 3.56mm. The density number C_t equals to the number of particles divided by the flowing fluid volume. Considering 10gr of powder containing seeding particles with a mean diameter of $10\mu m$

and density of $1.05\text{g}/\text{ml}$ added to a 19 liter fluid, the number density can be calculated as:

$$C_t = \frac{m/(V_p \cdot \rho_p)}{V_{tank}} = \frac{10g/((4\pi(10 \cdot 10^{-3}\text{cm})^3/3) \cdot 1.05\text{g}/\text{cm}^3)}{1.9 \cdot 10^7\text{mm}^3} \approx 120\text{mm}^{-3} \quad (\text{A.5})$$

Substituting the mentioned values yields an image density of $N_I = 14$. According to [52], the measurement error for an experimental setup characterized by $N_I = 15$, $N = 32\text{pixels}$ and $d_\tau = 2\text{pixels}$ is reduced to 0.02pixels under ideal conditions such as uniform particle diameter and the absence of background noise. Since ideal conditions cannot be achieved completely in real experiment, a measurement error of $\varepsilon_{\Delta x} = 0.2\text{pixels} = 0.023\text{mm}$ was considered.

The maximal particle displacement in both directions was $\Delta x = 8\text{pixels} = 0.897\text{mm}$. Maximal time interval between laser pulses $\Delta t = 7\text{ms}$ was considered as the characteristic time interval with an error of $\varepsilon_{\Delta t} = 0.02\mu\text{s}$. Velocity error was calculated as:

$$\varepsilon_u = \sqrt{\left(\frac{\partial u}{\partial \Delta x} \cdot \varepsilon_{\Delta x}\right)^2 + \left(\frac{\partial u}{\partial \Delta t} \cdot \varepsilon_{\Delta t}\right)^2} = \left(\left(\frac{\varepsilon_{\Delta x}}{\Delta t}\right)^2 + \left(-\frac{\Delta x}{\Delta t^2} \cdot \varepsilon_{\Delta t}\right)^2\right)^{0.5} = 3.3\text{mm/s} \quad (\text{A.6})$$

Measured absolute velocity values are in the range of $30 \div 150\text{ mm/s}$, therefore the relative error is $2\% \div 11\%$.

A.3 3D-PTV

The independent variables which determine the method uncertainty are the particle 3D coordinates determined in each time step and the time interval between the frames. Error quantification of particle position is a function of accuracy of both the peak search (pre-processing), which finds the position of each particle image, and the calibration, which allows to determine particle 3D coordinate.

Under ideal condition, the accuracy in the peak search is evaluated as 0.05pixel , however under experimental conditions in flow measurements application with imperfect spherical particles and illumination non-uniformities, accuracy of the order 0.2pixel is a more realistic assumption [10].

Errors in calibration arise from several sources, such as: residual lens aberrations, imprecision in calibration target production and imperfect placement of the calibration

target. Particle coordinates error in a stationary state can be determined in the stationary calibration process if the number of target points is larger than the number required for the solution of the photogrammetric model. The software treats the remaining points as unknowns and estimates their computed coordinates. The differences between the known points and the computed ones can then be calculated. Taking into account the conversion of pixels to millimeters, which is $16\text{pixel}/\text{mm}$ in the current measurements, the software provides the estimation of the error as $\varepsilon_x = \varepsilon_y = \pm 10\mu\text{m}$ for x and y direction. If all four cameras are arranged on the same side of the observation volume, the error in z direction (perpendicular to the model, volume depth) is usually 2-3 times higher than the length and width directions (x and y directions), therefore $\varepsilon_z = \pm 30\mu\text{m}$. However, the error in z direction can be improved by arranging the cameras from both sides of the observation volume as was preformed in the current measurements. Furthermore, a dynamic calibration improves the accuracy of the parameters determined in the stationary calibration in all directions. Therefore, the real error of particle position is smaller and the error estimation can be considered conservative.

From particle trajectories the flow velocity can be derived directly as: $u = \frac{x(t+\Delta t) - x(t)}{\Delta t}$. However, this process is very sensitive to particle position errors, therefore the whole position signal of each trajectory is low-pass filtered and filtered velocity and acceleration signals are derived as first and second derivatives from the filtered trajectory. Considering that the velocity and acceleration of the particles changes at time steps equivalent to Kolmogorov time scale of the measurements ($\tau_\eta = 0.07 - 0.1\text{s}$), the time interval for filtered velocity and acceleration error calculations can be estimated as $\Delta t = \frac{\tau_\eta}{5} = \frac{0.07\text{s}}{5} = 0.014\text{s}$. The time delay is controlled by a synchronization unit with very high precision, therefore has little effect on the overall accuracy. Estimation of velocity error can be calculated as follows:

$$\varepsilon_u = \varepsilon_v = \sqrt{2 \cdot \left(\frac{1}{\Delta t} \cdot \varepsilon_x \right)^2} = 1.01\text{mm/s} \quad (\text{A.7})$$

$$\varepsilon_w = 3.03\text{mm/s} \quad (\text{A.8})$$

$$|\vec{u}| = \sqrt{u^2 + v^2 + w^2} \quad (\text{A.9})$$

u_f	v_f	w_f	$ u_f $	$\epsilon_{ u_f }$	u_p	v_p	w_p	$ u_p $	$\epsilon_{ u_p }$
0.05	0.065	0.07	0.11	0.0021	0.07	0.06	0.05	0.1	0.0017

Table A.1: Estimated particle and tracers velocity error [m/s].

a_{xf}	a_{yf}	a_{zf}	$ a_f $	$\epsilon_{ a_f }$	a_{xp}	a_{yp}	a_{zp}	$ a_p $	$\epsilon_{ a_p }$
2.5	2.7	6.0	7.0	0.266	1.2	1.0	1.5	2.1	0.224

Table A.2: Estimated particle and tracers acceleration error [m/s²].

$$\epsilon_{|\vec{u}|} = \sqrt{\left(\frac{\partial |\vec{u}|}{\partial u}\right)^2 + \left(\frac{\partial |\vec{u}|}{\partial v}\right)^2 + \left(\frac{\partial |\vec{u}|}{\partial w}\right)^2} = \sqrt{\frac{[(u \cdot \epsilon_u)^2 + (v \cdot \epsilon_v)^2 + (w \cdot \epsilon_w)^2]}{u^2 + v^2 + w^2}} \quad (\text{A.10})$$

Estimation of acceleration error can be calculated as follows:

$$\epsilon_{ax} = \epsilon_{ay} = \sqrt{2 \cdot \left(\frac{1}{\Delta t} \cdot \epsilon_u\right)^2} = 102 \text{mm/s}^2 \quad (\text{A.11})$$

$$\epsilon_{az} = 306 \text{mm/s}^2 \quad (\text{A.12})$$

$$\epsilon_{|\vec{a}|} = \sqrt{\left(\frac{\partial |\vec{a}|}{\partial a_x}\right)^2 + \left(\frac{\partial |\vec{a}|}{\partial a_y}\right)^2 + \left(\frac{\partial |\vec{a}|}{\partial a_z}\right)^2} = \sqrt{\frac{[(a_x \cdot \epsilon_{a_x})^2 + (a_y \cdot \epsilon_{a_y})^2 + (a_z \cdot \epsilon_{a_z})^2]}{a_x^2 + a_y^2 + a_z^2}} \quad (\text{A.13})$$

The velocity and acceleration of particles and tracers change constantly with time and position; particle velocity and acceleration increase after lift-off. Therefore, in order to maintain a conservative approach and to estimate the highest possible error, particle velocity and acceleration values were chosen as the average (the average value between all particles) value obtained after lift-off, tracers velocity and acceleration values were evaluated as the highest values in tracers velocity and acceleration histograms. Since there was no considerable difference between the four frequencies, the same values were chosen for all four.

Table A.1 and table A.2 present the estimated particle and tracers velocity and acceleration errors respectively.

A.3.1 Error propagation

A.3.1.1 Buoyancy force

The buoyancy force is defined as:

$$F_g = \frac{4}{3}(\rho_p - \rho_l)g\pi r_p^3 \quad (\text{A.14})$$

The error depends on ρ_p and r_p and can be evaluated as follows:

$$\epsilon_{F_g} = \sqrt{\left(\frac{\partial F_g}{\partial \rho_p} \cdot \epsilon_{\rho_p}\right)^2 + \left(\frac{\partial F_g}{\partial r_p} \cdot \epsilon_{r_p}\right)^2} = 2.6 \cdot 10^{-9} N \quad (\text{A.15})$$

Estimated buoyancy force is $-5.7 \cdot 10^{-8} N$, therefore the relative error is 4.5%.

A.3.1.2 Pressure force

The pressure force is defined as:

$$F_p = \frac{4}{3}\rho_l\pi r_p^3 <\frac{DU_f}{Dt}> \quad (\text{A.16})$$

where $<\frac{DU_f}{Dt}>$ is defined as the mean Lagrangian acceleration of tracers up to 25 mm from the particle. The error in the mean Lagrangian acceleration of tracers was estimated by the standard deviation of tracers acceleration and the number of tracers. The number of tracers was chosen as the lowest number of tracers observed at a specific time step in order to obtain the highest possible error; $\epsilon_{<a_f>} = 800 \frac{mm}{s^2}$, $<a_f> = 1200 \frac{mm}{s^2}$. Therefore, the estimated error of pressure force is:

$$\epsilon_{F_p} = \sqrt{\left(\frac{\partial F_p}{\partial r_p} \cdot \epsilon_{r_p}\right)^2 + \left(\frac{\partial F_p}{\partial a_f} \cdot \epsilon_{<a_f>}\right)^2} = 6.9 \cdot 10^{-8} N \quad (\text{A.17})$$

A.3.1.1 Inertia force

The inertia force is defined as:

$$F_i = -\frac{4}{3}\pi r_p^3 \left(\rho_p \frac{du_p}{dt} + m_a \rho_l <\frac{Du_p}{dt} - \frac{Du_f}{Dt}> \right) \quad (\text{A.18})$$

The estimated error is:

$$\varepsilon_{F_i} = \sqrt{\left(\frac{\partial F_i}{\partial r_p} \cdot \varepsilon_{r_p}\right)^2 + \left(\frac{\partial F_i}{\partial \rho_p} \cdot \varepsilon_{\rho_p}\right)^2 + \left(\frac{\partial F_i}{\partial \langle a_p - a_f \rangle} \cdot \varepsilon_{\langle a_p - a_f \rangle}\right)^2 + \left(\frac{\partial F_i}{\partial a_p} \cdot \varepsilon_{a_p}\right)^2} = 1.2 \cdot 10^{-7} N \quad (\text{A.19})$$

A.3.1.1 Basset force

The Basset force is defined as:

$$F_b = 6\pi r_p^2 \mu \int_0^t \frac{d \langle u_p - u_f \rangle / d\tau}{\sqrt{\pi v(t-\tau)}} d\tau \quad (\text{A.20})$$

The estimated error should be calculated as follow:

$$\varepsilon_{F_b} = \sqrt{(12\pi r_p \mu \int_0^t \frac{d \langle u_p - u_f \rangle / d\tau}{\sqrt{\pi v(t-\tau)}} d\tau \cdot \varepsilon_{r_p})^2 + \left(\frac{6\pi r_p^2 \mu}{\sqrt{\pi v(t-\tau)}} \cdot \frac{\Delta \langle u_p - u_f \rangle}{\Delta \tau} \cdot \varepsilon_{\frac{\Delta \langle u_p - u_f \rangle}{\Delta \tau}}\right)^2} \quad (\text{A.21})$$

The first term is of the order of $10^{-11} N$, at the second term, $\left(\frac{6\pi r_p^2 \mu}{\sqrt{\pi v(t-\tau)}} \cdot \frac{\Delta \langle u_p - u_f \rangle}{\Delta \tau}\right)$ is of the order of $10^{-5} N$. The value of $(\varepsilon_{\frac{\Delta \langle u_p - u_f \rangle}{\Delta \tau}})$ should be estimated by calculating the standard deviation of the term. However, since the Basset force was calculated based on the previous 6 time steps and not every tracer appeared at each time step in the trajectory of the particles, the resulting Basset force from the effect of each tracer could not be calculated (only the relative velocity between particle velocity and the average velocity of local tracers could be calculated). Still, it can be assumed that the value of $(\varepsilon_{\frac{\Delta \langle u_p - u_f \rangle}{\Delta \tau}})$ is smaller than $10^{-3} N$. Therefore, a conservative estimation for the Basset force error can be of the order of $\sim 10^{-8} N$.

B Velocity convergence plots

Velocity convergence plots were preformed for the PIV experiments. For each of the four frequencies of the grid, a cumulative average of instantaneous velocity components at 2cm from the bottom of the grid's chamber was preformed according to eq.B.1.

$$S_N = \frac{1}{N} \sum_1^N (\mathbf{u})_i \quad (\text{B.1})$$

where N is the number of instantaneous velocity maps. Fig. B.1 show the cumulative average as a function of the number of instantaneous velocity maps for each frequency. It can be seen that for every frequency the cumulative average converges after approximately 350 images. Therefore, we can support the accuracy of the results extracted from the velocity maps and there is no obligation to require images of the flow at the same phase of the grid oscillatory.

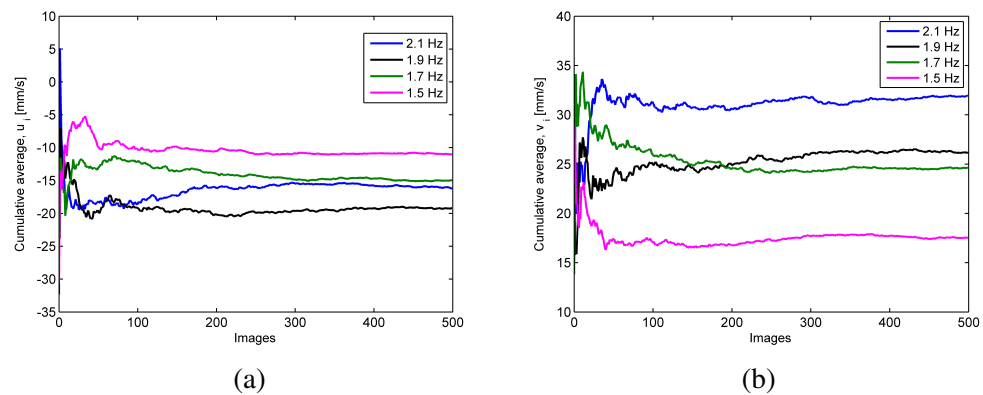


Figure B.1: Cumulative average of instantaneous velocity as a function of the number of instantaneous velocity maps for four frequencies of the grid [mm/s]
(a) Horizontal velocity. (b) Vertical velocity.

תקציר

הקריטריון לתנועה הראשונית של חלקי חומר החשופים לזרם והרחבתם הינו מגנון חשוב במגוון תחומים, כגון: שינוי פנאומטי, זיהוי חומי נפץ, ניקוי שבבי סיליקון בתעשייה, פיזור חלקי אבק, משקעים וחומרים מזהמים בסביבות טבעיות. מרכיבות התופעה הנובעת מהצורך באיפיון הקשר בין החלקיק לשטח ממנו הוא מתרומות ובין החלקיק לזרם אליו הוא השופ. בנוסף קיים הקושי הטכני במדידה בו זמןית של תכונות הזורם, הכוחות הפעלים על החלקיק ותונעטו ברגע ההרחה. עקב הקשיים הללו היבטים רבים בקשר בין החלקיק המתחיל תונעטו על ידי ולתוך הזרימה הטורבולנטית הינם ידועים כוון איקוטי בלבד.

מחקר זה מציג מדידות ב-3 מימדים של תנאי הזרימה ההכרחים להרחבת חלקיים כדוריים מיקרומטריים הנעים בחופשיות על משטח חלק, בזרימה טורבולנטית בעלת מאץ גזירה ממוצע אפס, תחת רשות התונדת. במסגרת המחקר בוצעו בו זמןית מדידות לוגנגיאניות ב-3 מימדים, באמצעות טכניקת מדידה V-PTV³, המאפשרת לעקב אחריו החלקיקים ואחריו הזורם בתונעתם החופשית. מהנתונים הייחודיים הללו הצלחנו להעריך את הכוחות הפעלים על החלקיקים לפני וברגע ההרחה כמו כן בוצעו מדידות שדה הזרימה בקרבת משטח ההרחה באמצעות טכניקת מדידה דו-מימדית עם רזולוציה מרחבית גבוהה - PIV.

באמצעות שילוב השיטות האופטיות, ניתן היה לקשר ישירות בין תכונות הזרימה הטורבולנטיות למיקום ההרחה. תוצאות המחקר מראות כי ההרחבות מתרחשות בהתאם לאזורים בהם מאconi רייןולדס, תנודות המהירות האופקיות, r_{rms} , והמהירות האופקית הממוצעת הינם גבוהים. בהשוואה למודלים קיימים עבור הרחבת חלקיים תחת רשות תונדת, מתרברר כי רוב ההרחבות התרחשו זמן רב לאחר שערך ה- LKE (שינוי האנרגיה הקינטית הטורבולנטית המקומית) עבר את ערך הסף. על כן, פרמטר זה עשוי להיות פרמטר הכרחי אך לא מספיק במקרה של הרחפה. כוחות האינרציה, הלחץ, הגרא, העילי וכח המctrבר על החלקיק (Basset) החובבו באמצעות התאצות הלוגנגיאניות של החלקיקים המורחפים והזורם המקומיים בסביבתם. תוצאות הניסוי מראות כי כוח העילי הטורבולנטי, הינו כוח הדומיננטי במחקר זה. כמו כן, לא ניתן להזניח את כוח Basset בעקבות הרחפה של חלקיים הנעים (על ידי גלגול או החלקה) על פני המצע. שני שיאים עוקבים בערבי כוח הלחץ ו- Basset האងיים נצפו לפני רגע ההרחה. שיאי הערך אלו אלו עשויים להציבו על מגנון אפשרי להרחה. יש צורך במחקר נוסף במקרה להוכיח חשיבות המגנון המוצע בזרימות טורבולנטיות נוספות, עם ולא הגזירה הממוצעת.

אוניברסיטת תל-אביב
הפקולטה להנדסה ע"ש איבי ואלדר פליישמן
בית הספר לתארים מתקדמים ע"ש זנדמן-סלינגר

הרחה של חלקיים תחת גריד תנך

חיבור זה הוגש כעבודה מחקר לקרהת התואר "מוסמך אוניברסיטה" בהנדסה מכנית
על ידי

הדר טרויגוט

העבודה נעשתה בבית הספר להנדסה מכנית
בנהichtet פרופסור אלכס ליברzon

שבט התשע"ה

אוניברסיטת תל-אביב

הפקולטה להנדסה ע"ש איבי ואלדר פליישמן

בית הספר לתארים מתקדמים ע"ש זנדמן-סלינגר

הרחפה של חלקיים תחת גריד תנך

חיבור זה הוגש כעבודת מחקר לקרהת התואר "מוסמך אוניברסיטה" בהנדסה מכנית
על ידי

הדר טרויגוט

שבט התשע"ה